

STUDY OF STRUCTURAL & OPTICAL PROPERTIES OF OXIDES IN SOFT X-RAY REGIME

By
Mangalika Sinha

Enrolment Number: PHYS03201404011

**Raja Ramanna Centre for Advanced Technology
Indore-452013, India**

**A thesis submitted to the
Board of Studies in Physical Sciences**

**In partial fulfillment of requirements for the Degree of
DOCTOR OF PHILOSOPHY
Of
HOMI BHABHA NATIONAL INSTITUTE**



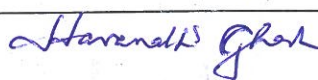

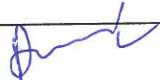

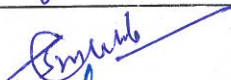



August 2020

Homi Bhabha National Institute¹

Recommendations of the Viva Voce Committee

As members of the Viva Voce Committee, we certify that we have read the dissertation prepared by **Mangalika Sinha** entitled “**Study of Structural & Optical Properties of Oxides in Soft X-Ray Regime**” and recommend that it may be accepted as fulfilling the thesis requirement for the award of Degree of Doctor of Philosophy.


Chairman - Prof. Arup Banerjee		Date: 13/08/2020
Guide / Convener - Prof. Mohammed H. Modi		Date: 13.8.2020
Co-guide- Prof. H. Ghosh		Date: 13.08.2020
Examiner - Prof. S. Mishra		Date: 13 th Aug, 2020
Member 1- Prof. A.K. Karnal		Date: 13-08-2020
Member 1- Prof. Tapas Ganguli		Date: 13-08-2020
Member 2- Prof. S.M. Gupta		Date: 13.08.2020
Member 4- Prof. D.M. Phase		Date: 13.08.2020

Final approval and acceptance of this thesis is contingent upon the candidate's submission of the final copies of the thesis to HBNI.

I/We hereby certify that I/we have read this thesis prepared under my/our direction and recommend that it may be accepted as fulfilling the thesis requirement.

Date:

Place: RRCAT, Indore

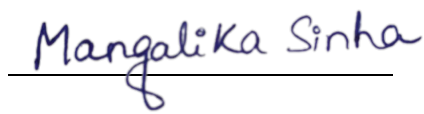
 13.8.2020
(Guide, Prof. M. H. Modi)

¹ This page is to be included only for final submission after successful completion of viva voce.

STATEMENT BY AUTHOR

This dissertation has been submitted in partial fulfillment of requirements for an advanced degree at Homi Bhabha National Institute (HBNI) and is deposited in the Library to be made available to borrowers under rules of the HBNI.

Brief quotations from this dissertation are allowable without special permission, provided that accurate acknowledgement of source is made. Requests for permission for extended quotation from or reproduction of this manuscript in whole or in part may be granted by the Competent Authority of HBNI when in his or her judgment the proposed use of the material is in the interests of scholarship. In all other instances, however, permission must be obtained from the author.


Mangalika Sinha

DECLARATION

I, hereby declare that the investigation presented in the thesis has been carried out by me. The work is original and has not been submitted earlier as a whole or in part for a degree/diploma at this or any other Institution/University.

Mangalika Sinha

Mangalika Sinha

List of publications arising from the thesis

In Journal:

1. Effect of zirconium oxide local structure on soft X-ray optical properties near the oxygen K-edge region.
Mangalika Sinha, R. K Gupta, Kiranjot, Amol Singh, Mohammed H. Modi
J. Appl. Phys. **128**, 065302(1-9) (2020).
2. Influence of the core-hole effect on optical properties of magnesium oxide (MgO) near the Mg L-edge region.
Mangalika Sinha, Mohammed H Modi, Haranath Ghosh, P. K Yadav, R. K Gupta
J. Synchrotron Rad. **25**, 771-776 (2018).
3. Soft X-ray characterization of ion beam sputtered magnesium oxide (MgO) thin film.
Mangalika Sinha, Mukul Gupta, Philippe Jonnard, Mohammed Hussain Modi
Surf. Interface Anal. **50**, 1145-1148 (2018).
4. Depth resolved compositional analysis of aluminium oxide thin film using non-destructive soft X-ray reflectivity technique.
Mangalika Sinha, Mohammed H. Modi
Appl. Surf. Sci. **419**, 311-318 (2017).
5. Optical constants of off-stoichiometric aluminum oxide thin film in 6-20 nm soft-X ray/extreme ultraviolet region.
Mangalika Sinha, Saurabh Sharma, Amol Singh, Mohammed H. Modi
Jpn. J. Appl. Phys **55**, 101101(1-5) (2016).
6. Optical constants of e beam-deposited zirconium dioxide measured in the 55-150 Å wavelength region using the reflectivity technique.
Amol Singh, Mangalika Sinha, R. K. Gupta, Mohammed H. Modi
Appl. Opt. **55**, 3170-3175 (2016).
7. Investigation on depth resolved compositions of e-beam deposited ZrO₂ thin film.
Amol Singh, Mangalika Sinha, R. K Gupta, Mohammed H. Modi
Appl. Surf. Sci. 419, 337-341 (2017).

In conference proceedings:

1. X-ray reflectivity and photoelectron spectroscopy study of aluminium oxide thin film.
Mangalika Sinha, Mohammed H. Modi
AIP Conf. Proc. **1832**, 080025 (1-3) (2017).
2. Glancing angle Soft X-ray reflectivity (SXR) and total electron yield (TEY) characterization of ZrO₂ thin film near O K-edge
Mangalika Sinha, Amol Singh, R.K. Gupta, Mohammed H. Modi
AIP Conf. Proc. **2054**, 040004(1-5) (2019).
3. Continuous optical constants (δ & β) spectra of aluminum oxide near Al L and O K-edge region
Mangalika Sinha, R. K. Gupta, P. Dasilva, P. Mercere, and Mohammed H. Modi
AIP Conf. Proc. **2115**, 030207 (1-4) (2019).

Other publications during the PhD work

1. Depth analysis of Al/ZrC interfaces using SIMS and X-ray reflectivity.
Mohammed H. Modi, Mangalika Sinha, Aniruddha Bose, Amol Singh, Philippe Jonnard
Surf. Interface Anal. **50**, 1239-1242 (2018).
2. Study of the Au-Cr bilayer system using X-ray reflectivity, GDOES, and ToF-SIMS.
Philippe Jonnard, Mohammed H. Modi, Karine Le Guen, Nargish Aneshwari, Mangalika Sinha, Mourad Idir, Patrick Chapon, Anouk Galtayries
Surf. Interface Anal. **50**, 1213-1217 (2018).
3. Study of soft X-ray optical properties of niobium carbide (NbC) thin film in 6–15 nm wavelength region.
Amol Singh, Mangalika Sinha, Mohammed H. Modi
Vacuum **155**, 60-63 (2018).
4. Kramers-Kronig analysis of soft X-ray reflectivity data of platinum thin film in 40-200 Å wavelength region.
Saurabh Sharma, R. K. Gupta, Mangalika Sinha, P. Yadav, Amol Singh, Mohammed H. Modi
AIP Conf. Proc. **1731**, 080001(1-3) (2016).

5. A soft X-ray reflectivity beamline for 100-1500 eV energy range at Indus-2 synchrotron radiation source

Mohammed H. Modi, R. K. Gupta, S. R. Kane, V. Prasad, C. K. Garg, P. Yadav, V. K. Raghuvanshi, Amol Singh, and Mangalika Sinha.

AIP Conf. Proc. **2054**, 060022(1-5) (2019).



Mangalika Sinha

**DEDICATED TO MY
GRANDMOTHER**

ACKNOWLEDGEMENTS

Firstly, I would like to thank my supervisor Dr. Mohammed H. Modi, on the successful completion of my thesis work. He has a great quality to simplify the experimental difficulties that eventually helped me in successful completion of experiments without much hesitation.

I sincerely thank Dr. Haranath Ghosh, for infusing many theoretical ideas that helped me a lot in growing up in the field of science.

I am extremely thankful to Dr. Tapas Ganguli, Head ISUD for his constant encouragement & fruitful discussions. I am grateful to Dr. Arup Banerjee, Dr. P. A Naik, Dr. Aparna Chakrabarti, Dr. S. M Gupta, Dr. D. M Phase and all other Doctoral Committee members for their constructive motivation and guidance.

I specially thank to Dr. Amol Singh, Dr. Gangadhar, Dr. Debasis & Ms. Kiranjot for several experimental help as well as for interesting discussions. Thanks are due to Mr. Rajkumar Gupta, Mr. Praveen Yadav & Mr. Pushkardeep Saxena for several help in measurements at the Reflectivity beamlines of Indus 1 & 2.

I sincerely thank Dr. D. M. Phase, Mr. A. D. Wadikar & Mr. Sharad Verma of IUC Indore for help in XPS measurements. I am also thankful to Dr. Mukul Gupta & Mr. Rakesh Shah for help in sample deposition & initial X-ray absorption measurements at BL-01 of Indus-2 Synchrotron source. Thanks are due to Dr. Sanjay Rai for providing GIXRR measurement facility.

I am also thankful to Dr. V. K Dixit, Dr. C. Mukherjee and Dr. Pankaj Mishra for help in sample preparation.

I am thankful to our collaborators- Dr. Phillpe Jonnard of Sorbonne Université, Paris, Dr. Mourad Idir of Brookhaven National Laboratory, Dr. Pascal Mercere and Paul DaSilva of Soleil Synchrotron Source, France.

I specially thank my husband Subhrokoli Ghosh for his constant motivation. Thanks are due to my sister Kuhelika Sinha, and most importantly my friends Charu, Rijul, Arindam, Subhomoy, Preeti, Dhanshree, Rajiv, and Sahadeb, who have supported me and made my stay pleasant at RRCAT, Indore.

Above all, it would have not been possible for me to achieve this milestone in my research career without encouragement and support from my all family members who have dreamed and prayed for my all around success. My Parents who hold exceptional concerned about my success has imparted a great enthusiasm at every moment.



Mangalika Sinha

Table of Contents

CHAPTER 1.	1
1.1 Introduction:	2
1.2 Correlation of optical properties with other intrinsic properties of matter	5
1.3 Tools for determination of optical constants in soft X-ray region	8
1.3.1 Reflectance spectroscopy	8
1.3.1.1 Methodology for extraction of optical constants from angle-dependent reflectivity data.	12
1.3.1.2 Methodology for extraction of optical constants from energy-dependent reflectivity spectrum	14
1.3.2 X-ray Absorption Spectroscopy	17
1.3.2.1 Methodologies for extraction of optical constants from X-ray Absorption Spectroscopy	21
1.4 Methods to check the accuracy of the investigated optical constants.	24
1.5 Oxides in X-ray optics	27
1.6 Scope of the present work	30
CHAPTER 2.	31
2.1 Introduction:	32
2.2 Indus Synchrotron Sources	33
2.2.1 Indus-1 source	33
2.2.2 Indus-2 source	35
2.3 Soft X-ray Reflectivity Beamlines	36
2.3.1 Reflectivity Beamline of Indus-1 source	37
2.3.1.1 Two-mirror harmonic suppressor system	38
2.3.1.2 Details of the reflectometer chamber	40
2.3.2 Reflectivity Beamline of Indus-2 source	41
2.3.2.1 Optical Scheme of the beamline:	41
2.3.2.2 Details of the Reflectometer chamber	43
2.3.2.3 Investigation of Higher harmonics in BL-03	45
2.3.2.4 Higher order suppressor system in BL-03:	47
2.4 Deposition Techniques	48
2.4.1 Mechanism of Sputtering	49
2.4.1.1 Reactive Sputtering Technique	50
2.4.1.2 Ion Beam Sputtering Technique	51
2.4.2 Mechanism of Evaporation Based Processes	52
2.4.2.1 Electron Beam Evaporation Technique	53

2.5	Other Characterization Techniques.....	54
2.5.1	X-ray Photoelectron Spectroscopy (XPS).....	54
2.5.2	Secondary Ion mass Spectrometry (SIMS)	58
CHAPTER 3.	61
3.1	Introduction:	62
3.2	Experimental details:.....	66
3.3	Results and discussions:	67
3.3.1	GIXRR analysis.....	68
3.3.2	Determination of Optical Constants.....	71
3.3.3	Optical constants spectra of α -Al ₂ O ₃ near Al L _{2,3} and O K-edge.....	74
3.3.3.1	Energy dependent SXR measurements.....	75
3.3.3.2	Comparison of Optical Constants of α -Al ₂ O ₃ with that of thin film	78
3.3.4.	Depth Resolved Compositional analysis of off-stoichiometric film.....	81
3.3.4.1	GIXRD analysis	82
3.3.4.2	XPS analysis.....	83
3.3.4.3	In-depth compositional study using SXR analysis	85
3.4	Conclusions.....	88
CHAPTER 4.	90
4.1	Introduction:	91
4.2	Core-hole effect and its implication on electronic structure.....	95
4.3	Experimental details	97
4.4	Results and discussions:	98
4.4.1	Surface/ Interface study of Magnesium oxide thin film.....	98
4.4.2	Investigation of optical constants of MgO thin film and its relation to electronic structure	103
4.4.2.1	Investigation of optical constants near Mg L-edge from energy-dependent SXR measurement.	103
4.4.2.2	Investigation of optical constants near O K-edge from X-ray absorption measurement.....	105
4.4.2.3	Relation between electronic structure & the investigated optical constants.....	107
4.4.2.4	Checking the accuracy of the optical constants of MgO thin film.	112
4.5	Conclusions:.....	113
CHAPTER 5.	115
5.1	Introduction:	116
5.2	Experimental details:.....	117
5.3.1	Initial Characterization: GIXRD & GIXRR.....	118

5.3.2	Investigation of optical constants of ZrO_2 covering Zr $M_{4,5}$ edge.....	121
5.3.3	Optical constants spectra of zirconium oxide thin film near the O K-edge	125
5.3.3.1	GIXRR Analysis.....	126
5.3.3.2	Energy dependent SXR measurements.....	127
5.3.3.3	Checking the accuracy of the optical constants near O K-edge of zirconium oxide thin film.....	130
5.3.4	Glancing Incidence TEY	130
5.4	Depth resolved compositional analysis using non-destructive SXR technique	133
5.4.1	XPS analysis.....	133
5.4.2	Investigation of chemical composition by SXR in qualitative manner.....	135
5.5	Conclusions:.....	139
CHAPTER 6	141
6.1	Summary and Conclusions:	142
6.1.1	Work Related to Beamline Development:	142
6.1.2	Optical studies:.....	143
6.1.3	Structural & compositional studies:	145
6.1.4	Relation of the optical constants with the electronic structure:	146
6.2	Scope of the Future Work:.....	148
APPENDIX	150
BIBLIOGRAPHY	165

List of Figures:

Figure 1-1 Schematic diagram showing interference of the reflected beam emerging from the top surface of a bilayer sample and the origin of the Kiessig fringes.	11
Figure 1-2 Schematic diagram showing the basic mechanism of the X-ray absorption spectroscopy and its utility in probing the unoccupied states and the electronic structure.	18
Figure 1-3 Schematic diagram showing different modes of X-ray absorption measurement.	19
Figure 1-4 shows the effect of ignoring (a) lower energy range and (b) higher energy range of the reflection spectrum while calculating the optical constants.	25
Figure 1-5 shows the effect of the choice of the higher energy range in the determination of optical constants (δ and β).	26
Figure 1-6 Difference in the optical constants (δ and β) values calculated using the reflectivity spectrum for two different energy ranges of 62-20,000 eV and 62-24,000 eV respectively. The upper limit of the higher energy values is different.	26
Figure 2-1 Schematic diagram of the various beamlines on Indus-1 synchrotron radiation source.....	34
Figure 2-2 Schematic diagram of the various beamlines on Indus-2 synchrotron radiation source.....	36
Figure 2-3 Schematic and actual photograph of two mirror higher order suppressor system installed at the reflectivity beamline (BL-04) of Indus-1 Synchrotron radiation source primarily used for grating 2 & 3 in the wavelength range of 120 Å-1000 Å.....	39
Figure 2-4 Comparison of the reflectivity spectra over the complete range of grating 2 & 3 of BL-04 Indus 1 with and without two mirror harmonic suppressor system. Results of similar measurement carried out at metrology beamline of Synchrotron SOLEIL are also shown.....	39
Figure 2-5 Optical schematic of the soft X-ray reflectivity beamline BL-03 of Indus-2 Synchrotron source.....	42
Figure 2-6. (a) Inside view of the reflectometer chamber (b) schematic of sample scanning stages as the sample can be scanned in x-y plane using two lateral translation stages and Z-vertical stage can be used to move the sample in and out of the beam and also to adjust samples of different thicknesses.	43
Figure 2-7 Measured (green stars) and calculated (red solid line) reflectivity pattern considering the contribution of harmonics present in the beamline.....	46
Figure 2-8. (a) Schematic of three mirror assembly for higher order suppressor (top view). Each mirrors are coated with stripes of four different materials as shown in (b). During the operation the three mirrors will set such that the stripes of same materials will remain in the beam path.	47
Figure 2-9 Schematic diagram of different processes which occurs during sputtering.	49
Figure 2-10 Schematic diagram of reactive sputtering technique.	51
Figure 2-11 Schematic diagram of ion beam sputtering technique in a single ion beam configuration.....	52
Figure 2-12 Schematic diagram of the electron beam evaporation technique	53
Figure 2-13 Schematic diagram describing referencing the work function of the sample with respect to spectrometer.....	55
Figure 2-14: Diagram of X-ray photoelectron spectrometer used for experimental purpose for this thesis.....	56
Figure 2-15 Schematic diagram of a TOF-SIMS set up.....	58
Figure 3-1 Reflectance curve of 60 layer pair Mo/Si multilayer of a period of 103 Å measured at $\lambda=138$ Å. The Bragg peak located near Brewster angle provides precise information about the polarization content.....	67
Figure 3-2 Measured (open circles) and fitted (continuous line) GIXRR spectra of aluminum oxide thin film as a function of momentum transfer vector q_z is shown. Schematic of three layer model used for the fitting is also shown.....	69
Figure 3-3 Scattering length density (SLD) profile derived by modelling the parameters obtained from the analysis of the GIXRR curve. The region of different layers is marked in the SLD profile.	69
Figure 3-4 Measured (circle) and fitted (solid line) angle dependent SXR spectra of aluminium oxide thin film are shown for different wavelengths in (a) 60-200 Å (~206-62 eV) region. (b) Near the Al L absorption edge (170Å/73 eV). For the sake of clarity the curves are vertically shifted by a constant factor as shown in the figure.	71
Figure 3-5 The measured optical constants of the aluminium oxide thin film (principal layer) are compared with the Henke's tabulated values obtained from the CXRO website for bulk density as well as for the measured density of 2.93g/cc.....	72

Figure 3-6 Comparison of (a) delta (δ) and (b) beta (β) of aluminum oxide thin film obtained from Henke, Palik, and Hagemann literature with the present experimental data.....	74
Figure 3-7 (a) Shows the reflectivity spectrum of α - Al_2O_3 measured at an incidence angle of 5° covering the Al $L_{2,3}$ edge region. (b) Shows the reflectivity spectrum near the O K-edge region measured at an incidence angle of 3°	76
Figure 3-8 (a) shows the obtained optical constants (δ & β) profile near the Al $L_{2,3}$ edge region where the features are marked from A to F. Inset shows the well resolved L_2 and L_3 edge features with a SOS of 0.4 eV. (b) shows the optical constants (δ & β) profile near the O K-edge region where the salient features are marked from A to D.	77
Figure 3-9 Comparison of the experimentally obtained optical constants δ & β of the sapphire (α - Al_2O_3) with that of the aluminum oxide thin film having a thickness of 240 Å.....	79
Figure 3-10 shows the comparison of the optical constants of sapphire crystal evaluated from angle-dependent and energy-dependent Soft X-ray reflectivity (SXR) measurements.	81
Figure 3-11 GIXRD spectrum of aluminum oxide thin film is shown. The vertical dotted line represents the peak positions of aluminum (Al) & aluminum oxide (Al_2O_3).	83
Figure 3-12 XPS spectra of Al2p, 2s & O 1s core levels of aluminum oxide thin film measured after sputtering for 10 minutes. Sputtering leads to removal of the top contamination layer.	84
Figure 3-13 Optical index profile (a) δ and (b) β for AlO_x ($x=1.6$), Al_2O_3 are calculated for 2.93 g/cm ³ and 3.97 g/cm ³ density respectively and compared with experimentally measured profile of aluminum oxide thin film. The combination of 50% AlO_x ($x=1.6$) + 50% of Al_2O_3 gives best fit to the experimental data.....	86
Figure 3-14 Optical index profile (a) δ and (b) β for interfacial layer formed at film/substrate interface. The experimental profile matches reasonably well with 25% SiO_2 and 75 % AlO_x ($x=1.6$) composition.....	87
Figure 4-1 Schematic representation of the formation of core-exciton state as a consequence of core-hole effect (a) shows the ground state of MgO (b) shows the transition state where formation of core-exciton state occurs & (c) shows the final effect of core-hole.....	97
Figure 4-2 Measured (star) and fitted (continuous solid line) angle dependent soft X-ray reflectivity curve of magnesium oxide (MgO) thin film over the wavelength range of 120-190 Å.....	100
Figure 4-3 Secondary ion mass spectroscopy (SIMS) spectra of magnesium oxide (MgO) thin film.	101
Figure 4-4 In-depth optical density profile obtained from modelling the soft X-ray reflectivity data. Inset shows the Henke tabulated delta values in the wavelength range of 120-190 Å for bulk Mg_2SiO_3 , SiO_2 , and Mg_2Si	102
Figure 4-5 Measured reflectance spectrum of an MgO thin film at a fixed glancing angle of $\theta = 5^\circ$ in the energy range 40–300 eV. The inset shows thereflectance spectra neat the Mg L-edge.....	104
Figure 4-6 Measured values of (a) delta (δ) and (b) beta (β) obtained from the KK analysis of reflectivity versus photon energy data are compared with tabulated values obtained from the CXRO database. The inset shows the 40–100 eV region where several fine features are evident.	105
Figure 4-7 Experimental X-ray absorption spectra of MgO thin film measured near O K-edge in total electron yield mode scaled with respect to the Henke tabulated beta values taken from CXRO database.....	107
Figure 4-8 Measured values of delta (δ) obtained from the KK analysis of beta (β) values as obtained by scaling of total electron yield spectra with respect to Henke tabulated data. Comparison of the measured delta (δ) values with the Henke data available in CXRO database is also shown.	108
Figure 4-9 X-ray absorption spectra of 500-Å-thick MgO thin film and that of a MgO substrate measured in total electron yield mode near the O-K absorption edge region.	110
Figure 4-10 Experimental absorption spectra of MgO near the Mg $L_{2,3}$ -edge shown along with the theoretical spectra. The experimental spectra match well with the theoretical spectra obtained by considering the core-hole effect.	111
Figure 4-11 Calculated partial density of states (PDOS) of MgO in the absence of a core-hole.....	113
Figure 4-12 Comparison of the measured energy-dependent soft X-ray reflectivity spectra at incidence angles of 5° with the simulated one.	114
Figure 5-1 Measured (circle) and fitted (solid line) GIXRR spectra of ZrO_2 thin film for $\lambda=1.54$ Å are shown.....	120
Figure 5-2 Variation of Scattering length density (SLD) with respect to thickness as derived from the GIXRR fit of the measured data of ZrO_2 thin film is shown. Schematic of the three-layer model used for the fitting is also shown.	122

Figure 5-3 Measured (circle) and fitted (solid line) SXR curves of ZrO_2 thin film are shown for different incident wavelengths in the 55–150 Å wavelength region. Reflectivity data are fitted with the same model used in GIXRR data analysis. Curves are vertically shifted for the sake of clarity.....	123
Figure 5-4 Measured (circle) and fitted (solid line) angle-dependent SXR curves of ZrO_2 thin film near the Zr $M_{4,5}$ edge are shown. Curves are vertically shifted for the sake of clarity.....	124
Figure 5-5 $\beta\delta$ ratio for experimentally derived optical constants (in circle) along with the $\beta\delta$ ratio for Henke's tabulated values (in solid line) are shown.	125
Figure 5-6 Experimentally measured optical constants of ZrO_2 thin film are shown as discrete points along with the error bars. In the inset, optical constants near the Zr $M_{4,5}$ edge are shown.....	126
Figure 5-7 Real and imaginary parts of atomic scattering factor f_1 and f_2 , respectively, are plotted in the 80-240 eV (within 55–150 Å) energy region for Zr and O as obtained from the CXRO website.	127
Figure 5-8 (a) Measured (scatter) and fitted (solid line) GIXRR curves of as-deposited 500 Å ZrO_2 thin film. The curves are vertical shifted for clarity. (b) Variation of delta (δ) along the depth of the as-deposited 500 Å. ZrO_2 films obtained from the modelling of the GIXRR data.	129
Figure 5-9 Shows the reflectivity spectrum of ZrO_2 measured at an incidence angle of 2° covering the O K-edge region.	131
Figure 5-10 Measured values of delta (δ) & beta (β) obtained from KK analysis of reflectivity versus photon energy data near O K-absorption edge.....	131
Figure 5-11 X-ray absorption spectrum (XAS) of ZrO_2 thin film measured in total electron yield mode at normal incidence geometry.....	132
Figure 5-12 Comparison of the measured energy-dependent soft X-ray reflectivity spectra at incidence angles of 2° with the simulated one.	133
Figure 5-13 Total electron yield (TEY) spectra of zirconium oxide thin film measured at an glancing angle of 3 & 5 degree respectively.....	134
Figure 5-14 (left) Measured (red scatter) and simulated (blue short dot dash) total electron yield spectra considering the contribution of electrons originating from both resonant and non-resonant absorption processes separately. For a complete understanding we have also plotted our experimentally obtained beta (β) spectra normalized wrt the TEY spectra.(right) the behavior of the resonant and the non-resonant contribution along with the net total electron yield contribution covering the O K-edge of off-stoichiometric zirconium oxide thin film. The parameters of the simulated TEY spectrum are $\tau_{\text{res}}=0.05$ and $\tau_{\text{res}}=0.95$, with the electron escape length of 10 Å. The energy scale of the simulated spectra is shifted to a certain value which is well within the energy resolution of beamline.	135
Figure 5-15 XPS spectrum of zirconium dioxide thin film at Zr 3d and O 1s core levels for as-deposited and 10 min sputtered film. The spectra are deconvoluted using Gaussian de-convolution method and two different phases of ZrO_x and ZrO_2 are identified along with the presence of oxygen.	138
Figure 5-16 In-depth optical index profiles of 450 Å zirconium oxide thin film using $\lambda=64$ Å, 80 Å, 100 Å, 120 Å and 150 Å wavelengths are shown. The different regions in the film are marked.	139
Figure 5-17 Optical constant profile for zirconium oxide thin film as a function of energy over 225-82 eV (55–150 Å) region. CXRO data for $\text{Zr}_{0.8}\text{O}_{2.2}$ and ZrO_2 are also plotted for comparison. Composition consisting of 60% ZrO_2 and 20% $\text{Zr}_{0.8}\text{O}_{2.2}$ & 20% oxygen vacancies gives the best fit to the experimentally obtained data.	141
Figure 5-18 Optical constant profile for interfacial layer of zirconium oxide thin film as a function of energy over 225-82 eV (55–150 Å) region. CXRO data for Ga_2O_3 , As_2O_3 and ZrO_2 are also plotted for comparison. Composition consisting of 20% As_2O_3 along with 25% Ga_2O_3 , 35% ZrO_2 and 20% oxygen vacancies gives the best fit to the experimentally obtained data.	142

List of Tables:

Table 2-1: Parameters of Indus-1 synchrotron radiation source.	33
Table 2-2: Parameters of Indus-2 synchrotron radiation source.	35
Table 2-3: Parameters of BL-04 of Indus-1 synchrotron radiation source.	37
Table 2-4: Parameters of BL03 beamline optical elements.....	41
Table 2-5 Structural parameter of the W/B ₄ C multilayer used for investigation of harmonic content	46
Table 3-1 Structural parameter of the aluminum oxide thin film from GIXRR analysis.....	68
Table 3-2: Measured values of optical constants of off stoichiometric aluminum oxide thin film are listed along with Henke's tabulated values of Al ₂ O ₃ for reduced density 2.93 g/cc in the 60–200 Å (~206-62 eV) region	73
Table 3-3. Elemental concentration for different sputtering cycle obtained from the XPS spectra of Al 2s and O 1s core levels	84
Table 4-1 Structural parameter of the magnesium oxide thin film obtained from angle-dependent SXR.	101
Table 5-1 Structural parameters of ZrO ₂ thin film deposited on GaAs substrate as obtained from GIXRR analysis.	121
Table 5-2 Experimental and tabulated optical constants of ZrO ₂ in the 55-150 Å wavelength region (~225-82 eV).....	124
Table 5-3 Structural parameters of different layers of the as-deposited 500 Å ZrO ₂ film as obtained from the analysis of the GIXRR data.	129
Table 5-4: Percentage contribution of various phases obtained from de-convolution of XPS spectra from Zr 3d and O 1s respectively.....	137

Chapter 6

Summary, Conclusions and Future Scope

This chapter deals with the summary and important findings of this thesis. The future scope of the present work is also highlighted.

6.1 Summary and Conclusions:

The present thesis deals with the evaluation of optical behavior of three important oxides: aluminum oxide, magnesium oxide & zirconium oxide which are widely used as optical elements for different Soft X-ray optics applications. The evaluated optical constants in the Extreme ultraviolet (EUV)/Soft X-ray region are the crucial parameters for determining the reflectivity performance of optical elements of such materials. The thesis also deals with the correlation of the optical constants with the material's structural parameters, chemical composition, stoichiometry and the electronic structure. Most of the investigation of the present thesis has been carried out using the reflectivity beamlines BL-04 & BL-03 of the Indus-1 & Indus-2 synchrotron radiation sources respectively.

Below, the crucial findings of the present thesis are summarized along with the future scope of this work.

6.1.1 Work Related to Beamline Development:

Reflection optics based harmonic suppressor system comprised of two parallel mirrors is installed and optimized on reflectivity beamline BL-04 of Indus-1 SR source. In order to suppress the higher harmonics in 120-1000 Å wavelength region a pair of polished silicon mirror was used and set on optimized angle (5-20 degree range). The performance of the HOS system was checked by measuring R vs wavelength spectra of α -Al₂O₃ with & without the HOS system. The reflectivity in the 360-100 Å wavelength region (grating 3) remains almost constant to the value of 85% with no features using the two mirror HOS. On the other hand, without the presence of the two mirror suppressor system the reflectivity diminishes upto 20% in the grating-3 and several unwanted features are observed. The reflectivity performance with HOS setup was

compared with the data obtained on same sample from metrology beamline of Synchrotron SOLEIL, and found both matches well in the Grating 2 region.

The harmonic content of the Soft X-ray Reflectivity beamline (BL-03) of Indus-2 Synchrotron Radiation Source is estimated using a W/B₄C multilayer of 36.5 Å period and 100 layers for photon energy range of 600-1000 eV. A three mirror based HOS system for this beamline is in fabrication and will be installed in near future. Different edge filters are presently being used for harmonic suppression

The energy calibration of the beamline in the Grating 3 (~400-1600 eV) is carried out by tracing the shift of the Bragg peak position from the expected/simulated position. The energy offset with respect to the set value is found to be linear in nature and can be easily estimated from the slope and the intercept value as obtained from the linear fitting.

6.1.2 Optical studies:

Optical behaviors of three oxides Al₂O₃, MgO & ZrO₂ are analyzed in the EUV/ Soft X-ray region covering the absorption edges of their respective constituent elements. The investigation has been carried out using the angle-dependent & energy-dependent reflectivity measurements.

For aluminum oxide thin film deposited using Al target, the optical constants are investigated in the 60-200 Å (~206-62 eV) range covering the Al L-edge region. The experimentally obtained δ & β values are found to be 5-33% higher than the tabulated Henke's values for reduced density alumina of 2.93 g/cc. Near Al L- absorption edge, δ are 50-120% higher whereas β are lower by 7-20%. An increase in delta values and a decrease in beta values are possible if unreacted Al and oxygen are present in a significant amount. Such films grown using reactive sputtering method may be useful as a spacer layer in multilayer optics because of the lower value of the absorption

(β). The optical constants of the thin film obtained at few discrete photon energies by R vs angle method are compared with optical constants spectra of crystalline α -Al₂O₃ obtained from R v/s photon energy method in small steps of 0.1 eV. The L₂ and L₃ features are found to be well-resolved in both dispersion (δ) and absorption (β) curve with an energy separation of 0.4 eV.

The optical constants of magnesium oxide thin film deposited using MgO target (IBS) are investigated using energy-dependent reflectivity technique in 42-310 Å (~300-40 eV) range covering the Mg L-edge. Below the Mg L-edge region, the experimentally obtained delta (δ) values are found to be higher by ~20-50% with respect to the Henke tabulated values (corresponding to bulk density) making it suitable for use in this region. In the higher energy region far away from the Mg L-edge (140-300 eV) the deviation in delta (δ) is ~5-10%, while for beta (β) values the experimental values are found to be higher by ~5-20%. At the Mg L-edge region a drastic increase in the experimental δ values (~45%) as compared to the Henke tabulated one is observed. While for the experimental β values the deviation extends upto ~30%. Experimental value of Mg L-absorption edge is found to be 52.8 eV because of chemical shift associated with Mg-O bonding which is missing in Henke database.

The optical constants of zirconium oxide film deposited using ZrO₂ target on GaAs substrate are investigated in the 50-150 Å (~250-80 eV) range covering the Zr M-edge at discrete photon energies. The experimentally obtained δ and β values above the Zr M_{4,5} edge region 150-70 Å (~80-177 eV) are found to be lower by 1- 24 % as compared to tabulated Henke's values. Below the Zr M_{4,5} edge region the measured β values are higher by 1-20% whereas the delta values are lower than the Henke values. This could be understood if the behaviour of atomic scattering factors for Zr and O are separately analysed. The real and imaginary part of the atomic scattering factor shows that the f₂ values of Zr and O are very close in 50-150 Å (~250-80 eV)

range, whereas the f_1 values of these two elements are significantly different. This suggests that the change in Zr: O ratio (due to presence of oxygen and voids) does not affect the beta values much, but it lowers the delta values significantly. Thus the presence of oxygen vacancies with change in Zr: O ratio as discussed below attributes to this deviation in optical constants.

We have also investigated the fine optical constants profile covering the O K-edge region of zirconium oxide thin films of different thicknesses & densities deposited on Si substrate. The obtained fine absorption (β) and dispersion (δ) profile correlate well with the electronic structure of the film showing the e_g & t_{2g} feature.

6.1.3 Structural & compositional studies:

In this thesis work, the initial characterization of the structural parameters, like determination of thicknesses and roughnesses & the densities of the three different oxide thin films are carried out using X-ray reflectivity measurements (R vs. θ). The chemical composition of the film, surfaces and interface are investigated using X-ray Photoelectron Spectroscopy (XPS).

Density of the aluminum oxide film of 240 Å thickness is found to be 2.93 g/cc, which is 73% of the bulk density (3.93 g/cc). The Scattering length density (SLD) profile obtained from the modelling of reflectivity data indicates about the presence of interlayer whose composition is different from the substrate native oxide. The thickness of this interlayer is found to be 18 Å. To investigate the qualitative composition of the principal as well as the interfacial layer the optical modelling of the optical constants profile is carried out. It is estimated that the principal layer consists of 50% AlO_x ($x=1.6$) and 50% Al_2O_3 , while the interfacial layer consists of 25% SiO_2 and 75% AlO_x ($x=1.6$). The intermixing of these two leads to form an aluminum silicate compound at the interface region. The composition of the principal layer corroborates well with the XPS data. Analysis of the XPS spectra ensures the presence of two different phase of

aluminum oxide at the principal layer. The off-stoichiometric nature of the film, with increased oxygen content as compared to Al confirms the fact that the optical constants δ (δ) is found to be higher while β (β) is found to be lower as compared to Henke tabulated value at a density of 2.93 g/cc.

For the magnesium oxide thin film deposited on Si substrate, the optical density profile obtained from SXR analysis confirms the presence of Mg-Si-O and Si-O layers at the film/substrate interface. In-depth profile of the film as obtained from SIMS has also been found to be consistent with in-depth optical density profile.

Density of the 467 Å thick zirconium oxide thin film deposited on the GaAs substrate is found to be 4.50 g/cc (80% of the bulk density of 5.68 g/cc). The composition of ZrO_2 film is qualitatively estimated by modelling the optical constant profile over 50-150 Å wavelength region. The principal layer is estimated to be composed of 60% ZrO_2 , 20% ZrO_x & the remaining part consists of oxygen vacancies. From XPS analysis it is confirmed that the peak position of Zr 3d & O 1s corresponds to ZrO_x & ZrO_2 phases. The optical constant profile of the interfacial layer matches well by considering a composition of 20% As_2O_3 along with 25% Ga_2O_3 , 35% ZrO_2 and 20% oxygen vacancies. The presence of voids ensures the variation in Zr:O ratio which affects the atomic scattering factor and simultaneously the optical constants

6.1.4 Relation of the optical constants with the electronic structure:

We have observed and analyzed the fine features in optical constants profile (both dispersion δ & absorption β) of $\alpha\text{-Al}_2\text{O}_3$ in the energy range of 45-150 eV from energy dependent reflectivity measurement. Various fine features corresponding to the absorption edge and various other transitions occurring from the Al 2p to other states are visible in the optical constants profile. Two well resolved peaks corresponding to the L_2 & L_3 absorption edge of Al are located at an

energy position of 78.0 eV & 78.4 eV respectively. These are also termed as Al $L_{2,3}$ excitonic features. The spin orbit splitting is found to be 0.4 eV and is visible in both δ & β .

For MgO thin film the fine features are evident in both dispersion (δ) and absorption (β) profile in the 40-100 eV region near the Mg L-edge energy. All the higher energy features (above 60 eV) marked from root from the transition of Mg p to Mg s, d and hybridized states of Mg s and O s states respectively as observed from the calculated partial density of states (PDOS) and literature data. However, the features marked as 'a' & 'b' located at 52.8 eV & 54.4 eV (see Figure 4-6, Chapter -4) are found to originate as a consequence of core-hole excitonic effect as shown from the calculation of Mg L- edge absorption spectrum with & without considering core-hole.

For ZrO_2 thin film, the optical constants profiles near the O K-edge region are extracted from the analysis of energy-dependent reflectivity data. The e_g and t_{2g} features originating as a consequence of crystal field effects is well evident in both the dispersion & absorption profile.

For zirconium oxide, we could not observe core-hole effect in the optical constants as measured near the Zr $M_{4,5}$ edge and O K-edge. Thus, it is very important to understand the factors related to the occurrence of the core-hole feature in the optical constants spectra. Some of the solid state phenomena like crystal field effect, covalency and distortion might play an important role in the appearance of a core-hole feature. For 3d and 4d transition metals like Ti^{4+} and Zr^{4+} in their oxides, the crystal field effect is pronounced as a result of which the core-hole potential is much weaker as compared to the crystal field and thus we do not observe any core-hole peak. Whereas in case of Al^{3+} and Mg^{2+} in their oxides there are no 3d electrons and the p electrons being more delocalized don't show any crystal field effect as a result of which the core hole potential is

dominating in the XAS spectra. Detailed understanding can be achieved on investigation of optical constants of metal oxides having different exotic solid state properties.

Fine features reported in the thesis is an important finding as Henke tabulated database does not show such features therefore our experimental data is more useful for practical applications particularly for X-ray optics community.

6.2 Scope of the Future Work:

The information of optical behavior of three oxides investigated in the present thesis work will be useful in calculation/ simulation of reflectivity performance of the oxide/ Metal multilayer combination in the EUV/ soft X-ray region. The formation of various interfaces and varied chemical composition /stoichiometry as analyzed from the present thesis can be taken into account while simulation.

The present work can be continued to study the optical constants of the three oxides deposited using different deposition techniques e.g. e-beam evaporation, ion beam sputtering, pulse laser deposition etc. This will help in understanding the role of each deposition techniques on structure, composition and stoichiometry of oxide thin films and resultant effect on X-ray optical properties. Moreover, films of different thicknesses for e.g. ultrathin films used as capping layer and moderate thin films used as mirror coating etc. have several X-ray optics applications. However, for thin film of same material but different thickness, density and other physical properties may be different. Thus, in future we would like to do a comparative study on the films of different thicknesses to understand the growth mechanism and its influence on the optical properties of thin films of compound materials.

Moreover, it is known that PVD growth methods can produce textured thin films. Thus if there is a crystal face dependence of optical constants, knowing the exact texture of these films would be important. This work could be continued in future.

We also hope to understand the effect of the different co-ordination geometry like octahedral, tetrahedral etc. on the optical properties of oxide thin films. It is known that in accordance with the co-ordination geometry, the crystal field splitting differs and thus the dispersion and absorption features near the edge region reflects all these.

As discussed in the last part of the Section 6.1.4, there is a lot of scope in the detailed understanding of the different factors like crystal field splitting, covalency, distortion and other material properties responsible for the disappearance of the core-hole feature in few oxides.

Finally, the present work can be continued to study the optical properties near the K-edges of the constituent 1st element of oxide.

Summary

Synchrotron and Free electron laser (FEL) beamlines emanating X-rays of broad range of energies are widely used all over the world for various cutting edge research purposes and the heart of these beamlines is its optical elements. The main criterion of the selection of these optical elements is based on the optical properties of the material in the working energy range along with its thermal stability and radiation tolerating ability. Oxide material having high mechanical and thermal stability mostly satisfies these criteria. There are several literatures on fabrication and optical performance of optical elements like multilayer mirrors, Fresnel's zone plate, Laue lens etc. where oxides are abundantly used. However, for understanding their optical performance, X-ray optics community still relies mostly on the Henke tabulated optical constants database available on CXRO website which has several limitations. The present thesis deals with the evaluation of optical constants of three important oxides: aluminum oxide, magnesium oxide & zirconium oxide which are widely used as optical elements for different Soft X-ray optics applications. The thesis also deals with the correlation of the optical constants with the material's structural parameters, chemical composition, stoichiometry and the electronic structure.

For aluminum oxide thin we determined the optical constants (δ & β) experimentally are found to be 5-33% higher than the tabulated Henke's values for reduced density alumina of 2.93 g/cc as determined from GIXRR measurement. Near Al L- absorption edge, δ are 50-120% higher whereas β are lower by 7-20%. We have also evaluated the optical constants profile of α -Al₂O₃ covering Al L_{2,3} edge and O K-edge where there is appearance of the excitonic like feature as stated in literature. On comparison of the optical constants of the thin film with that of α -Al₂O₃

we found that δ & β of the film is slightly lower than that of α -Al₂O₃. The lower value of the absorption (β) indicates the suitability of the thin film as a spacer layer for a multilayer mirror.

For magnesium oxide thin film deposited using MgO target (IBS), the optical constants are investigated in 42-310 Å (~300-40 eV) range covering the Mg L-edge using energy-dependent reflectivity. The experimentally obtained delta (δ) values are found to be higher by ~20-50% the with respect to Henke tabulated values (corresponding to bulk density) below the Mg L-edge making it suitable to use in this region. In the higher energy region far away from the Mg L-edge (140-300 eV) the deviation in delta (δ) is ~5-10%, while for beta (β) values the experimental values are found to be higher by ~5-20%. At the Mg L-edge region a drastic increase in the experimental δ values (~45%) as compared to the Henke tabulated one is observed. While for the experimental β values the deviation extends upto ~30%. Experimental value of Mg L-absorption edge is found to be 52.8 eV because of chemical shift associated with Mg-O bonding which is missing in Henke database.

For zirconium oxide film deposited using ZrO₂ target on GaAs substrate, the optical constants are investigated in the 50-150 Å (~250-80 eV) range covering the Zr M-edge at discrete photon energies. The experimentally obtained δ and β values above the Zr M_{4,5} edge region 150-70 Å (~80-177 eV) are found to be lower by 1- 24 % as compared to tabulated Henke's values. Below the Zr M_{4,5} edge region the measured β values are higher by 1-20% whereas the delta values are lower than the Henke values. This could be understood if the behaviour of atomic scattering factors for Zr and O are separately analysed. The real and imaginary part of the atomic scattering factor shows that the f₂ values of Zr and O are very close in 50-150 Å (~250-80 eV) range, whereas the f₁ values of these two elements are significantly different. This suggests that the change in Zr: O ratio (due to presence of oxygen and voids) does not affect the beta values

much, but it lowers the delta values significantly. Thus the presence of oxygen vacancies with change in Zr: O ratio as discussed below attributes to this deviation in optical constants.

We have also investigated the fine optical constants profile covering the O K-edge region of zirconium oxide thin films of different thicknesses & densities deposited on Si substrate. The obtained fine absorption (β) and dispersion (δ) profile correlate well with the electronic structure of the film showing the eg & t2g feature.

Chapter 1.

Introduction

This chapter gives a general overview of the complex refractive index in X-ray region which are defined in terms of “optical constants”. A brief introduction to the X-ray reflectivity and absorption spectroscopy techniques are given which are useful for the investigation of these optical constants in Extreme ultraviolet (EUV) and Soft X-ray region. The implementation of methodologies like conventional Kramers-Kronig (KK) relation, double subtracted KK relation in the extraction of optical constants along with the challenges involved is described. The importance of investigation of optical constants is described along with the application of oxide materials as optical elements in synchrotron beamlines. Finally the scope of the work is presented.

1.1 Introduction:

The discovery of X-rays in the year 1895 and its further development has opened up the path of various forms of researches which were not possible until the previous century. With the short wavelength property as compared to the other part of the electromagnetic spectrum several microscopic properties of the material can be investigated using X-rays. However, the X-ray region of the electromagnetic spectrum is quite broad, ranging from 0.01 nm to 10 nm in terms of wavelength and 100 eV to 120 keV in terms of energy. Thus, in terms of wavelength or energy range they can be roughly classified as- Hard X-rays & Soft X-rays. The X-rays with photon energies above 5 keV are called Hard X-rays and have much shorter wavelengths, while those with lower energies from 100 eV to 5 KeV and comparatively higher wavelengths are called soft X-rays. Below the soft X-ray region, there exists the extreme ultraviolet region (EUV) with photon energies ranging from 20 eV to 100 eV. The response of a material in the EUV/Soft X-ray region is strikingly different from the remaining part of the electromagnetic spectrum. This can be well understood from the well-known response function- “refractive index”. In general form, it can be written as: $N = n + i\beta$, where n is the real & β is the imaginary part of the complex refractive index N . The real part of the refractive index indicates dispersion behavior of a material with respect to its interaction with the probing photon energy, while the imaginary part indicates its absorptive behavior. From a semi-classical approximation, the expression of refractive index¹ in X-ray region can be written as-

$$N(\omega) = 1 - \frac{e^2 n_a}{2m\epsilon_0} \sum_s \frac{g_s}{(\omega^2 - \omega_s^2) + i\gamma} \dots\dots\dots (1-1)$$

where n_a is the atomic density of the material, g_s is the oscillator strength, ω_s is the resonant frequency of the oscillator ‘s’, e & m are the charge & mass of an electron, ϵ_0 is the electric

permittivity of the medium & γ is the damping factor and is related to the losses occurring inside the medium. The most important approximation accounted in this expression is that the frequency of the X-rays is higher as compared to the others parts (IR, visible, UV) of the electromagnetic spectrum. Thus, one obtains Equation (1-1) by introduction of binomial expansion in the generalized expression of refractive index valid for low energy region of the electromagnetic spectrum.

The origin of this expression is based on the forces acting on a system of electrons bound to the nucleus. The whole system is under the influence of the fields of an electromagnetic wave passing through the material. Thus the dispersion & absorption behavior of a material under the interaction of X-rays is provided from its refractive index. This becomes more interesting since the absorption edges of most of the elements lies in the EUV and X-ray region of the electromagnetic spectrum.

In simplified form refractive index in X-ray region can also be written as-

$$N(\omega) = 1 - \frac{r_e n_a c^2}{2\pi\omega^2} [f_1^0(\omega) - if_2^0(\omega)] \dots\dots\dots (1-2)$$

Where c is the speed of light in vacuum, r_e is the classical electron radius given by $r_e = \frac{e^2}{4\pi\epsilon_0 m_e c^2} = 2.817 \times 10^{-5} \text{ \AA}$, $f_1^0(\omega)$ & $f_2^0(\omega)$ are real and imaginary part of an important physical term known as atomic scattering factor. The atomic scattering factor is the Fourier transform of the electron density distribution.² For X-rays, the scattering factor is proportional to the atomic number of the element or the total number of electrons in a material. It is also dependent on the scattering angle, however the scattering contribution at angles other than $\theta=0$ (forward scattering) is negligible because of predominance in destructive interference. For the forward scattering case, the scattering factor tends to the atomic number of the element.³

In terms of the optical constants δ & β , the refractive index can be written as $N = 1 - \delta + i\beta$, where,

$$\delta = \frac{r_e n_a c^2}{2\pi\omega^2} f_1^0(\omega), \beta = \frac{r_e n_a c^2}{2\pi\omega^2} f_2^0(\omega) \dots \dots \dots (1-3)$$

Both δ & β are of the order of 10^{-2} - 10^{-6} and is critically dependent on the energy and the other sample property. Generally, away from the absorption edge region, $\beta < \delta$, but near the edges due to predominance of absorption, $\beta \approx \delta$.

In X-ray region there is scarcity of the available data of the optical constants which are very important for understanding the optical properties of the material. The standard available database is the Henke tabulated one⁴, which contains information about the optical constant β of all the elements with atomic number $Z=1-92$, investigated from transmission measurements. In the next step, the optical constant δ is extracted by applying Kramers-Kronig relation.

The information about the optical constants of compound materials in X-ray region is not easily available. The more common approach adopted for compounds is the weighted average method where weighted contribution of atomic scattering factors of constituent elements are taken into account. However, there are several flaws in this method. For example, the actual density of the material is not considered, rather individual densities of the constituent elements are taken, with individual stoichiometric ratios as weighted factors. Thus, this approach is found to be well validated away from the absorption edges of the constituents of the compound but near the absorption edges the situation is worse. The local chemical environment of the atoms forming the bond has to be taken into account for the correct near edge results which is absent in the weighted average approach. Thus, experimental determination of optical constants of compounds in the X-ray region, especially near the absorption edge is a prerequisite task.

Several techniques like ellipsometry^{5,6}, interferometry⁷, reflectivity^{8,9}, absorption measurements^{10,11} etc. can be used for the determination of optical constants. However, each of these techniques is advantageous near a certain energy range of the electromagnetic spectrum.

Another important thing which we often overlook is the relation between the optical constants and the structural parameters, electronic states and also the surface and the interfaces of the sample. There are several techniques like Electron Microscopy, Secondary Ion Mass Spectroscopy (SIMS), Rutherford Backscattering Spectroscopy (RBS), X-ray Photoelectron spectroscopy (XPS) to probe sample surface, interface, elemental composition, each with its individual pros and cons. The primary disadvantages of these techniques are either they have lower probing depth or in most cases they are destructive in nature. On the other hand, X-ray reflectivity proves to be an interesting technique which can probe surface, interfaces as well as provide a wide plethora of information about the film density, structural parameters like thickness & roughness along with their optical constants in the measuring energy range in a non-destructive manner.^{12,13,14,15} This powerful technique is capable of evaluating the optical constants along with understanding its relation with the other intrinsic properties.

1.2 Correlation of optical properties with other intrinsic properties of matter

Optical properties of the materials in the X-ray region are represented by energy-dependent optical constants δ & β as defined earlier. There are evidences available in the literature which confirms the fact that optical constants are not only critically dependent on energy but also on the electronic structure, chemical environment and bonding, density and most importantly on the

growth conditions.^{16,17,18} In this section we will discuss how the optical constants in soft X-ray region are related to the other properties like electronic structure, composition etc.

In the introduction part we have already discussed about the origin of refractive index under semi-classical approximation and the physical significance of the real & imaginary part of it. Talking about the relation with electronic structure, these begin with the very basic rule of time-dependent perturbation theory of quantum mechanics- the “Fermi Golden Rule” which will finally provide us the concept of refractive index in quantum mechanical term. According to this rule, the transition rate from initial energy state to a group of energy states in a continuum (or final state), as a result of a weak perturbation is given as-

$$\Gamma_{i \rightarrow f} = \frac{2\pi}{\hbar} |\langle f | H' | i \rangle|^2 \rho(E_f) \dots\dots\dots (1-4)$$

where, $\langle f | H' | i \rangle$ are the matrix element of the perturbation H' between the final and the initial states and $\rho(E_f)$ is the density of states at the energy E_f of the final state. The perturbation in this case is the electromagnetic wave or X-rays impinging on the solid. The perturbation Hamiltonian can be written as²-

$$H' = -\frac{e}{mc} \vec{A}(\mathbf{r}) \cdot \vec{p} + \frac{e^2}{2mc^2} A^2(\mathbf{r}) \dots\dots\dots (1-5)$$

Where, the 1st term represents absorption and the 2nd term represents scattering, both of which are closely related to the optical constants δ & β , $\vec{A}(\mathbf{r})$ is the vector potential of the incident field and \vec{p} is the linear momentum of the interacting electrons. The transition rate as expressed in Equation (1-4) gives the number of photons absorbed per unit time and volume i.e., the power lost by the field per unit volume of the material. Power loss from the field can also be expressed in terms of imaginary part of the dielectric constant. We can express the rate of decrease in energy of the incident beam per unit volume as¹⁹-

$$-\frac{dI}{dt} = -\frac{dI}{dx} \frac{dx}{dt} = \frac{\omega \epsilon_i I}{N^2} \dots \dots \dots (1-6)$$

Where, $I = -\frac{N^2}{8\pi} |\vec{E}|^2$, \vec{E} being the electric field of the electromagnetic wave and N is the refractive index of the medium. Thus the imaginary part of the dielectric constant representing absorption is directly proportional to the transition rate which consists of information about the electronic structure of the material in terms of its density of states as well as the matrix elements depicting the final and initial state wave functions participating in the transitions.¹⁹

When the photon energy impinging on the sample matches or is greater than the binding energy of the core-levels of the constituent elements present, a photoelectron is ejected. This process is followed by the generation of a core hole which has a finite lifetime resulting in energy broadening. This fact is a consequence of the well-known Heisenberg's uncertainty principle. In case of insulating sample, the number of free electrons being less, the core hole formed gets screened effectively by the presence of the surrounding electron cloud leading to the formation of bound excitonic like states. In other words, the Coulomb interaction between the excited electron and the core-hole formed results in the formation of exciton like state, whose energy depends on the strength of the Coulomb interaction.^{20,21,22} Now, the final state will be a combination of the final orbital state along with the contribution of this excitonic state which modifies the transition rate as evident from "Fermi Golden Rule". These excitonic states will have a strong influence on the overall absorption which is related to transition rate. Moreover, the oscillator strengths for transitions at higher energies will be modified to a large extent. The creation of excitonic like features results in the appearance of sharp features near the absorption threshold, modifying the optical constants near the absorption edge region. Thus, from the fine optical constants spectra covering the absorption edge of any material we can understand the electronic structure from the transitions occurring between several states.

Besides electronic structure, optical constants of a material are highly dependent on the deposition technique, composition or stoichiometry, structure and density of the film.²³ For example, in case of a compound material like ZrO_2 if we are using Zr target and grow films under different oxygen flow, the density of the films differs from that of the bulk density resulting in different optical properties.^{24,25,26} Soufli et al.²⁷ determined the atomic composition of the magnetron sputtered boron carbide films from its optical constants profile utilizing the density as determined from another complementary technique. In their case, the atomic composition of the B_4C film consists of 74% boron 20% carbon and 6% oxygen and with the change in composition the optical constants changes accordingly. Filatova et al.²⁸ also demonstrated the effect on optical constants of HfO_2 thin films as a result of two different deposition techniques- MOCVD and ALD.

From the above discussion, we conclude that for real applications it is necessary to investigate the optical constants & understand the relation between the optical properties with the other physical properties of matter.

1.3 Tools for determination of optical constants in soft X-ray region

1.3.1 Reflectance spectroscopy

In soft X-ray region there are several techniques available to investigate optical constants such as reflectivity, absorption, electron energy loss spectroscopy etc. However, in this thesis we have exploited the X-ray reflectivity technique for the determination of optical constants due to its advantage over several other techniques.

X-ray reflectivity measurements are performed in two different modes: Angle-dependent & Energy-dependent. Angle-dependent reflectivity mode can precisely determine the structural parameters of a layered structure along with the optical constants at discrete photon energies.

^{29,30,31,32,33} From measurements we obtain reflectivity v/s incidence angle (θ) or in terms of z-component of momentum transfer vector q_z . From the obtained data one can extract the information about the variation of density (or scattering length density) along the depth of the film (along z-direction) by modelling.^{34,35} However, this technique involves lot of modelling and effort in computations. Using energy-dependent reflectivity measurements one can obtain fine spectra of dispersion and absorption by applying “Kramers-Kronig relations”.^{36,37,38,39,40}

The importance of this technique lies in the fact that it- provides information about thickness with Å-resolution, non-destructive in nature, element specificity especially near the absorption edges. However, there are certain disadvantages associated with this technique such as one does not generally obtain unique result without any pre-knowledge of the sample layer structure.

The theory of reflectivity can be understood from both dynamical as well as kinematical scattering theory.^{35,41} The kinematical scattering theory works under the Born Approximation⁴² and under this the multiple scattering effects are usually neglected and the reflected intensity is given by the Fourier transformation of the derivative of the electron density. But this approximation fails as, $q_z \rightarrow 0$. Thus, the dynamical scattering theory comes into the picture where multiple scatterings are taken into account.

For a flat, smooth and homogeneous vacuum/substrate interface the reflection co-efficient is given by Fresnel’s formula as-

$$r_s = \frac{\sin\theta - \sqrt{N^2 - \cos^2\theta}}{\sin\theta + \sqrt{N^2 - \cos^2\theta}} \dots\dots\dots (1-7)$$

Where, θ is the glancing incident angle and $N=1-\delta+i\beta$ is the refractive index of the substrate medium and subscript s -polarization of the incident wave where the electric field vector remains perpendicular to the plane of incidence. The derivation relies on the boundary conditions as predicted from Maxwell’s equation.⁴³ The limitation of Fresnel’s formula for reflection lies in

that- it is applicable only for smooth surfaces where there is no role of surface or interface roughnesses. But in reality it is very difficult to obtain such smooth surfaces. The presence of surface roughness causes diffused scattering thus reducing the magnitude of the reflectivity. To take into account the presence of surface roughness in the film, Nevot-Croce model⁴⁴ is generally used.

Once the reflection co-efficient is known, reflectivity can be written as $R = |r_s|^2$. If we assume the case of normal incidence i.e. $\theta=90^\circ$, with incorporation of $N=1-\delta+i\beta$, we obtain $R \approx \frac{\delta^2+\beta^2}{4}$.

Both the values of δ & β are of the order of 10^{-2} - 10^{-6} , thus for a single interface the reflectivity at normal incidence is very small.

In order to obtain enhanced reflectivity performance near to normal incidence region multilayer structures are widely used. The multilayer structure consists of alternate high Z- low Z material and acts as a 1D-Bragg reflector.⁴⁵ However, reflection co-efficient of a multilayer configuration cannot be explained using Fresnel's formulae owing to the presence of multiple layers & interfaces.

To understand the reflection process in multiple layered films we begin with the consideration of a film of two different layers having different refractive indices deposited on a substrate as shown in Figure 1-1. As the incident photon impinges on the 1st layer of thickness d_1 & refractive index n_1 , a part of it gets reflected and the other part gets refracted to the 2nd layer of thickness d_2 & refractive index n_2 . On reaching the interface of 2nd layer/substrate, a part of the refracted beam gets reflected back and the other part gets transmitted to the substrate. Simultaneously, multiple reflections occur throughout the layers. The reflected beam appearing in the surface layer after travelling through the interfaces of different layers may interfere

constructively or destructively with the initial reflected beam. The interference of the reflected beams leads to the formation of Kiessig fringes as shown in Figure 1-1.

In case of multilayer structure, the reflection co-efficient is derived starting with the Fresnel's formula for single interface and finally incorporating the multiple reflections from different layers in a recursive manner. The final expression is known as Parratt's recursive formalism.⁴⁶

$$X_i = \exp(-2i\varphi_i) \frac{r_{i,i+1} + X_{i+1} \exp(\mp 2i\varphi_i)}{1 + r_{i,i+1} X_{i+1} \exp(\mp 2i\varphi_i)} \dots \quad (1-8)$$

Where, X_i is the ratio of the reflected to the transmitted beam of the i^{th} layer, $r_{i,i+1}$ is the Fresnel's reflection from the substrate/ layer interface. Another formalism known as 'matrix formalism' by Abeles⁴⁷ also produces similar results as that of Parratt recursive formalism.

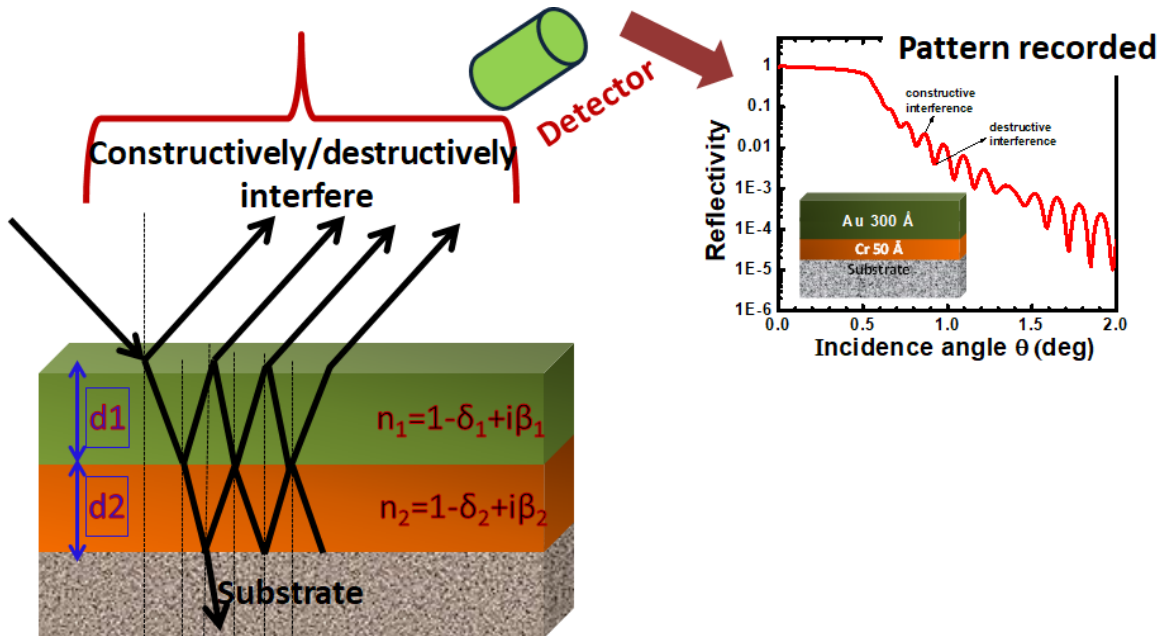


Figure 1-1 Schematic diagram showing interference of the reflected beam emerging from the top surface of a bilayer sample and the origin of the Kiessig fringes.

Finally we conclude that the prime criterion for a successful reflectivity measurement is a smooth and polished surface and a suitable film thickness since the thickness measurement depends on the angular resolution and the available q -range.

1.3.1.1 Methodology for extraction of optical constants from angle-dependent reflectivity data.

In this thesis the analysis of the experimental angle-dependent reflectivity data is carried out using a Labview based SRxrr tool as well as MOTOFIT⁴⁸ software. Using MOTOFIT software one can perform the least squares fitting of specular X-ray and neutron reflectivity data. The advanced feature of this software includes the inbuilt scattering length density database (SLD) which is user expandable too. The most unique feature of MOTOFIT is that it can simultaneously fit the multiple contrast neutron and reflectometry data. The user has choice of using four different algorithms for the refinement of the reflectivity data. There are various features like estimation of layer thickness using Fourier transform and from fringe spacing, it can fit as many layers as the user wants and finally all the graphs can be easily exported. The only limitation of this software is that all the analyses are valid for s-polarized X-rays. The SRxrr tool⁴⁹ has many unique features which are not available in other softwares. It considers the effect of higher harmonic, contribution of different polarization, effect of beam divergence, background noise etc. This tool is also capable of calculating both reflectivity and transmission as a function of incidence angle and wavelength/energy.

The most important step in extraction of optical constants from angle-dependent reflectivity data is the modelling of the different layers present in the film. In most cases, for a single layer thin film deposited on the substrate, a three layer model is used which consists of principal film layer, top surface layer which forms due to contamination or oxidation of the principal layer and a native oxide/interface layer over the substrate. Once the choice of layer model is complete the remaining task is to evaluate the different parameters associated with reflectivity data. The parameters include the optical constants (δ & β) of the individual layers & their structural parameters thickness & roughness.

Thus, for analysis in first step we start with the evaluation of the structural parameters of the different layers of the thin film. This is conveniently done by analyzing the hard X-ray reflectivity data where the number of variables is less. As for most of the elements the absorption edge lies in the soft X-ray region, so in the hard X-ray region beta (β) value does not varies much from the bulk form. Thus, as an initial guess, the thickness and roughness values of the layers & the optical constants corresponding to the bulk values are incorporated, with fixed beta (β) values.

Once the structural parameters of the film are obtained from hard X-ray reflectivity data, these are kept fixed while analyzing the soft X-ray reflectivity data. In this case the only variables remains are the optical constants, delta & beta.

The limitation of determining optical constants using this technique is that it provides optical constants for discrete photon energies. Thus to obtain fine features near the absorption edge region one has to perform a huge number of measurements in small steps of energy. Moreover, the modelling also becomes critical near the absorption edge region where due to high beta (β) value, the critical angle is not well visible or undefined and thus uncertainty in the determination of correct optical constants increases.

If a researcher is interested to understand the fine features near the absorption edges of the constituent elements, energy-dependent reflectivity measurements serve the purpose. However, for quantitative analysis of the optical properties i.e., extracting information about dispersion and absorption spectra from the photon energy v/s Reflectivity raw data is quite tricky. The following section deals with methodology involved in the extraction of optical constants from energy-dependent reflectivity spectra.

1.3.1.2 Methodology for extraction of optical constants from energy-dependent reflectivity spectrum

In experimental procedure the reflectivity is measured in terms of photon intensity which is nothing but a modulus square of reflection co-efficient. Therefore, in experimental procedure the phase information is lost and extraction of this information is a major challenge. This difficulty can be resolved using a special relation- Kramers-Kronig (KK) relation.^{50,51}

KK relations are bidirectional relations which connects the real and imaginary part of a causal, linear response function of any physical system.^{52,53} However, there are criteria for a response function to satisfy the KK relations. One of the most important criteria of the response function is that it must be causal and analytic.

We consider a physical quantity $X(t)$ at time t which depends on another quantity $Y(t')$ at times t'

by the relation: $X(t) = \int_{-\infty}^{+\infty} R(t - t')Y(t') dt' \dots\dots\dots (1-9)$

Where, R is the response function which describes that how some time dependent property $X(t)$ of a physical system responds to an impulse $Y(t')$ at time t' .

To satisfy the criteria for KK relations, the response function must be causal and on the other hand strict causality implies that the past can determine the present. Taking this into account: $R(t - t')=0$ for $t' \geq t$. In this way the causality condition gets satisfied.

KK relations can be applied to both absorption and reflection spectroscopy. In case of absorption spectroscopy, one can obtain the β spectrum experimentally and obtain the δ spectrum using KK relation. Whereas, in reflection spectroscopy, using KK relation one evaluate the phase (ϕ) of the electric field, and using reflectivity (R) and phase (ϕ) we can determine both δ & β simultaneously. There are several evidences in literature which shows the application of KK relation to the reflectance data for the reconstruction of phase.^{54,55,56,57} To obtain information

about two variables: dispersive part of refractive index δ as well as the imaginary part or absorption/ extinction co-efficient, there is requirement of information about both reflectivity and phase. But, unfortunately phase information is lost. Thus utilizing the KK relations to the reflectance data, one can easily determine the optical property of a material especially in the short wavelength region. This is very useful for researchers since in the short wavelength region other conventional methods like interferometry and ellipsometry fails because of experimental limitations.

KK relations in Reflectance Spectroscopy

The reflection co-efficient is a complex quantity which can be defined in terms of reflectivity (R) and phase (φ) of the reflected electric field as: $r(E) = \sqrt{R(E)}e^{i\varphi}$. In ample of literatures, the KK relation was implemented to the reflectance data for the formulation of phase at a particular energy say E_0 as-

$$\varphi(E_0) = -\frac{2E_0}{\pi} P \int_0^{+\infty} \frac{\ln R(E)}{E^2 - E_0^2} dE \dots \dots \dots (1-10)$$

This is well known as Robinson-Price formula⁵⁸ where P stands for the principal value of the integral.

Several problems were pointed out in the Robinson-Price formula. From the physics of the scattering theory as well as the theories of the dispersion relations⁵² it was clear that something was missing in the formula mentioned above. When this relation was used for two different energy values by Jones & March and their difference was taken, it obtained an ambiguous result. It was clearly evident that Equation 1-10 was incorrect by an additional term which is independent function of energy.

Nash et al.⁵⁷ claimed the correct version of the KK relation for the phase of the reflected electric field at energy E_0 as-

$$\varphi(E_0) = \varphi(0) - \frac{2E_0}{\pi} P \int_0^{+\infty} \frac{\ln R(E)}{E^2 - E_0^2} dE \dots \dots \dots (1-11)$$

This modification is inherent in the Robinson-Price formula itself, which may be corrected by performing the correct contour integration. Otherwise, according to Nash et al.⁵⁷, it is a term which arises from the existence of a pole at zero frequency/energy whose value is generally close to $-\pi$ for those materials whose absorption-coefficient tends to vanish at zero energy/frequency. There are several other possibilities of modification in the KK relation for phase, the most important one relating to the occurrence of singular points of complex reflection co-efficient along the imaginary energy axis. The correction terms corresponding to these singularities are known as Blaschke factors and to know the exact value of this factor the knowledge of the behavior of the complex refractive index along the imaginary energy axis is required.⁵⁹ There are several other factors on which these additive terms in the phase depend, such as the geometry of measurement i.e., normal or oblique incidence, polarization of the incident beam, samples under study: thin films, bulk or a multilayer.³⁹

In the shorter wavelength region (i.e. UV and X-ray region), the reflectance measurements are mostly carried out at oblique incidence because the critical angle in this region is of the order of few degrees only and below critical angle only the incident beam is totally reflected.

Thus, the choice of angle for the reflectance measurement is also an important parameter for reconstruction of phase from reflectivity. The choice must be such that the selected angle is below the critical angle for the particular energy range of measurement and most importantly it shouldn't be so small that footprint effect creeps into limelight.

The main concern that lies with the application of the KK relation of phase with reflectivity values at oblique incidence is the analyticity of the logarithmic kernel in the upper half plane at this condition. This has been emphasized well for the first time by Plaskett et al.⁵⁹ where they have explicitly shown the origin of the additional terms (Blashke factor, zero-energy pole term etc.) in the phase of KK relation and its relation to oblique incidence.

1.3.2 X-ray Absorption Spectroscopy

X-ray absorption spectroscopy (XAS) is one kind of inner-shell spectroscopy where X-ray photon interacts with an electron belonging to inner core-shell and the behavior of interaction is dependent upon the energy of the X-ray photon.^{60,61} As the incident photon energy approaches towards the energy of a core-shell, there is a sudden increase in the absorption cross-section, depicting the absorption edge. It is a powerful tool to probe the electronic structure. Moreover, the optical constants of material can also be determined using XAS data. However, depending on the mode of measurement the process of evaluation of optical constants is tricky one and will be discussed in the next section. In this section we will discuss about the basic mechanism of absorption process, the various modes of measurements and the factors influencing the experimental results.

Figure 1-2 shows all the basic mechanism involved in the X-ray absorption process. In this process, the sample undergoes photon absorption and finally leads to emission of a core level electron or photoelectron into unoccupied states near or above the Fermi level. As a photoelectron is ejected due to absorption, a vacancy is created in the core level.

This vacancy can be subsequently filled by an electron from upper level having lower binding energies. The difference between the two energy levels is released in the form of fluorescent photon. Another process i.e., Auger electron emission may occur which is nothing but radiation-

less transition. Further these electron emitted may lead to inelastic scattering among themselves resulting in the formation of a cascade of secondary electrons.

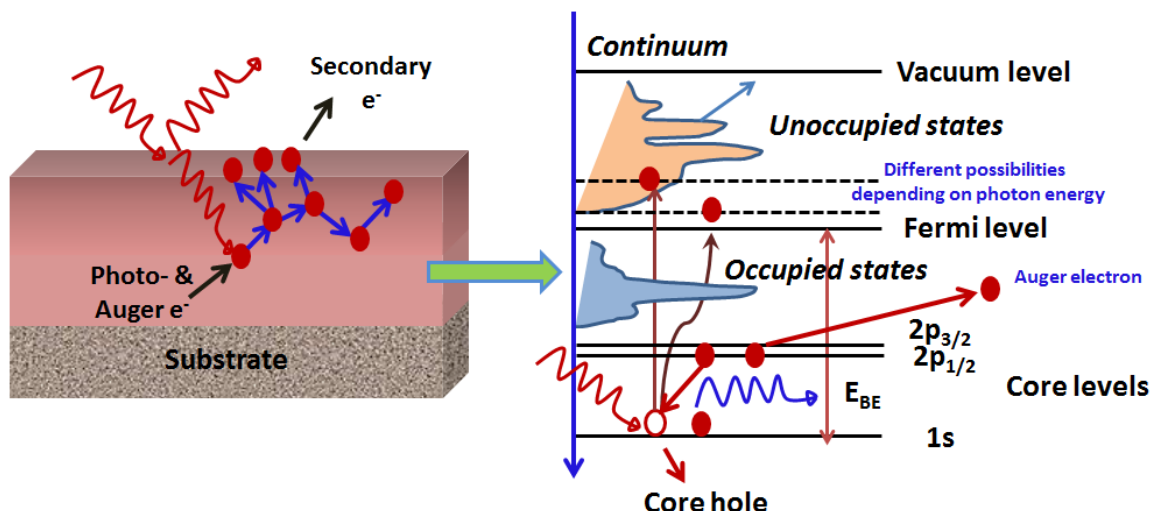


Figure 1-2 Schematic diagram showing the basic mechanism of the X-ray absorption spectroscopy and its utility in probing the unoccupied states and the electronic structure.

Depending on the products obtained in absorption process, XAS measurements can be performed in different modes: 1) Fluorescence Yield Mode (FY), where a photon emitted is collected. 2) Total electron Yield Mode, where the electrons emitted from the sample gets collected in the form of electrical current from the specimen. 3) Transmission mode where transmitted photon are collected and normalized with respect to the incident photons.

Figure 1-3 shows the schematic diagram of the different modes of XAS measurement. Transmission mode is the most simple and straightforward technique, however its limitation lies in the suitable sample preparation. The transmitted intensity can be written as- $I_t = I_0 e^{-\mu x}$, where I_0 is the intensity of the incident photons, x is the thickness of the sample and μ is the linear absorption co-efficient.² In soft X-ray region, since the absorption co-efficient is very high as compared to the hard X-ray region, there is requirement of preparation of free standing films, which is quite a difficult task.

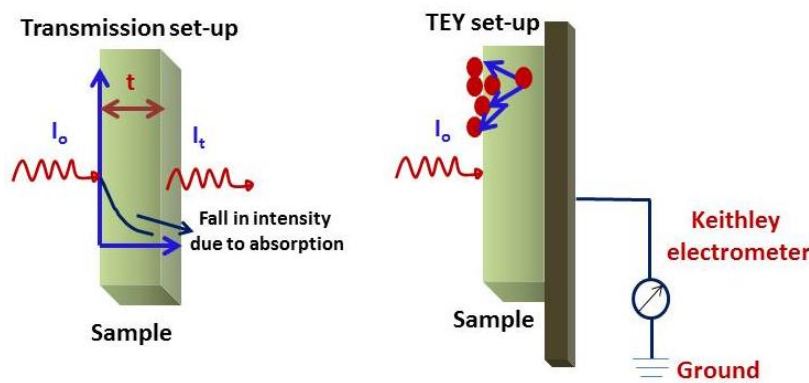


Figure 1-3 Schematic diagram showing different modes of X-ray absorption measurement.

To avoid this problem, the by-products such as the ejected electrons and the fluorescent photons can be recorded to obtain XAS spectra at different core-shells. The XAS mode where the ejected electrons (containing the primary, Auger & secondary electrons) are collected as the incident energy is scanned, is known as total electron yield (TEY) technique while if the fluorescent photons are collected, it is known as total fluorescence yield (TFY) technique. It is generally considered that both the TEY and TFY spectra is proportional to the absorption spectra^{62,63}, however, this statement is valid only under certain conditions.⁶⁴

In this thesis work, we have used the total electron yield mode for recording the X-ray absorption spectra. Thus the basic mechanism, influencing factors affecting the TEY spectrum and other details are described below.

When a X-ray photon of particular energy E and intensity I impinges on the sample surface, a portion of the radiation RI gets reflected and the remaining portion $(1-R)I$ gets refracted and penetrates inside the sample, where R is the reflectivity. The penetration depth of the refracted X-ray photon depends upon the angle of incidence θ and also on the refractive index N of the sample. In the next step, as the X-ray beam penetrates inside, absorption process becomes dominant.

In absorption process, depending on the incident photon energy, the ejection of electrons (either valence or core electrons) occurs which results in creation of a 'core-hole' in the inner shells. To obtain a stable electronic configuration, the core-hole is filled by an electron from upper states resulting in fluorescence/Auger processes.^{65,66,67,68} The generated photoelectrons and Auger electrons as a result of the absorption possess sufficient kinetic energy to travel towards the sample surface. However, it engages in the process of ionization with the atoms present in the sample at the expense of its kinetic energy. In the ionization process a cascade of secondary electrons are originated as a result of inelastic electron-electron collisions. The generated secondary electrons also possess sufficient kinetic energy to escape the barrier energy of the sample and get collected in the form of current (electron yield) signal. Thus the TEY signal mostly consists of the secondary electrons and also a part of high energy photoelectrons and Auger electrons whose mean free path is large enough to travel to the surface of the film.⁶⁹

An important point is to be noted that in most cases we consider the yield signal corresponding to the absorption process, however, the signal also depends on the nature of the absorption process or energy of the incident photon. In any of the absorption process, as an electron gets ejected a core hole is created in the inner shell, resulting in energy release through emission of Auger electrons. However, when the energy of the incident photon is more than the absorption edge energy, the ejected initial photoelectron possess a large kinetic energy and may contribute to the TEY signal along with the other by-products such as Auger and secondary electrons. On the other hand when the incident photon energy is equivalent to any absorption edge energy of the probing sample, the ejected photoelectron has approximately less kinetic energy and remains just above the Fermi level. At this point it is not capable of contributing to the TEY signal. However, the auger electron and the secondary electrons arising in such instance contribute to

the TEY signal. Thus, the contribution of the photoelectrons and also the Auger & secondary electrons (arising from these two cases) to the TEY signal is different.

The next important point is the influencing factors affecting the TEY signal which results in its disproportionality with the absorption spectrum.^{70,64}

1. The sampling depth of the TEY signal depends on the escape depth of the emitted electrons. As the X-ray penetration depth varies over an absorption edge, it might be possible that the electron escape depth tends to approach the X-ray penetration depth, leading to saturation effects and distorting the measured electron yield spectra.
2. At glancing angles, the reflection-refraction optical effect interferes with the yield signal resulting in its suppression.
3. Since TEY signal consists of photoelectrons, Auger electrons as well as secondary electrons whose energies are distributed over a broad range, it is not possible for a detector to detect all kind of electrons with equal efficiency.
4. The number of electrons recorded in a yield signal for different absorption process (mentioned above) differs resulting in distortion of TEY signal especially below the absorption edge.

1.3.2.1 Methodologies for extraction of optical constants from X-ray Absorption Spectroscopy

We have already discussed the various modes of XAS measurements in the previous section. In case of transmission measurements, both the transmitted intensity (I_t) and the incident intensity (I_o) of photons are recorded and thus absorption co-efficient (μ) can be determined from Beer-Lambert's law using: $\mu = -\frac{1}{x} \ln \left(\frac{I_t}{I_o} \right)$. Finally the optical constant β can be expressed as- $\beta =$

$\frac{\mu}{2k}$, where k is the propagation constant defined as $k = \frac{2\pi}{\lambda}$, with λ as the wavelength of the incident photon energy. However, XAS measurements in TEY/TFY and other modes do not record the absolute value of absorption co-efficient. In such case, the recorded spectrum have to be scaled with the standard Henke database over a large energy range away from both sides of the absorption edge region to get absolute β value.

Once we are able to extract the absorption spectra (β) over the complete energy range from transmission or other modes of absorption measurements, the dispersion spectra can be easily obtained using KK relation.-

$$\delta(E) = 1 + \frac{2}{\pi} P \int_{-\infty}^{+\infty} \frac{E' \beta(E')}{(E'^2 - E^2)} dE' \dots\dots\dots (1-12)$$

However, the problem arises on the available limited energy range of measurement. As an alternative to this finite energy range one has to opt for the extrapolations in both lower and higher energy spectra side of the measured spectra. The whole analysis process becomes complicated and sometimes errors are introduced in the δ spectra.

To simplify these problems one can use subtractive KK relations. The idea of subtractive KK relations, introduced by Bachrach & Brown⁷¹, is to reduce the error caused by the finite range of measurement. There is no stringent requirement of extrapolation over the long energy range while using the subtractive KK relations for determination of optical constants. First the idea of singly subtractive KK relation (SSKK) popped up, where the complex refractive index (both dispersion & absorption) at one reference point was measured using some independent technique. It is very suitable to use angle-dependent reflectivity technique for simultaneous determination of both dispersion and absorption part of complex refractive index at discrete photon energy and using the obtained data as the reference. Once the complex index of

refraction at one reference energy point is known, the accuracy of the KK analysis is greatly improved. Moreover it has the advantage of faster convergence than the conventional KK relation as discussed earlier.

Palmer et al.⁷² described the use of multiply subtracted KK relations (MSKK), which is an extension of SSKK. These relations are derived in a similar manner as singly subtractive KK relation; the only difference lies in the fact that it requires complete information on complex refractive index at several reference points. A special case of MSKK is the doubly subtracted KK relation, where E_a and E_b are the two reference points where delta values are known, and the final expression can be written as-

$$\begin{aligned} & \frac{\delta(E)}{(E^2 - E_a^2)(E^2 - E_b^2)} - \frac{\delta(E_a)}{(E^2 - E_a^2)(E_a^2 - E_b^2)} - \frac{\delta(E_b)}{(E_b^2 - E^2)(E_a^2 - E_b^2)} \\ &= -\frac{2}{\pi} \mathbf{P} \int_{E_{\min}}^{E_{\max}} \frac{E' \beta(E')}{(E'^2 - E^2)(E'^2 - E_a^2)(E'^2 - E_b^2)} dE' \dots\dots\dots (1-13) \end{aligned}$$

MSKK have much faster convergence as compared to SSKK & conventional KK, resulting in significant reduction in errors caused by extrapolations which is compulsory for data analysis using conventional KK.⁷³

To obtain the optical constants over measured energy range using MSKK, one needs to perform X-ray absorption measurements covering a large energy range away from the absorption edges in both low and high energy sides. In the next step the optical constant (β) can easily be obtained by scaling the measured spectra with the absorption (β) from the Henke tabulated database. Away from the absorption edges in both sides of edge region, the measured and tabulated spectra must match well, since the chemical environment of the bonding atoms does not affect the spectra much. The scaled absorption (β) along with the complex index of refraction measured at

discrete reference points using angle-dependent reflectivity are considered as inputs for DSKK and finally the dispersion spectra can be obtained over the finite energy range measured.⁷⁴

1.4 Methods to check the accuracy of the investigated optical constants.

Once we have determined the optical constants using the experimentally measured reflectivity or absorption spectrum, it is very important to know its accuracy and reliability. The reliability of the investigated optical constants using Kramers-Kronig relation depends on the integration limits i.e. the energy range of the reflectivity or absorption data used during phase or dispersion (δ) calculation. This can be well understood if we closely see the dispersion relation between phase and energy as given in Equation (1-10). In another form, this equation can also be expressed as-

$$\varphi(E_o) = \frac{1}{\pi} \int_0^{\infty} \ln \left| \frac{E+E_o}{E-E_o} \right| \frac{d \ln \sqrt{R(E)}}{dE} dE \dots\dots\dots (1-14)$$

According to Roessler⁵⁴, determination of correct optical constants depends on the evaluated phase which in turn depends on the slope of the reflection spectrum. When the reflection changes rapidly with the variation of energy, the term $\frac{d \ln \sqrt{R(E)}}{dE}$ becomes very large, thus it is necessary to choose an energy range where the slope of the reflection spectrum is high. In X-ray region, as we proceeds towards lower energy range, $R \rightarrow 1$, and the slope of reflection spectrum tends to zero and thus does not contribute to phase of the reflected electric field. Thus, the reliability of the optical constants is critically dependent on the choice of the higher energy range rather than that of the lower energy range.

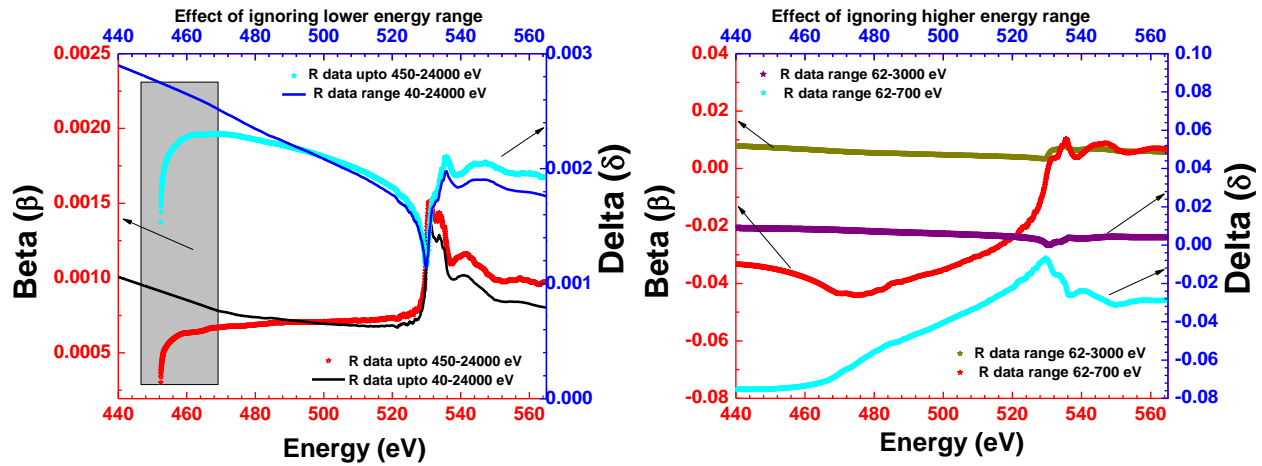


Figure 1-4 shows the effect of ignoring (a) lower energy range and (b) higher energy range of the reflection spectrum while calculating the optical constants.

Figure 1-4 shows the effect of ignoring the contribution of lower energy range and higher energy range of reflection spectra while calculating the optical constants using the phase spectrum as evaluated using Kramers-Kronig relation.

For these calculations we have considered the measured reflectivity spectrum of a ZrO_2 thin film at an incidence angle of 2° and stitched it with the simulated reflectivity spectrum calculated for different energy ranges. For simulation of the reflectivity spectrum outside the measured energy range, the structural parameters of the film were taken as obtained from GIXRR measurement of the film and the optical constants are taken from CXRO database⁷⁵.

It is evident from Figure 1-4 (a) that on ignoring the lower energy range truncation error creeps at the lower energy end of the optical constants (δ and β) spectra (~ 450 eV). On the other hand, the optical constants (δ and β) values near the measured O K-edge region does not get seriously affected. Figure 1-4 (b) clearly shows that the effect of ignoring the higher energy range is very critical on obtaining correct values of optical constants (δ and β). On choosing the reflectivity spectrum from the energy range of ~ 62 -700 eV, we obtain negative values of optical constants, which is completely wrong.

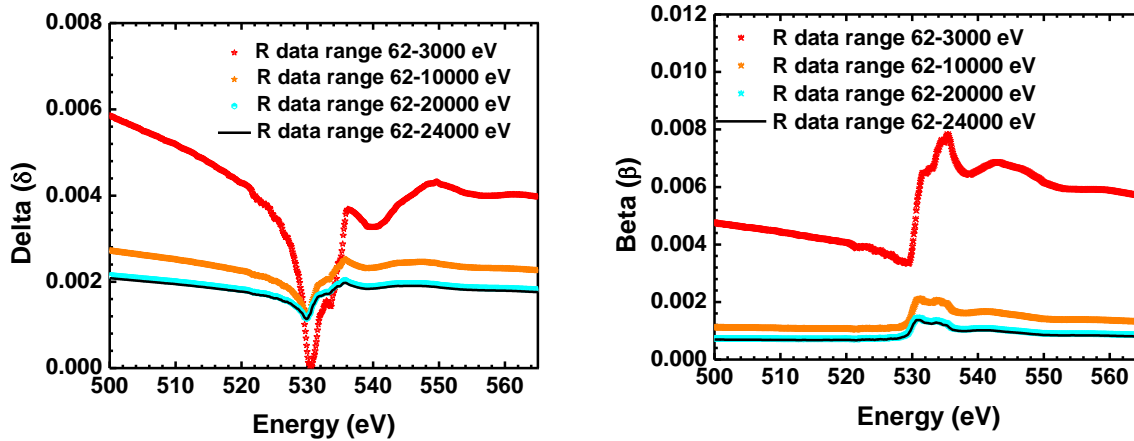


Figure 1-5 shows the effect of the choice of the higher energy range in the determination of optical constants (δ and β).

As we increase the choice of the upper limit of the energy range from 700 eV to 3000 eV, we obtain positive value of optical constants, though the values were still inconsistent. To obtain accurate and reliable values of optical constants we calculated the same using different limit of the higher energy values in increasing order. Figure 1-5 shows the effect of the increasing the upper limit of higher energy values for determination of optical constants (δ and β) spectra.

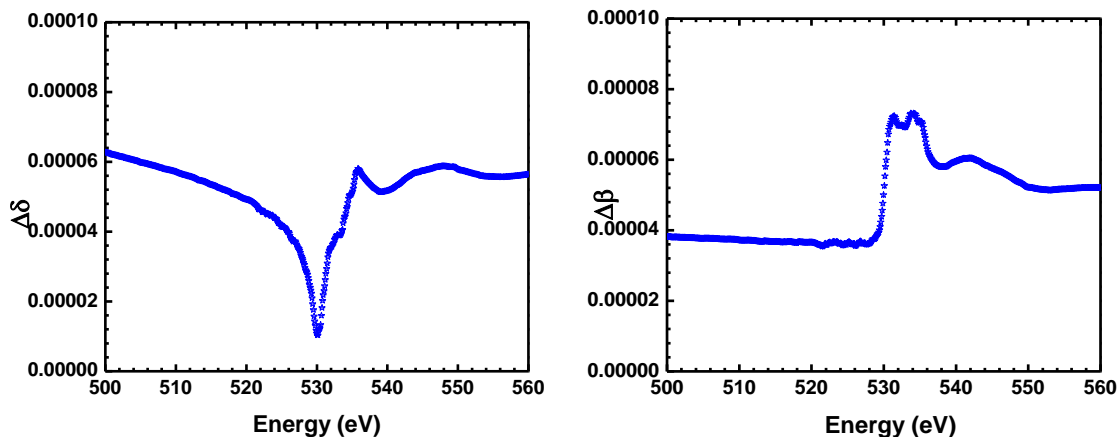


Figure 1-6 Difference in the optical constants (δ and β) values calculated using the reflectivity spectrum for two different energy ranges of 62-20,000 eV and 62-24,000 eV respectively. The upper limit of the higher energy values is different.

It is evident that as the limit of the higher energy range increases the optical constants values changes and finally we conclude that the optical constants values calculated using the reflectivity spectrum for the energy range of 62-20,000 eV and 62-24,000 eV are similar. Figure 1-6 shows

that the difference of both the optical constants (δ and β) lies in the fifth significant digit ensuring the accuracy of the obtained optical constants near the O K-edge region if we choose the upper limit of the higher energy to be greater than 20,000 eV.

Other factors like the number of data points used for the phase calculation, accuracy of the measured reflectivity data, uniformity of the film and most importantly roughness affects the accuracy of the determined optical constants using KK approach.

1.5 Oxides in X-ray optics

Rapid development of free electron lasers (FEL) ⁷⁶ and high brilliance synchrotron radiation sources have posed a new challenge for X-ray optics community. There is high risk of radiation damage in optical components due to X-ray pulses of very high intensity. ^{77,78} The increasing use of high brilliance sources for cutting edge research purposes poses a demand for high throughput optics. The optical elements must have the ability to withstand the heat load coming from the insertion devices in advanced synchrotron radiation sources.

The optical elements mostly used in the beamlines are thin film coated mirrors, multilayer mirrors, Fresnel's Zone plate, Laue lens etc. In case of thin film coated mirrors, high reflection occurs below the critical angle. Thus, mostly high-Z materials like Au, Pt, Ir etc. are used since $\theta_c \approx \lambda\sqrt{Z}$. In case of a multilayer mirror, alternate high Z and low Z materials are deposited in such a way that high reflection is obtained near the normal incidence. Different multilayer combinations like Mo/Si, W/B₄C, Mg/SiC, Mg/Co, Pt/C are widely used in the EUV/Soft X-ray region providing higher reflectivity. ^{79,80} However, problems like surface oxidation,

interdiffusion, interface formation, ageing with time & poor thermal stability always creeps in deteriorating the reflectivity performance.

New materials are required to withstand extreme radiation conditions and optimal performance. There is ultimate requirement of better understanding of their optical behavior. Researchers are working to find new materials combinations for better stability and high reflectivity performances.^{81,83} Oxide thin films have wide range of applications owing to their attractive mechanical, thermal, chemical and optical properties. Some of the oxide thin films are used in Fresnel's zone plate for soft X-ray microscopy application as well as in multilayer optics.

The present thesis work is devoted to the investigation of optical properties of three oxide thin films; aluminum oxide (Al_2O_3), magnesium oxide (MgO) & zirconium oxide (ZrO_2) in the Extreme ultraviolet (EUV)/ Soft X-ray region. The available literatures on X-ray optics focusing these three materials are discussed below.

Mayer et al.⁸⁴ developed a new technique of growing multilayer based zone plate for soft X-ray microscopy applications. They have chosen different combinations of oxides like Al_2O_3 - Ta_2O_5 & SiO_2 - Al_2O_3 and demonstrated from calculations that the efficiency of the zone plate is dependent on its thickness and obviously on the energy range. Finally using atomic layer deposition (ALD) technique, Al_2O_3 - Ta_2O_5 Fresnel's zone plate was grown whose diffraction efficiency was determined to be 1.4% for the present partial Fresnel's zone plate & 3.7% for the corresponding full Fresnel's zone plate. The numbers obtained are comparable with the theoretical efficiency for the full Fresnel's zone plate of 4.0% and are capable of resolving sub 39 nm structures at working energy of ~1200 eV. Sanli et al.⁸⁵ have demonstrated three-dimensional nanofabrication of multilayer zone plate with Al_2O_3 - HfO_2 material combinations. This combination provides higher diffraction efficiencies at both soft and hard X-ray region.

Experimentally they have achieved efficiencies of 80% with respect to the theoretical value and are capable of resolving sub-15 nm structures.

M. Reese et al.⁸⁶ have shown that the soft X-ray (28.8 Å, 430.56 eV) can be focused upto submicron level using multilayer Laue lenses. They have fabricated Laue lenses of ZrO₂/Ti multilayers using pulsed laser deposition (PLD) and focused ion beam (FIB) technique. T. Liese et al.⁸⁷ used ZrO₂/Ti multilayers for linear focusing optics (Fresnel zone plates). Moreover, ZrO₂ is considered as one of the most suitable capping layers for use in synchrotron based optical components.⁸⁸

Vitta et al.⁸⁹ have shown that multilayer material Ni₈₀Nb₂₀-MgO having periods in the range of 25–30.7 Å is suitable for the water-window region (23-44 Å, 280-530 eV). Fuhse et al.⁹⁰ have also demonstrated the high reflectivity performance of Metal/MgO based multilayers in the water window region. Magnesium based Mg/SiC is one of the potential multilayers providing best reflectivity performance in the 250–800 Å (30-49 eV) wavelength range (below Mg L-edge).⁹¹ However, due to instability of Mg, the experimentally obtained reflectance value is found to be degraded. MgO is found to be more stable as compared to Mg and can be chosen as the best alternative to Mg. There is also evidence of using MgO in conjunction with other oxide materials as capping layer over reflective multilayer structures.⁹²

All these applications of oxides in the EUV/Soft X-ray region motivate us to investigate its optical properties and understand its relation to other important physical properties like composition, electronic structure etc. In this thesis we have chosen three oxides: aluminum oxide (Al₂O₃), magnesium oxide (MgO) & zirconium oxide (ZrO₂) owing to their enriched applications in the field of X-ray optics. We have evaluated the optical constants of these three oxides covering the absorption edges of their constituent elements. We have also evaluated the

fine optical constants spectrum where several features appearing near the absorption edges are reflected in both δ & β spectra. Understanding the origin of these features reveals the electronic structure of the material and we are also able to correlate the electronic properties with that of optical properties. These fine features in δ & β spectra are missing in the Henke table and thus are a valuable finding.

1.6 Scope of the present work

The aim of the present thesis work is experimental investigation of optical constants of three oxide thin films; aluminum oxide (Al_2O_3), magnesium oxide (MgO) & zirconium oxide (ZrO_2) in the Extreme ultraviolet (EUV) and Soft X-ray region. All the applications of oxides as mentioned in Section 1.5 motivate us to investigate its optical constants.

The present work shows that the behavior of the optical constants is highly dependent on the film composition/stoichiometry, deposition technique and obviously the density. Thus, depending on our requirement of selecting an ideal spacer layer or absorber layer we can modify its optical properties by controlling its density using different deposition techniques.

The present work also aims to investigate the fine features of the dispersion (δ) & absorption (β) of these three important oxides near the absorption edges of their constituent elements. The investigation of fine features in the optical constants is important from fundamental point of view since these informations are not available in the literature. The huge deviation of the optical constants near the edge region with respect to the standard tabulated database is understood to be dependent on electronic structure & other structural characteristics.

Once the optical constants are estimated experimentally, its relation with various physical properties are understood, it will be much easier to simulate the optical performance of a device in this energy region.

Chapter 2.

Experimental Techniques

In this chapter, details of the Soft X-ray Reflectivity Beamline BL-03, including a brief introduction of Indus-2 synchrotron radiation source are discussed. A short description of the reflectivity beamline BL-04 of Indus-1 source is also presented. Details of the X-ray reflectometer chamber, which facilitates simultaneous measurements of specular X-ray reflectivity & grazing incidence total electron yield (TEY) used for the present thesis work are also discussed. Several other lab- & synchrotron based techniques used in the present thesis are given in details.

2.1 Introduction:

X-rays are the part of the electromagnetic spectrum, which is one of the most explored areas of research worldwide. With the advancement in technology one obtains high brilliance & focused X-ray beams which have variety of applications ranging from imaging soft matter & structural components of materials to killing cancer cells & providing spectroscopic information. X-rays can be broadly classified into two regimes- Hard X-rays & Soft X-rays depending upon their wavelength range. Hard X-rays can be used to probe materials at the atomic scales because of small wavelengths, whereas, the EUV and the Soft X-ray region of the electromagnetic spectrum are mainly used for different types of spectroscopic applications. The importance of soft X-rays lies in the fact that a large number of atomic resonances are present in this band of electromagnetic spectrum. Thus, the characteristics features of a particular element can be probed in the soft X-ray region. Moreover, soft X-ray microscopy is a powerful imaging technique and has a lot of applications in the field of biology⁹³, magnetic materials⁹⁴ and many more.

In the recent past, several advancements in soft X-ray and high vacuum components were made which enabled a rapid growth in the field of soft X-ray spectroscopy. With the emergence of high brilliance synchrotron sources where tunable monochromatic X-rays are available, the ease of investigating various materials properties is appreciated by materials science researchers. EUV and soft X-ray based spectroscopic techniques serve as a powerful non-destructive tool for probing structural parameters as well as optical properties of the materials. In this thesis we have investigated the soft X-ray optical properties of oxides and tried to understand the influence of electronic structure on optical properties using soft X-ray reflectivity (SXR) and other

complementary techniques. Most of the experiments are carried out at the beamlines of Indus Synchrotrons Radiation Source.⁹⁵

This chapter deals with the complete specifications of the two different soft X-ray reflectivity beamlines- a) BL-03 covering the energy range of 100-1500 eV on Indus-2 and b) BL-04 covering the energy range of 10-300 eV on Indus-1 synchrotron radiation sources. Brief descriptions of the two synchrotron sources are also given. This chapter also focuses on the sample deposition & other experimental techniques used in this thesis.

2.2 Indus Synchrotron Sources

2.2.1 Indus-1 source

Figure 2-1 shows the schematic layout of the Indus-1 Synchrotron source along with associated beamlines. It is a 450 MeV, 100 mA synchrotron source belonging to second generation. It produces continuous electromagnetic radiation in the soft X-rays to extreme ultraviolet region with a critical wavelength of 61 Å.

Table2-1: Parameters of Indus-1 synchrotron radiation source.

Electron energy	450 MeV
Beam Current	100 mA
Beam lifetime	7 hours
Bending magnet field	1.5 T
Critical wavelength	61 Å (~202 eV)
Circumference	18.97 m
Electron bunch length	11.3 cm
Photon flux @ λ_c	$\sim 7 \times 10^{11}$ photons/s/mrad horiz. 0.1% BW

The Indus-1 ring has a circumference of 18.97 m where four bending magnets and 16 quadrupole magnets are present. The magnets are arranged in four similar cells where each of the unit cell has a 1.3 m long straight section. In one of the section the septum magnet is present while a pulsed kicker magnet is placed diametrically opposite to it. The main function of the pulsed kicker magnet is to inject electron beam into the ring. In another straight section, a RF cavity operating at a frequency of 31.613 MHz is placed. Synchrotron radiation is extracted from 3 bending magnets placed inside vacuum chamber. Each of the bending magnet chamber has 2 ports, one at 10° and another is at 50° for extracting the emitted synchrotron radiation.^{96,97} There are 6 operational beamlines which are devoted to different applications. Parameters of Indus-1 synchrotron machine are given in Table 2-1 and further details about Indus-1 SR facility and related beamlines can be obtained online.

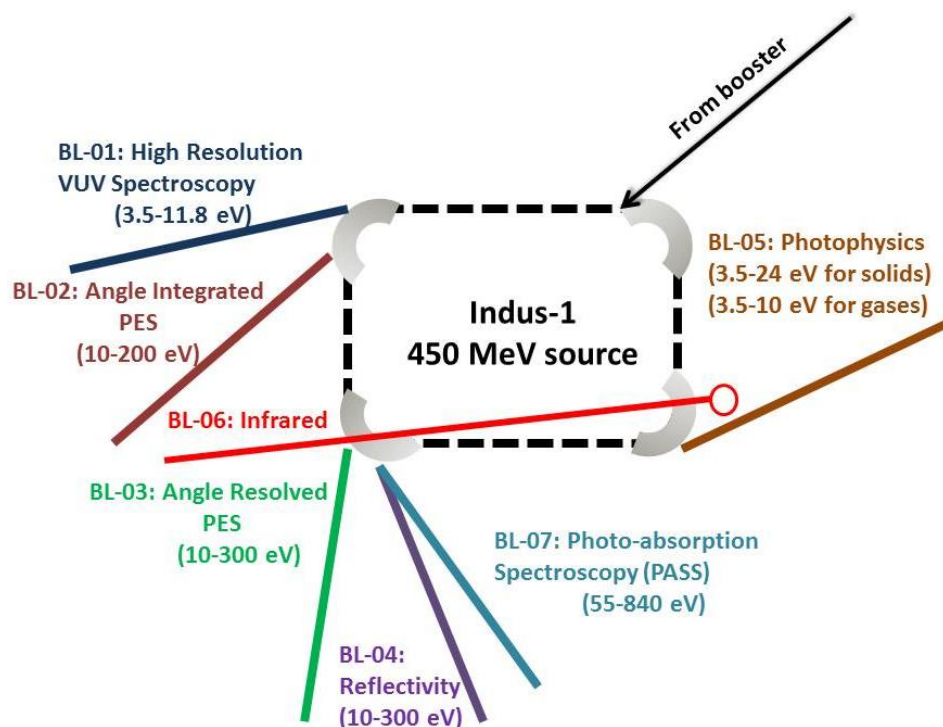


Figure 2-1 Schematic diagram of the various beamlines on Indus-1 synchrotron radiation source.

2.2.2 Indus-2 source

Figure 2-2 shows the schematic layout of Indus-2 synchrotron source along with associated beamlines. Indus-2 is a 2.5 GeV, 200 mA synchrotron source belonging to third generation. It produces continuous electromagnetic radiation in hard X-rays to soft X-rays with a critical wavelength of $\sim 1.98 \text{ \AA}$. The Indus 2 source consists of a double-bend-achromat lattice with zero dispersion function along the straight sections. This allows one to obtain a low-emittance and high-brightness photon source size for the bending magnets. The circumference of Indus-2 ring is about 172.47 m. The storage ring consists of 8 unit cells. The length of the straight section of each unit cell is 4.5 m and two 22.5° bending magnets are present. Besides this, several quadrupole and sextupole magnets are also present in the straight sections of each of the unit cell. A RF system is also present to compensate the energy lost by the electron beam. The system consists of four cavities which are powered by four stations excited by 64 kW RF power with operating frequency of 505.812 MHz.^{98,99} Table 2-2 provides the various parameters of Indus-2 storage ring. At present, there are 16 operational beamlines which are devoted to different applications including X-ray spectroscopy measurements. More details about Indus-2 SR facility and available experimental facilities at different beamlines can be obtained online.

Table 2-2: Parameters of Indus-2 synchrotron radiation source.

Electron energy	2.5 GeV
Beam Current	200 mA
Beam lifetime	24 hours
Bending magnet field	1.5 T
Critical wavelength	1.98 \AA (6.3KeV)
Circumference	172.47 m
Electron bunch length	3.00 cm
Photon flux @ λ_c	$\sim 10^{13}$ photons/s/mrad horiz. 0.1% BW

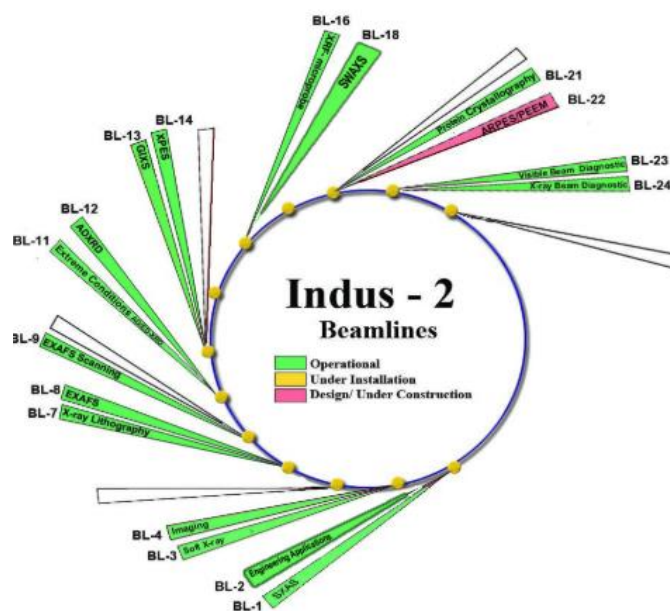


Figure 2-2 Schematic diagram of the various beamlines on Indus-2 synchrotron radiation source.

2.3 Soft X-ray Reflectivity Beamlines

Beamline serves as the interface between the synchrotron source i.e; the bending magnet or other insertion devices with the experimental station where the sample of interest is placed. Several components that lie within the path of beamline include the optical components like mirrors, monochromator(s), vacuum components, diagnostic devices and so on. The design of a beamline depends on the mechanism of various techniques and their requirements. For a soft X-ray beamline, even the experimental station requires a chamber having ultra-high vacuum; on the other hand there is no requirement of vacuum based experimental chamber in case of a hard X-ray beamline. Optimization of parameters like photon flux and monochromator resolution is an important factor and is completely based on the experiment. For example, in case of angle-dependent reflectivity measurements there is no stringent condition on high resolution but there is requirement of high flux otherwise the dynamic range of reflectivity reduces. On the other

hand, for energy-dependent reflectivity measurements especially near the absorption edges, where the energy separation between the salient features is less, there is a requirement of high resolution as well as high flux.

2.3.1 Reflectivity Beamline of Indus-1 source

The Reflectivity beamline¹⁰⁰ of Indus-1 provides monochromatic photons in the range of 40 Å to 1000 Å in terms of wavelength and 10 eV to 300 eV in terms of energy covering a portion of the soft X-ray region up to the extreme ultraviolet (EUV) region. This beamline covers the K-edges of low-Z elements like boron, carbon etc. to the L- edges of magnesium, aluminum, silicon etc. & M-edges of rare-earth transition elements like zirconium etc. All the parameters of Indus 1 reflectivity beamline are tabulated in Table 2-3. The beamline is installed on the bending magnet port of 50°, where the dimension of circulating electron beam in storage ring is 0.8 mm × 0.1 mm (horizontal × vertical). The acceptance angle of the beamline is 10 mrad × 5 mrad.

Table 2-3: Parameters of BL-04 of Indus-1 synchrotron radiation source.

Source	Bending magnet
Energy range	40-1000 Å (10-300 eV)
Flux	~10 ¹¹ photons/s/mrad horiz. 0.1% BW
Beam Size	~1mm×1mm
Energy Resolution	200-500
Monochromator	TGM (40-120 Å) 1800 l/mm (120-360 Å) 600 l/mm (360-1000 Å) 200 l/mm

This beamline uses toroidal grating monochromator to provide monochromatic photons in 40-1000 Å wavelength range (~300-10 eV energy range) with high flux and moderate spectral

resolution ($\lambda/\Delta\lambda \sim 200-500$). Three gold-coated gratings with different groove densities of 1800, 600 and 200 lines/mm respectively are installed in the monochromator section to get monochromatic photon with high flux in three different wavelength range of 40-120 Å, 120-360 Å and 360-1000 Å respectively.¹⁰¹ Different edge filters like boron, aluminum, silicon and indium are present in the beamline to suppress the higher harmonic contribution.¹⁰² Moreover, a two-mirror system is also provided in the beamline to reduce higher harmonic contamination dominant in the grating-2 (120-360 Å) & grating-3 (360-1000 Å) region¹⁰³ whose details are given below.

2.3.1.1 Two-mirror harmonic suppressor system

The two mirror harmonic suppressor system consists of two polished Si mirrors placed parallel to each other in such a way that the beam incident on one mirror gets reflected when the incidence angle is equal to the critical angle and the reflected beam from mirror 1 serves as an incident beam for mirror 2 and the final reflected beam from mirror 2 consists of photons free from undesired higher harmonics.

Figure 2-4 shows the reflectivity spectra of aluminum oxide single crystal measured at an angle of 5 degree. The measurements are carried out at the grating 2 (120-360 Å) and 3 (360-1000 Å) of BL-04 of Indus 1 synchrotron source with and without Higher order suppressor (HOS) system. The reflectivity in the grating 3 region remains almost constant to the value of 85% with no features using the two mirror HOS. On the other hand, without the presence of the two mirror suppressor system the reflectivity diminishes up to 20% in the grating-3 and several unwanted features are observed. The results obtained using BL-04 are compared with same measurements performed at the metrology beamline of Synchrotron SOLEIL; both of the results matches well.

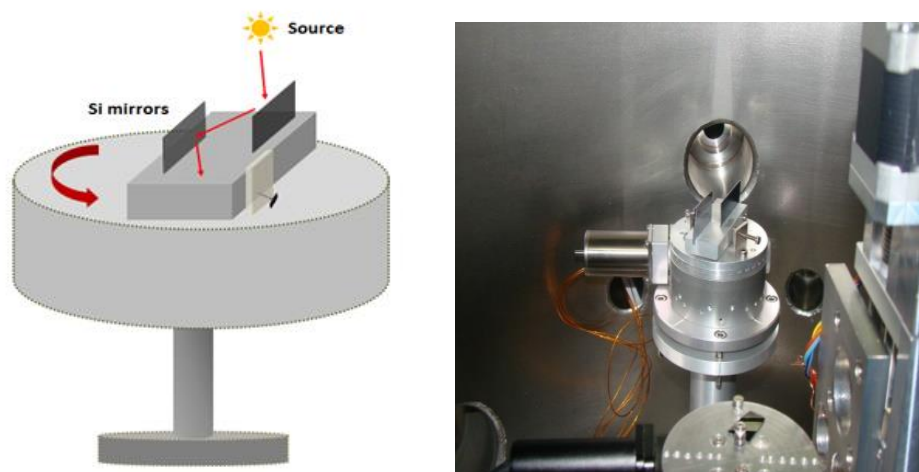


Figure 2-3 Schematic and actual photograph of two mirror higher order suppressor system installed at the reflectivity beamline (BL-04) of Indus-1 Synchrotron radiation source primarily used for grating 2 & 3 in the wavelength range of 120 Å-1000 Å

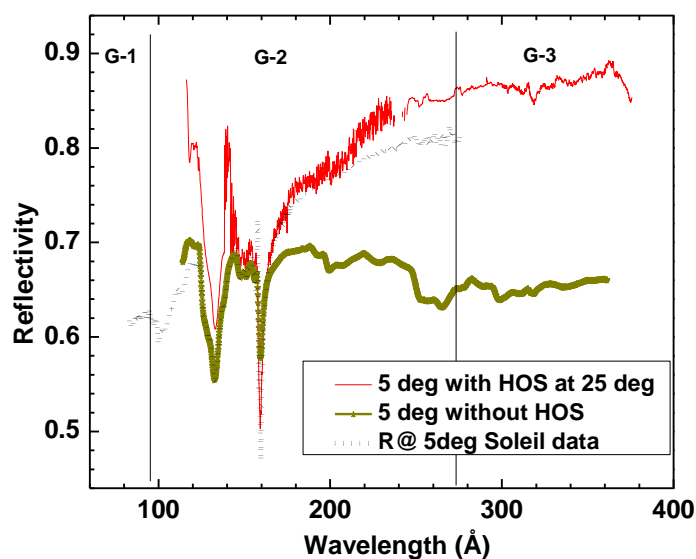


Figure 2-4 Comparison of the reflectivity spectra over the complete range of grating 2 & 3 of BL-04 Indus 1 with and without two mirror harmonic suppressor system. Results of similar measurement carried out at metrology beamline of Synchrotron SOLEIL are also shown.

2.3.1.2 Details of the reflectometer chamber

Reflectometer chamber¹⁰⁴ is the experimental station where the samples are placed and maintained at a high vacuum of 2×10^{-7} mbar, which is comparatively much less than the rest of the beamline. A differential pumping system is accommodated in between the reflectometer

chamber and the beamline section in order to separate the high vacuum reflectometer chamber ($\sim 2 \times 10^{-7}$ mbar) from the ultra-high vacuum section of the beamline ($\sim 5 \times 10^{-8}$ mbar). A θ -2 θ goniometer and a linear translation stage are used for performing various scans and sample alignment purposes. The goniometer can be set in both vertical and horizontal reflection geometry but it is not motorized. In vertical reflection geometry, the incident synchrotron light is plane polarized in horizontal plane and hence this measurement geometry is called s-polarization geometry. On the other hand, for the horizontal geometry the synchrotron light is plane polarized in vertical plane and thus it is called p-polarization geometry. In this thesis work, the s-polarization geometry is chosen for all measurements.

Before the onset of reflectivity measurements, various scans are performed to align the sample in the path of the beam to obtain specular reflection condition. In the first stage, the detector is aligned with respect to the direct beam by placing the sample stage out of the beam path. In the next stage, the sample stage is placed in the path of the beam at the position where the detector current reads just the half of the direct beam. Once the sample stage is placed in the beam path, in the next step rocking scan is performed to align the sample with respect to the beam. A soft X-ray silicon photodiode detector (International Radiation Detector Inc, USA) having a 100 % internal quantum efficiency is used for the detection of the reflected photon.¹⁰⁵ The detector signal is measured in terms of electrical current using a Keithley electrometer (6514).

2.3.2 Reflectivity Beamline of Indus-2 source

The soft X-ray reflectivity beamline of Indus-2 is a bending magnet based beamline covering photons from the energy range of 100 to 1500 eV and 8 to 124 Å in terms of wavelength. This beamline covers the K edges of light elements like C, N and O and the L and M edges of

transition elements. The major parameters of the beamline optical elements are given in Table 2-4¹⁰⁶.

Table 2-4: Parameters of BL03 beamline optical elements						
Optical Element	TM ₁	SM	TM ₂	G ₁	G ₂	G ₃
Deflection	Horizontal	Vertical	Horizontal	Vertical	Vertical	Vertical
Size (mm ²)	900×50	300×20	270×25	180×20	180×20	180×20
Coating	Au	Au	Au	Au	Au	Au
Meridional Radius (mm)	413088	152745	85961	--	--	--
Sagittal Radius (mm)	280	152745	105	--	--	--
mer. slope error (arc sec)	1.0	0.1	1.0	0.16	0.16	0.16
sag. slope error (arc sec)	3.0	0.2	3.0	0.2	0.2	0.2
Included angle (deg)	176	177	176	174.5	174.5	174.5
Groove density (l/mm)	--	--	--	1200	400	150
Energy range (eV)	--	--	--	400-1500	150-600	100-225
Line space variation parameters for G1, G2, G3				a1(mm ⁻¹)	-5.546 × 10 ⁻⁴	
				a2(mm ⁻²)	2.304 × 10 ⁻⁷	
				a3(mm ⁻³)	-6.3 × 10 ⁻¹¹	
Beamline major parameters						
Energy Resolution				1000-6000		
Flux				10 ⁹ - 10 ¹¹ ph/sec		
Beam size				0.5 mm(H) × 0.3 mm (V)		
(in experimental station)						

2.3.2.1 Optical Scheme of the beamline:

The Indus-2 Soft X-ray reflectivity beamline uses a constant deviation angle variable line spacing plane grating monochromator (VLS-PGM) with Hettrick type^{107,108,109} optics. The choice of this configuration lies in its simplicity of mechanism and requirement of less number of optical elements.¹¹⁰ The optical layout of the beamline is shown in the Figure 2-5. The optical components of the beamline consist of the pre-focusing toroidal mirror, a spherical mirror, three interchangeable gratings and finally a post-focusing toroidal mirror.

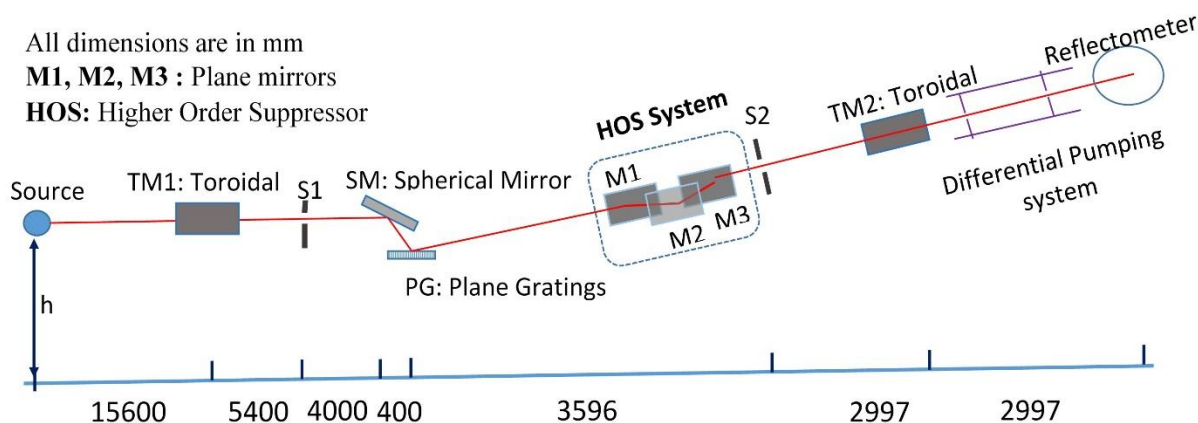


Figure 2-5 Optical schematic of the soft X-ray reflectivity beamline BL-03 of Indus-2 Synchrotron source.

The first optical element of the beamline is a horizontally deflecting and vertically mounted toroidal mirror named as TM1. TM1 accepts 2 mrad (H) \times 3 mrad (V) of the emitted bending magnet radiation and focuses the light vertically on to the entrance slit S1, and horizontally on to the exit slit S2. The second optical element present is a spherical mirror SM, which is vertically deflecting and forms a convergent beam on the grating present. After SM, the white light is diffracted by the plane grating and desired wavelength gets focused on the slit S2. Three gratings named as G1, G2 and G3 of line densities 1200, 400 and 150 lines/mm respectively are present. These gratings are interchangeable in-situ without breaking the vacuum and are used to cover the whole energy region of 100-1500 eV efficiently. The beamline provides moderate spectral resolution ($E/\Delta E \sim 1000-6000$) and high photon flux ($\sim 10^9 - 10^{11}$ ph/sec) with the use of three gratings. The monochromatized light with a particular wavelength gets focused on to the sample by horizontally deflecting and vertically mounted toroidal mirror TM2. The whole beamline operates in ultrahigh vacuum environment of pressure $< 3 \times 10^{-9}$ mbar. All the parameters of beamline optical elements are given in Table 2-4.

2.3.2.2 Details of the Reflectometer chamber

The experimental station of the Soft X-ray reflectivity beamline BL-03 consists of a reflectometer chamber, where the sample to be studied is placed in a high-vacuum environment similar to that of BL-04 of Indus 1 as described in section 2.3.1.2. A diverse range of experiments can be performed in the reflectometer chamber, which includes angle- & energy-dependent soft X-ray reflectivity studies of thin films & multilayers, metrology experiments of real optical elements, total electron yield measurements of bulk as well as thin film samples, investigation of efficiency of gratings etc.

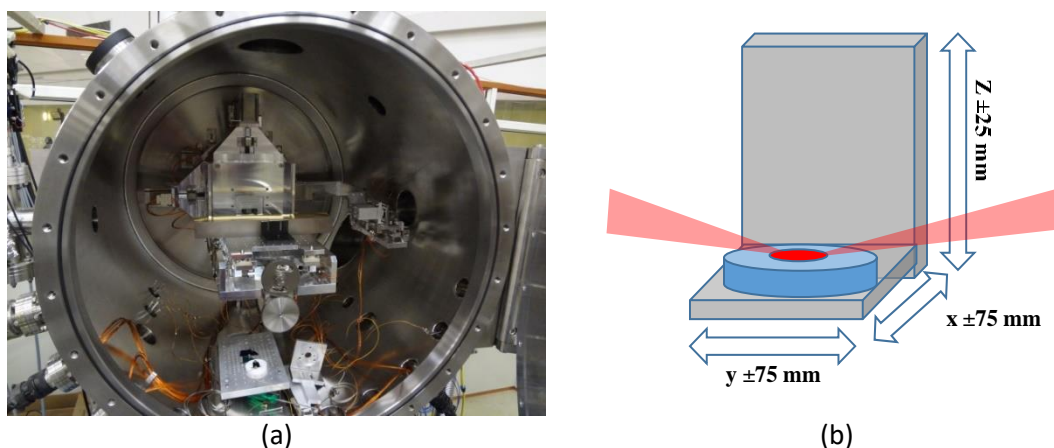


Figure 2-6. (a) Inside view of the reflectometer chamber (b) schematic of sample scanning stages as the sample can be scanned in x-y plane using two lateral translation stages and Z-vertical stage can be used to move the sample in and out of the beam and also to adjust samples of different thicknesses.

The reflectometer chamber consists of a 2-axes high-vacuum compatible goniometer with X-Y-Z sample manipulation stages as shown in Figure 2-6 (a). The scattering geometry is in the vertical plane which is suitable for the s-polarized reflectivity measurements. Figure 2-6 (b) shows the schematic diagram of the sample stage present in the reflectometer chamber. The sample and the detector are mounted on the θ and 2θ axes respectively. For moving the sample in and out of the beam, a high vacuum compatible linear translation stage is mounted on the sample rotation stage. The sample holder is capable of accommodating a sample of size up to 300 mm length, 100 mm

width and 50 mm height. It is also capable of holding a sample upto a weight of about 5 kg, enabling metrology of real optical components in terms of reflectivity performance. The reflectometer has a capability of positioning the sample with precision of 2 microns and the angular position of the sample can be set within 0.001° . A glass window gate valve separates the experimental station from the beamline. This helps in using the visible part of the synchrotron radiation from the window of the gate valve to position and align the sample keeping the reflectometer at the atmospheric pressure. Incident beam intensity can be monitored continuously by inserting a Nickel wire mesh in the incident beam and monitoring the photoelectron current from this mesh.

A soft X-ray photodiode detector (similar to that of Indus-1 beamline) is placed at a distance of 200 mm from the axis of rotation. The detector is placed at the detector arm which is designed to mount multi detectors. Using these detectors, reflectance can be measured over five orders of dynamic ranges. The used silicon photodiode detector (from International Radiation Detector Inc., USA) has 100 % internal quantum efficiency. Besides this photodiodes with Al or TiC coatings are also present. The detector signal is measured in terms of electrical current using a Keithley electrometer (6514). The total electron yield (TEY) signal can be directly measured by connecting a wire on a sample surface since the sample stage is electrically isolated from the goniometer body.

2.3.2.3 Investigation of Higher harmonics in BL-03

Harmonics are an intrinsic part of a beamline. In case of a soft X-ray beamline, grating monochromator is an essential optical component, however it has the problem of higher order harmonics in the monochromatic light it chooses.

In various experiments the data generated by the incoming energy of photon E and those by the higher harmonics (i.e. $2E$, $3E$ and so on) cannot be separated and therefore the analysis of measured data becomes a complicated process. In general, transmission or reflection-based gratings are used as an analyzer to experimentally quantify the spectral purity. The first order diffraction peak of incident energy range E coincides with higher order diffraction peaks of $2E$, $3E$, etc. Therefore the relative measurement with respect to the first order peak does not give correct information.

There is an alternative solution to estimate the higher harmonic contribution in the soft X-ray region. The solution is based on the angle-dependent reflectivity measurement of the multilayer mirror. The quantitative analysis of multilayer reflectivity data is rather simple; therefore the measured data can be fitted to retrieve the information of harmonic contamination. To investigate the different harmonic contribution of BL-03 in energy range of 400-1600 eV (grating 3), we have used a W/B₄C multilayer of $d=37$ Å to analyze higher harmonics in the 400-1600 eV energy range.

The initial characterization of the multilayer was carried out by Grazing Incidence X-ray reflectivity (GIXRR) technique using Cu K $_{\alpha}$ source (1.54 Å). The obtained data was analyzed using the Parratt Recursive formalism⁴⁶ and the effect of surface roughness was taken into account using the Nevot-Croce model⁴⁴ where the interface is considered to be of the form of an error function. The information about the structural parameters of the multilayer are given in Table 2-5. In the next step, we have measured the angle-dependent reflectivity data at different photon energies in the energy range of 400-1200 eV with the aim to investigate the harmonic contribution.

Table 2-5 Structural parameter of the W/B₄C multilayer used for investigation of harmonic content

Layer	Thickness (Å)	Roughness (Å)
Top surface	18±1.5	2.0
B ₄ C	20.6±2.0	2.0
W	16±2.0	5.1
Si Substrate	--	3.3

The measured data are analyzed using the Parratt formalism, keeping the structural parameters fixed and varying the other parameters like optical constants (δ & β) for two different energies corresponding to the fundamental energy (E) selected for the measurement and its harmonic (2E) along with their individual contributions.

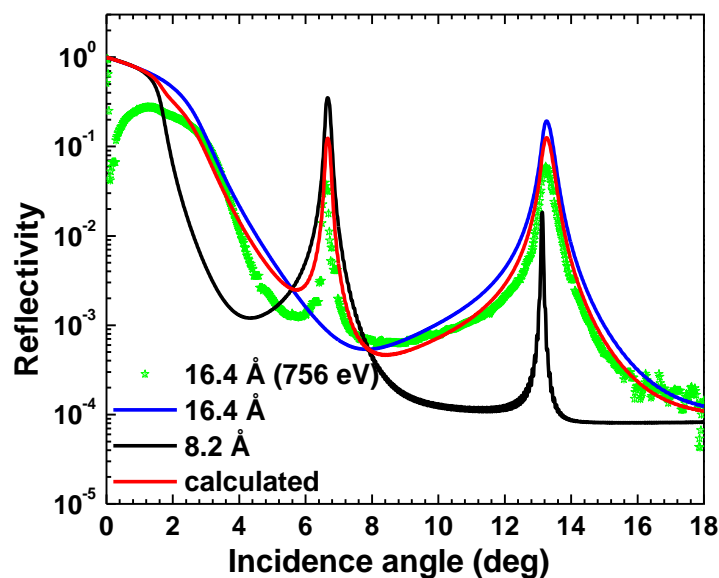


Figure 2-7 Measured (green stars) and calculated (red solid line) reflectivity pattern considering the contribution of harmonics present in the beamline.

In case of the reflectivity data measured at a wavelength of 16.4 Å, an appearance of a Bragg peak at $\theta=6.5^\circ$ is observed, which is not expected. However, a simulation of the reflectivity data, with same structural parameters, for the wavelength of 8.2 Å shows the appearance of Bragg peak at 6.5° . This fact ensures the presence of harmonic contribution in the reflectivity data of

the fundamental wavelength $\lambda=16.4 \text{ \AA}$. Moreover, appearance of a critical angle at $\theta=1.7^\circ$ corresponding to the higher harmonic ($\lambda\sim 8.2 \text{ \AA}$) is evident.

2.3.2.4 Higher order suppressor system in BL-03:

There are several solutions to improve the spectral purity of the monochromatic light of a beamline-

- 1) Transmission filters.
- 2) Two, three & four mirror system.

With the aim to improve the spectral purity of the monochromatic light coming from the monochromator, a three mirror based higher order suppressor (HOS) is designed. This HOS system will be installed before the exit slit of the monochromator of the Indus-2 reflectivity beamline. The schematic of the HOS optical elements is shown in Figure 2-8.

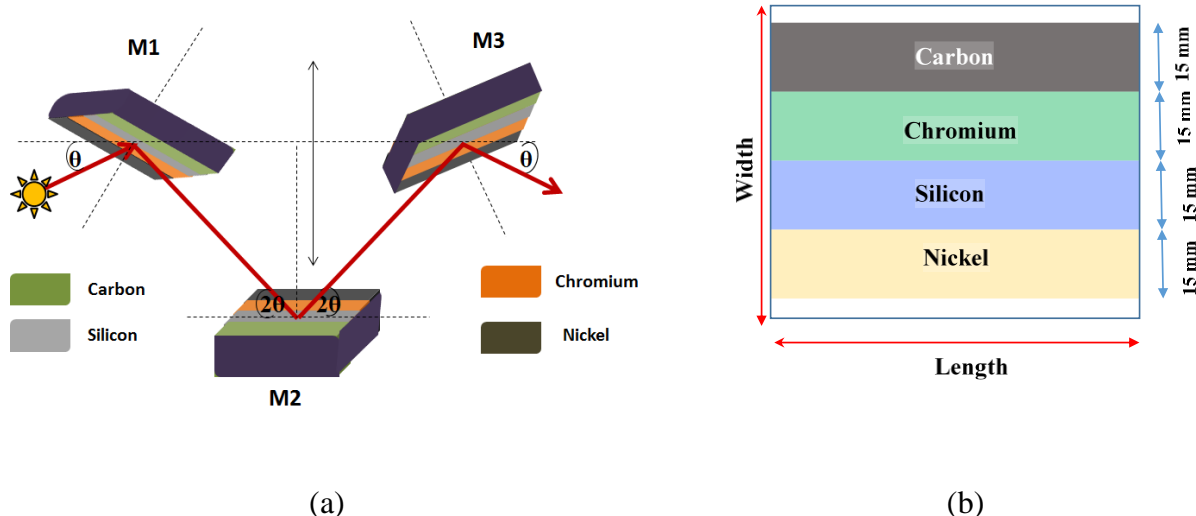


Figure 2-8. (a) Schematic of three mirror assembly for higher order suppressor (top view). Each mirrors are coated with stripes of four different materials as shown in (b). During the operation the three mirrors will set such that the stripes of same materials will remain in the beam path.

It is clear from the figure that the mirrors M1 and M3 operate at a grazing angle $\theta/2$, whereas, mirror M2 is set at an angle θ and moved in transverse direction. The configuration of M2 is set in such a way that the beam exit will remain fixed during the angular movement of the mirrors M1 and M3.

In order to suppress the higher harmonics efficiently in the energy range of 100-800 eV, different coating materials suitable to different energy regimes are used. The three mirrors in the HOS system will have a stripe coating of four different materials - Carbon, Chromium, Silicon and Nickel. During the operation of the HOS, the three mirrors can be set in the beam path with similar coatings on respective mirrors. The HOS setup will improve the spectral purity and reduce the harmonic components below 0.1%.

2.4 Deposition Techniques

In the present thesis work, three types of oxide thin films are prepared using different Physical Vapor Deposition (PVD) based techniques. The PVD technique is based on vaporization or atomization of the target sample inside a vacuum chamber, which condensate on a substrate, thus forming a film. We have used reactive & ion- beam sputtering technique for the deposition of aluminum oxide and magnesium oxide thin films, while the zirconium oxide films were prepared using electron beam evaporation technique. In this section we will give a brief introduction of the mechanism of sputtering and evaporation based process and then the details of the individual deposition techniques.

2.4.1 Mechanism of Sputtering

Sputtering is the process of removal of atoms from the surface of a thin film or coating material as a consequence of transfer of momentum by bombarding neutral atom/ion to the film surface.

The different processes occurring during a sputtering process is depicted in Figure 2-9. Mostly energetic gas ions are used for the bombardment process. In most of the cases, the gas ions are accelerated by implementation of a high voltage. As a result of acceleration, the gas ions gain energy and hit the target/ cathode material. The whole process is maintained at a high vacuum environment. The atoms ejected from the target material as a consequence of momentum transfer are deposited on the substrate placed inside the chamber forming a thin film.

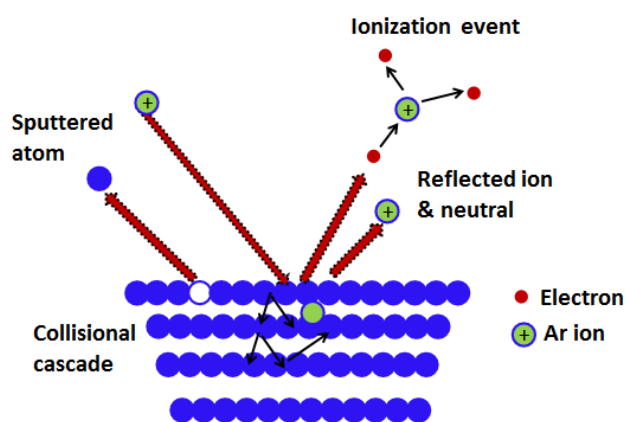


Figure 2-9 Schematic diagram of different processes which occurs during sputtering.

When the gas ions interact with the surface of the target, phenomena like reflection, adsorption, sputtering, ion implantation, chemical reaction etc. can take place. These phenomena depend on the kinetic energy of the bombarding particles, for e.g. at very low energy (~ 5 eV) the bombarding particles bounce back/reflect without affecting the target. Whereas at much higher energy (>10 keV) the process of ion implantation predominates over the sputtering process. Thus, one must choose the energy of the gas ions carefully to lie in between these two extremes (~ 10 eV to 3 keV) to carry out sputtering smoothly.

Another important point is the bombardment direction of the gas ions. In case of normal incidence, the number of atoms ejected from a surface is comparatively less since only the secondary collision participates in atom ejection. Whereas at oblique incidence the sputter yield from the primary collision process is significant.

Despite of choice of correct energy, some unavoidable consequences always exist in the sputtering process. For example, it may happen that some fraction of the energy of the bombarding ions may contribute to the lattice damage.

2.4.1.1 Reactive Sputtering Technique

In this technique a compound thin film is deposited by sputtering a target which may be a compound or pure element in presence of a reactive gas (mostly oxygen, nitrogen etc.) or a mixture of gases. Along with the reactive gas, an inert gas (mostly Ar, Xe, Kr etc.) creates a plasma discharge through ionization. Simultaneously, as the reactive gas enters into the deposition chamber, it collides with the energetic particles present in the plasma created and dissociates into neutral as well as charged components. These components react with the sputtering target resulting in the film deposition on the substrate. Figure 2-10 shows the different processes occurring during reactive sputtering as discussed above.

The prime advantage of this technique is that one can easily control the film composition by controlling the flow of the reactive gas. However, there are certain disadvantages too. In case of an elemental target, the process of target poisoning is a severe issue and the difficulty increases with the higher value of the partial pressure of the reactive gas.

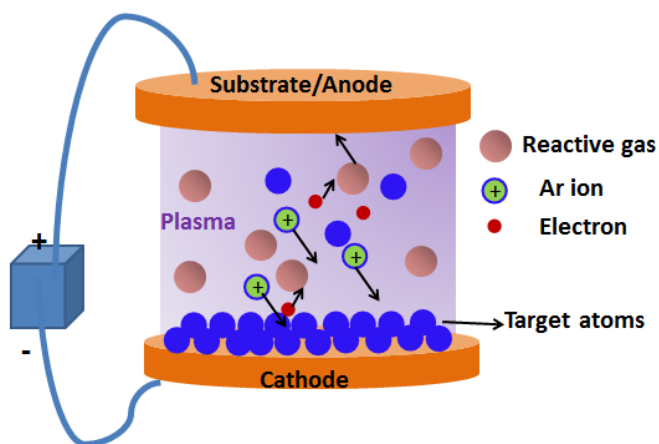


Figure 2-10 Schematic diagram of reactive sputtering technique.

2.4.1.2 Ion Beam Sputtering Technique

In this technique an ion source is used to generate energetic ion beam, which bombards on the target material to be sputtered. The ion source consists of both cathode and anode which are aligned to each other. On applying a high voltage field of 2-10 kV an electrostatic field is created inside the ion source as a result of which the injected argon gas ionizes, creating plasma inside the source region. The ions are then accelerated from the anode region to the cathode resulting in the formation of a focused ion beam. The focused ion beam hits the target material and sputters the target material towards the substrate via the sputtering mechanism as shown in Figure 2-11.

In this technique there is no use of external reactive gas, thus control of film composition completely relies on the target material. However, to have better stoichiometry and density of the films, one can use two ion beam configuration system. Other options include the presence of additional flowing gases like oxygen, nitrogen etc. for the growth of oxides & nitrides thin films.

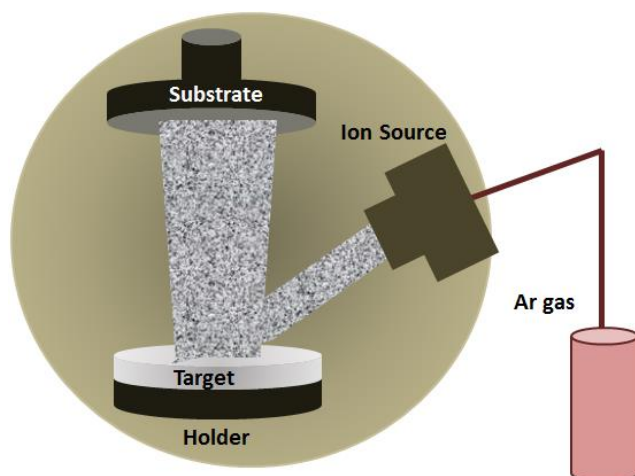


Figure 2-11 Schematic diagram of ion beam sputtering technique in a single ion beam configuration.

One of the most important advantages of this technique is good quality film, which is firmly bonded to the substrate. This is due to the fact that because of high energy of the ion beam, there is still sufficient kinetic energy to migrate on the surface of the substrate. Other advantages include high precision of thickness and preferable density and adhesion to the substrate. However, the disadvantage includes low deposition rate and incapability of depositing uniform films over larger areas.

2.4.2 Mechanism of Evaporation Based Processes

Evaporation is the process where the target material used for deposition is vaporized by various means of heating which include resistance heating, heating by electron gun etc. The evaporated atoms/molecules traverse towards the substrate with minimum collisions and get settled on the substrate forming a thin film. The complete process takes place in vacuum condition ($\sim 10^{-5}$ - 10^{-9} mbar) to minimize collision with the residual gases and have suitable mean free path.

For evaporation based deposition process the melting temperature of the holder having the target material to be deposited should be reasonably higher than the boiling point of the material. Other important criterion includes: temperature of the substrate must be less than the melting

point of target material and the substrate to target separation should be less than the mean free path of the material atoms or molecules.

2.4.2.1 Electron Beam Evaporation Technique

In this technique the target material is bombarded by high energy electron beam leading to evaporation. The electron beam is originated from thermionic emission of electrons generated by heating the filament (tungsten material). The emitted electrons are accelerated by a high voltage potential and a magnetic field is often applied to bend the electron path so that it gets focused on the target along the line of sight. The focused electron beam along the line of sight initiates the process of localized heating and leads to high evaporation rate. Thus, by changing the magnetic field one can easily control the curvature of the electron path and control the evaporation rate by changing the line of sight. Figure 2-12 shows the different processes occurring during film deposition by electron beam evaporation technique as discussed above

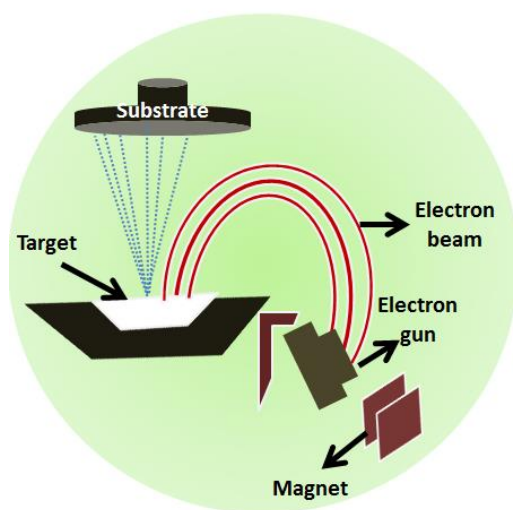


Figure 2-12 Schematic diagram of the electron beam evaporation technique

The most important advantage of this technique is that it can yield higher deposition rates starting from 0.1 nm/min to 100 nm/min. The disadvantage of this technique includes the

control of electron beam power in order to maintain the required speed of evaporation. Mostly the electron beam power fluctuates and results in variation of evaporation speed leading to formation of non-uniform films with moderately high roughness.

2.5 Other Characterization Techniques

2.5.1 X-ray Photoelectron Spectroscopy (XPS)

X-ray photoelectron spectroscopy (XPS) technique is used to investigate the chemical state, elemental identification and the relative composition of the constituent elements present in the sample.¹¹¹ When a sample is irradiated with mono energetic photon of energy $h\nu$, it emits electrons from the sample surface. A XPS spectrum is represented by the variation of the intensities of the photoelectrons with respect to its kinetic energies or in terms of the binding energies. From the energy conservation principle, the kinetic energy of the emitted electrons is given as:

$$K.E = h\nu - E_B - \phi \dots\dots\dots (2-1)$$

where, $h\nu$ is the energy of the incident photon, E_B is the binding energy of the electrons in the core level from which it is ejected and ϕ is the work function of the sample. Generally the work function of the material is difficult to investigate accurately. Thus, in real experiments, the kinetic energy is expressed in terms of the work function of the spectrometer in the way as shown in Figure 2-13. This is quite logical since we calibrate the binding energy scale with respect to the Fermi level and the kinetic energy of the photoelectrons is measured by the spectrometer and both of them are maintained at common potential.

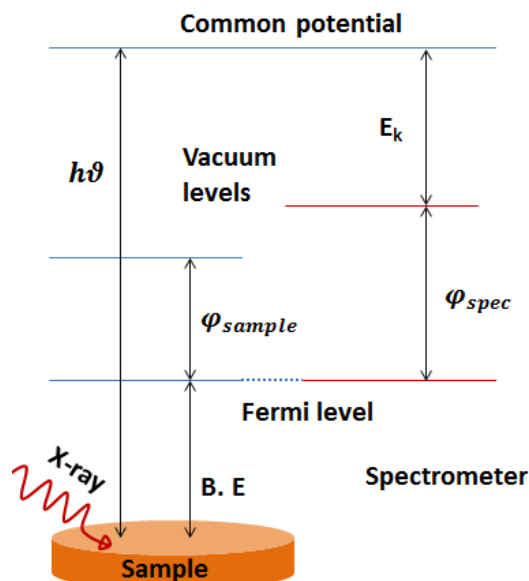


Figure 2-13 Schematic diagram describing referencing the work function of the sample with respect to spectrometer. The photoelectrons are detected only when $h\nu \geq \text{B.E.} + \phi$. For excitation purpose, the conventional X-ray sources mostly used are Al K_α source (~ 1486.6 eV) and Mg K_α source (~ 1253.8 eV). In this energy range, the inelastic mean free path (IMFP) is approximately 0.3–4 nm, which can be estimated from the universal mean free path curve. Thus, XPS is a surface sensitive technique. The best way to probe throughout the depth of the sample is to tune the excitation energy so that the IMFP can be varied and thus chemical information from different depth of the sample can be easily obtained. With the advent of the synchrotron sources, one can easily tune the excitation energy to measure the XPS spectrum at different depth.

Other ways include variation of the take-off angle of the analyser where the ejected photoelectrons are collected and simultaneous collection of the XPS spectrum by etching the film surface in a controlled manner.

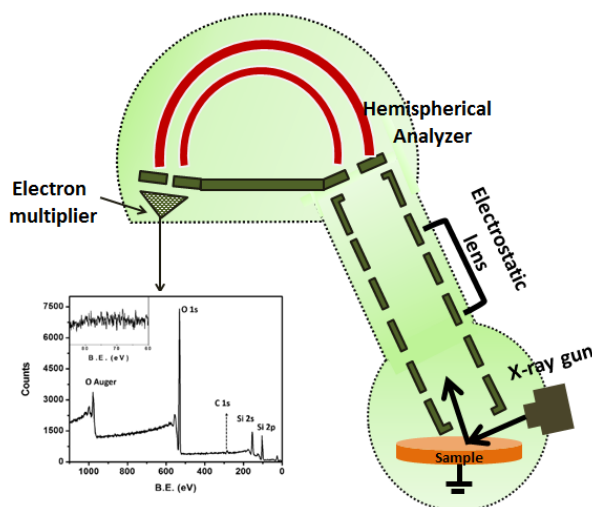


Figure 2-14: Diagram of X-ray photoelectron spectrometer used for experimental purpose for this thesis.

The photoelectron spectroscopy chamber consists of three major components 1)- A X-ray photon source, 2)- An electron energy analyser and 3)- An electron detector as shown in Figure 2-14. Inside the chamber, ultrahigh vacuum of the order of $\sim 10^{-10}$ mbar is maintained in order to increase the mean free path of photoelectrons. The monochromatic X-ray photon source is used for excitation and the energy of the photoelectron depends on it. The electrostatic analyser consisting of the electrostatic lens, the hemispherical elements and the detector (basically an electron multiplier tube) collects the ejected photoelectron and finally we obtain the XPS spectrum.

During the measurement process, initially a survey scan is recorded with higher energy interval. The survey scan consists of core-level peaks as well as the Auger peaks over the inelastic scattering background. One can distinguish Auger peaks by measuring XPS spectrum with different X-ray sources, because in the B.E. scale Auger peak positions depend on the X-ray source.

In the next step, fine scan of the different core levels is recorded with small steps of K.E/B.E. The peak positions of various core levels indicate that the binding energy values are fingerprint of different elements. For p, d & f core-levels, presence of doublets are observed, which corresponds to the different value of the total angular momentum 'j'. The separation between the two different doublets is known as spin orbit splitting (SOS) and the peak area ratio between the doublets depends on the degeneracy of each of the state 'j'. Both SOS and peak area ratio serves as important clue for elemental identification.

The prime advantage of XPS is that one can evaluate sample composition quantitatively. To estimate the composition or stoichiometry of a compound one needs to evaluate the intensity of the photoelectrons of different core-levels of the elements present in the compound, i.e, to evaluate the peak areas. However, to obtain correct value of the peak area one must subtract the background contribution. The intensity of photoelectrons corresponding to the core-level of an element 'x' can be expressed as-

$$I_i = C_i \sigma_i l_i K \dots\dots\dots (2-2)$$

Where, C_i is the average atomic concentration σ_i is the photoelectron cross-section and l_i is the inelastic mean free path of element 'i' in the measured energy range. K is related to all the other factors on which an XPS signal depends. With the prior information of σ_i & l_i along with the measured I_i of different core levels, one can acquire information about composition quantitatively.

2.5.2 Secondary Ion mass Spectrometry (SIMS)

Secondary mass ion spectrometry is a surface sensitive technique widely used to analyze the in-depth composition of thin films by sputtering of bulk samples using a primary beam. The

primary beam is generally a positive (e.g. Cs^+) or negative (e.g. O^-) ion. As the primary ion beam impinges upon the sample surface, generation of secondary ions, neutral atoms and molecules begins with the interaction. Depending on the composition of the specimen different types of the secondary ions are generated, which are directed towards mass spectrometer where detection process is carried out. The choice of the type of the primary beam is very crucial for the analysis of the secondary ions generated. If we choose positive ion for bombardment, then generally negative ions are generated & vice versa.

Nowadays, one of the most popular detection techniques is Time of Flight (TOF) mass spectrometry.¹¹² It is based on the fact that ions with the same energy but different masses travel with different velocities.

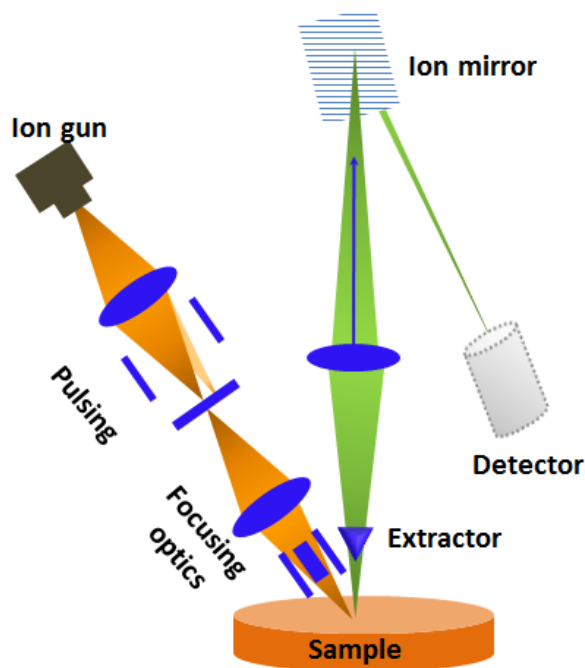


Figure 2-15 Schematic diagram of a TOF-SIMS set up.

The instrumentation for TOF-SIMS measurement consists of a primary beam source, a column for accelerating & focusing the beam, mass spectrometer, which separates the ions according to charge by mass ratio and a detection medium as shown in Figure 2-15. The whole system is kept

inside a high vacuum chamber (pressure $\sim 10^{-6}$ mbar) in order to avoid collision of the secondary ions with the residual gases present inside the chamber environment. During the measurement process when the primary ions and the generated secondary ions stabilize, then accurate composition can be known in a quantitative manner. During the measurement, one records the counts of the different ions having different charge to mass ratio over the complete sputtering time. However, if one measures the total thickness of the sample sputtered during measurement using X-ray reflectivity or by surface profilometry, then, by knowing the sputter yield the thickness can be easily calibrated. Finally, one obtains the variation of the intensity of different ions based on the charge to mass ratio with respect to the sample thickness.

The most important advantage of this technique is that samples with very low concentration down to ppb level can be analyzed. Other application includes depth profiling of thin layers or the imaging of the surfaces. The main limitation includes the effect of sputtering which may lead to deterioration of sample surface or may include artifacts which mislead a lot of information. Sometimes, in case of insulators effect of charging can also provide misleading information. Another limitation is that it is destructive in nature.

Chapter 3.

Structural, optical and compositional analysis of aluminum oxide (Al_2O_3).

In this chapter, the optical properties of reactive sputtered aluminum oxide thin film are investigated in the wavelength region of 60-200 Å (~206-62 eV) covering the Al $L_{2,3}$ edge. The optical properties of the thin film are compared with that of α - Al_2O_3 in its single crystal form. Both the Al L & O K-edges of α - Al_2O_3 are probed. The investigated optical properties are also compared with the existing available literature.

This chapter also shows the capability of soft X-ray reflectivity (SXR) technique to quantify the depth-resolved compositional details of the film. Modelling of optical constants profile obtained from the angle-dependent reflectivity data is used to evaluate the qualitative composition of the principal and the interfacial layer of the film which corroborates well with the X-ray photoelectron spectroscopy results.

3.1 Introduction:

Aluminum oxide (Al_2O_3) has many superior qualities such as high mechanical strength, excellent dielectric properties and good adhesion to many surfaces. In literature, it is shown as a superior spacer layer to achieve good stability¹¹³ and high reflectivity performances.^{114,115} A detailed description of the application of aluminum oxide in X-ray optics is discussed in Section 1.5 of Chapter 1. In the present chapter, we focus on the optical properties of aluminum oxide in the EUV/ Soft X-ray region covering the edge region and its relation to the film composition/stoichiometry.

Now we present a literature survey on the study of optical properties of aluminum oxide thin films. A study to compare optical response of sapphire crystal ($\alpha\text{-Al}_2\text{O}_3$) and electron beam deposited amorphous alumina have been performed in 145-185 Å wavelength range (~67-86 eV) to understand the effect of crystalline nature of alumina near Al $L_{2,3}$ edge.¹¹⁶ It was reported that the optical constants of amorphous and crystalline alumina are different near the Al L absorption edge, though they match with each other away from the absorption edge. It is important to note that the measurements were carried out at discrete photon energies.

The optical properties not only rely on the state of the sample but also on their composition or stoichiometry which is again dependent on the deposition techniques and its condition. J.Y. Jung¹¹⁷ has studied optical properties of alumina thin films in Visible- IR region with variation of stoichiometry over a wide range of film composition. French et.al¹¹⁸ investigated the optical properties of $\alpha\text{-Al}_2\text{O}_3$ by Vacuum Ultraviolet (VUV) spectroscopy and Electron Energy-Loss spectroscopy (EELS) within the energy range of 6 to 142 eV. They have concluded that the determination of optical constants are not only sensitive to sample preparation method but also

depends on the measurement technique. Therefore, a comparison of various data sets is the only way to understand the uncertainty in the information content of the final results.

As discussed in Chapter 1, it is also important to understand the relation between the experimentally measured optical constants with the chemical bonding and electronic structure of the material. The optical constants (δ & β) relating to dispersion and absorption spectrum is closely connected to the electronic structure of the material. Formation of defects states, core-exciton states etc. leads to modification in the electronic structure and the same is mapped in its optical constants spectra. Near the absorption edge region, the influence of the core-hole effect is generally visible for few special type of material. The effect of a localized core hole on the optical properties is found to be more prominent in case of strong insulators because of their less screening ability of electrons. Studies on the influence of the core hole^{119,120,121,122} and formation of excitonic like states on the electronic structure and absorption spectrum of oxides like Al_2O_3 , MgO & SiO_2 are widely discussed in literature.^{123,124,125,126} Experimental evidences of this effect is highly dependent on the resolution of the measurement. In this Chapter we have also attempted to address the influence of core-hole effect on the optical constants (both dispersion & absorption spectra) of $\alpha\text{-Al}_2\text{O}_3$ near the Al $L_{2,3}$ -edge.

For practical purposes and useful real applications, mere estimation of optical properties of the thin films does not complete the aim, investigation of the in-depth composition and structure is equally important. Depending on the deposition technique and the different parameters used for deposition, the film quality, composition, stoichiometry etc. may vary. Numerous studies on compositional details as well as depth profiling in aluminum oxide thin films have been carried out using different techniques. E. P Gusev et al.¹²⁷ have used a combination of different techniques like-nuclear resonance profiling (NRP), medium energy ion

scattering (MEIS) and high resolution transmission electron microscopy (HRTEM) to obtain in-depth profile of the CVD deposited alumina films. They have also explored the microstructural aspects of the films. Most of the interface studies reported on aluminum oxide thin films are based on the destructive methods. Thus, application of these destructive techniques for surface & composition studies can lead to additional modifications in film and interface region, tailoring its properties. Thus, it is desirable to investigate film composition by applying non-destructive techniques. To the best of our knowledge the interface studies on aluminum oxide thin films using a non-destructive technique is rather scarce.

Unlike the available conventional techniques, soft X-ray reflectivity based non-destructive technique serves to be efficient for in-depth compositional analysis. In the soft X-ray region, the energy-dependent optical constants (δ & β) changes drastically especially near the absorption edges of constituent elements. Thus, SXR technique is widely used for element sensitive analysis by tuning the energy of X-rays to the absorption edges of specific elements to be investigated. Moreover, unlike the X-ray photoelectron spectroscopy technique which is capable of providing information up to a certain depth of the material ($\sim 50\text{-}70$ Å), the SXR technique gives the in-depth compositional details upto a depth of $500\text{-}700$ Å, depending upon its penetration depth, which is again dependent upon the energy of the X-ray photon.

Few literatures are available that have focused on the unique feature of SXR technique in the investigation of the depth-resolved compositional details of thin films. Singh et al.¹²⁸ have investigated compositional details of silicon rich silicon nitride (SRSN) thin film utilizing SXR technique. They observed that the measured optical index profile of their SRSN layer lies in between the reference profile of Si and Si_3N_4 . The measured profile was used to determine the fractional composition of Si and Si_3N_4 in the SRSN film. M. Zwieler et al.¹²⁹ have shown that

the SXR technique in resonant mode can be used to obtain electronic depth profile with Å-resolution. They have shown that the effects in X-ray reflectivity near the absorption edges are caused by rapid variations in X-ray optical properties owing to a periodic arrangement of the resonating lattice planes. J. Bai et al.¹³⁰ have carried out X-ray reflectivity measurements near the K-absorption edges of Fe and Cr of a Fe/Cr multilayer system. They obtained the information of the electron density as well as the compositional profile of the multilayer.

In the present study, optical constants of a sputter deposited aluminum oxide thin films are measured using the angle dependent reflectivity technique in the energy range of 62-206 eV (~200- 60 Å in terms of wavelength), covering the Al L-edge region. Measured optical constants obtained are compared with the tabulated data available from the CXRO website⁷⁵ as well as with few other databases¹³¹.

Next, energy-dependent reflectivity measurements are carried out on α - Al_2O_3 substrate also near the Al L-edge and O K-edge region, and simultaneously the continuous spectra of optical constants are evaluated from phase extraction using KK relation. Comparison of the optical constants of the thin film with that of α - Al_2O_3 substrate is carried out.

Finally, X-ray photo electron spectroscopy (XPS) measurements are carried out to establish the chemical composition of the film. We have also carried out a depth resolved compositional analysis of an aluminum oxide thin film using non-destructive SXR technique. The SXR technique is applied to obtain the optical index (δ & β) profile of principal layer and interface region and simultaneous optical modelling is carried out to investigate the in-depth compositional details. The results of optical modelling are compared to the information obtained from the XPS technique.

3.2 Experimental details:

The aluminum oxide film was deposited on a Si substrate using reactive sputtering technique. The sputtering of a pure Al target (~99.9995% purity) was carried out in oxygen ambient using a pulsed DC power supply source. Argon was used as the sputtering gas. The Ar and O₂ flow rates were set at 15 sccm (standard cubic centimeter) and 60 sccm respectively. The base pressure of the system was 9.3×10^{-8} mbar before the deposition. Prior to the deposition, the Si substrates were cleaned by a standard RCA cleaning process. This process involves the removal of insoluble organic contaminants with H₂O:H₂O₂:NH₄OH solution. A thin silicon dioxide layer and metallic contaminants were removed using H₂O: HF solution. Ionic and heavy-metal contaminants were removed using H₂O:H₂O₂: HCl solution. After the standard process, the native oxide is etched by dipping in 2% HF for 30 s, followed by rinsing in de-ionized water.

Grazing incidence X-ray Diffraction (GIXRD) spectrum was recorded using a Bruker D-8 diffractometer. The glancing angle was fixed at 0.5° to limit the penetration of the beam into the film. The data was recorded in the range of 30-80° in the step of 0.03° and 10 second acquisition time.

To determine chemical composition, XPS measurements were carried out using Al source operated at an anode voltage of 10 kV and an emission current of 10 mA. Samples are etched by Argon ion beam (4 kV, 1 μA) to clean the sample surface and for chemical depth profiling. Survey scans are collected over 0 – 1400 eV kinetic energies. Detailed core scans are then performed to find the oxidation state of the constituent elements. XPS data have been recorded for as deposited and after different (10, 20, & 30 minutes) sputtering time cycle. XPS spectra have been de-convoluted using Gaussian de-convolution method.

To obtain information about structural parameters like thickness and roughnesses, Grazing incident X-ray reflectivity (GIXRR) measurement were performed using Bruker D-8 system which consists of a goniometer and a Cu K_α X-ray source (1.54 \AA). The GIXRR measurements were performed in 0.005° angular step size to observe the fine features of the Kiessig fringes.

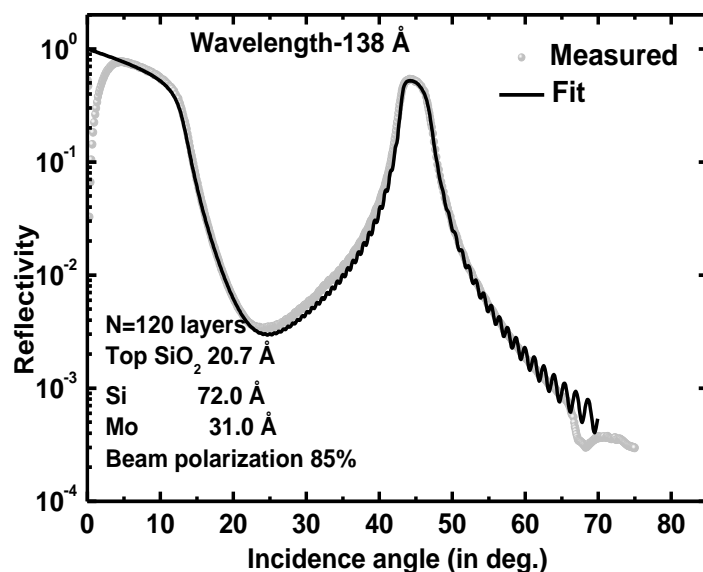


Figure 3-1 Reflectance curve of 60 layer pair Mo/Si multilayer of a period of 103 \AA measured at $\lambda=138 \text{ \AA}$. The Bragg peak located near Brewster angle provides precise information about the polarization content.

Soft X-ray reflectivity (SXR) measurements were carried out using a high vacuum soft X-ray reflectometer at the reflectivity beamline of Indus-1 synchrotron radiation source. In the beamline, the polarization state of the incident beam was checked by using a 45° Bragg reflection multilayer. A Mo/Si multilayer of $d=103 \text{ \AA}$ ($\text{Si } 73 \text{ \AA} / \text{Mo } 31 \text{ \AA}$) $_{\times 60}$ was used which gives a first Bragg reflection near 45° for $d=138 \text{ \AA}$. The analysis of the reflectivity pattern of the multilayer as shown in Figure 3-1 suggests that the incident beam is 85% s-polarized. This information is used in analyzing the soft X-ray reflectivity data of the aluminum oxide thin film.

3.3 Results and discussions:

3.3.1 GIXRR analysis

Figure 3-2 shows the measured and fitted GIXRR curve of 240 Å thickness aluminum oxide thin film deposited on Si substrate. The analysis of the curve has been carried out by taking into account suitable layers of different densities. As initial guess, a single layer of aluminum oxide with its density corresponding to bulk (3.97 g/cc) is considered on top of the Si substrate. In spite of density reduction as compared to bulk, the fit was not found to match and the χ^2 value was also high. Next, in the fitting model an additional layer was added over the substrate having the density of substrate native oxide (SiO₂), still lacking the best fit. Finally to obtain a best fit, a three layer model as shown in the inset of the Figure 3-2 is used. The model consists of an interfacial layer near the Si substrate, a principal aluminum oxide layer and a top surface layer arising due to interaction of the surface with the ambient. The structural parameters i.e. thickness and roughness of the different layers of the film as obtained from our analysis are tabulated in Table 3-1.

Table 3-1 Structural parameter of the aluminum oxide thin film from GIXRR analysis

Layer	Thickness (Å)	Roughness (Å)
Top	30±1.5	5.0
Principal Al-O	240.0±2.0	4.0
Interface	18±2.0	7.9
Substrate	--	5.4

In the next step we derived the Scattering length density (SLD) profile using the fit parameters as shown in Figure 3-3. The SLD resembles the scattering power of a material. The SLD has both real and imaginary part and it is related to the optical constants as: $\rho = \frac{2\pi}{\lambda^2} \times \delta$ and $i\rho = \frac{2\pi}{\lambda^2} \times \beta$. The SLD profile in Figure 3-3 shows that the film is uniform across the depth except near the top

surface. The density obtained from the GIXRR analysis is found to be 2.93 g/cc, which is 73% of the bulk density of stoichiometric Al_2O_3 (3.97 g/cc).

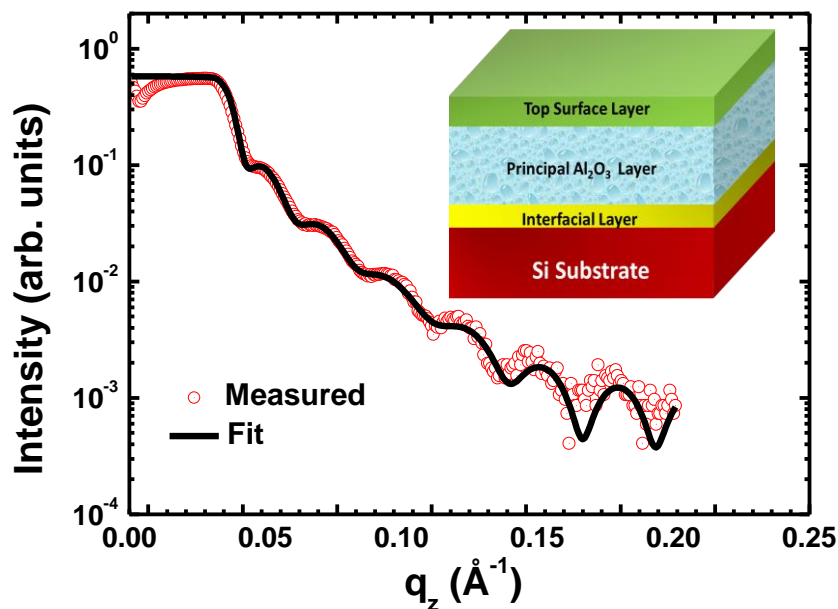


Figure 3-2 Measured (open circles) and fitted (continuous line) GIXRR spectra of aluminum oxide thin film as a function of momentum transfer vector q_z is shown. Schematic of three layer model used for the fitting is also shown.

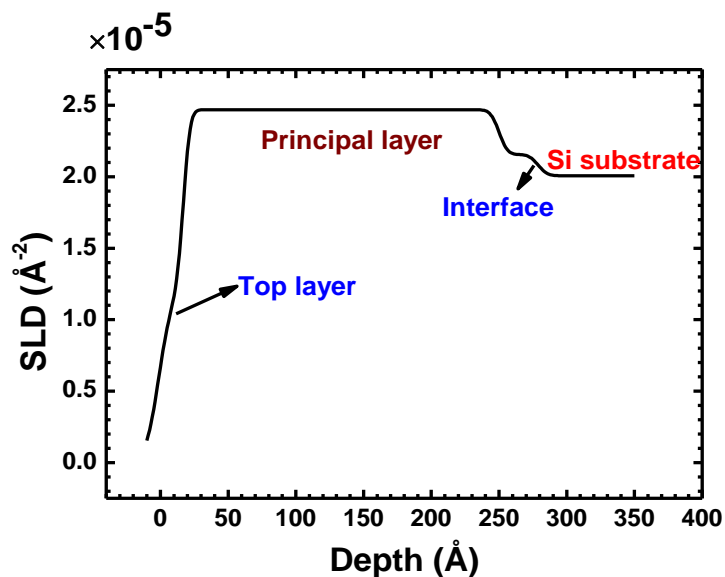


Figure 3-3 Scattering length density (SLD) profile derived by modelling the parameters obtained from the analysis of the GIXRR curve. The region of different layers is marked in the SLD profile.

The error or accuracy in density parameter depends on measurement accuracy of critical angle. In GIXRR analysis, the critical angle is not a fitting parameter and therefore error in curve fitting cannot be directly linked to define an error in density or in critical angle. To know the exact value of critical angle from a GIXRR curve, its well defined shape, especially below θ_c region is required. The shape of reflectivity curve below the critical angle region depends on the $\frac{\beta}{\delta}$ ratio. If $\beta/\delta < 1$, i.e., absorption is not dominant, then critical angle θ_c can be calculated from the relation- $\theta_c = \sqrt{2\delta}$, where δ is related to the density of the film. Another important parameter which helps in defining correct critical angle is goniometer accuracy in angle measurement. This angle accuracy defines the accuracy of the critical angle (θ_c) measurement.

In GIXRR experiment, the measurement error in density analysis can be obtained from the relation - $\frac{d\rho}{\rho} = 2 \left(\frac{dq}{q_c} \right)$. For aluminum oxide $\rho = 2.93 \text{ g/cc}$, (as obtained from the fit value of δ), the step size of momentum transfer (q_z) is 0.0007 \AA^{-1} and the critical angle in terms of q_c is 0.0359 \AA^{-1} this yields an error in density determination of $\sim 0.12 \text{ g/cc}$.

The analysis error in density determination can be estimated by calculating the difference between critical angle of measured and fitted GIXRR curve. From Figure 3-2, the difference between the critical angle (θ_c) of the fitted and the measured GIXRR curve is found to be $\Delta\theta_c \approx 0.004$. Thus, the error in density is $d\rho = 0.0929 \text{ g/cc}$.

In Figure 3-3 the hump in the SLD profile near the Substrate/ Film interface indicates about the presence of interlayer whose composition is different from the substrate native oxide. The interlayer may form during the initial stage of growth of alumina film where the Al atoms interact with the Si and native oxide layer. In the present case the thickness of this interlayer is

found to be 18 Å. The exact composition of the interlayer can be estimated from the optical constants profile as investigated further.

3.3.2 Determination of Optical Constants

To determine the optical constants in the soft X-ray region of 60-200 Å (~206-62 eV) the angle-dependent SXR experiments are carried out at Indus-1 reflectivity beamline. Measured and fitted SXR data are shown in the Figure 3-4 (a) for different incident wavelengths in step of 10 Å. In the close vicinity of the Al L absorption edge (~170 Å) the SXR measurements are carried out in 0.5 Å and 1 Å step size and those are shown in the Figure 3-4 (b). The SXR data are fitted with the same three layer model which was earlier used for GIXRR data analysis. The information of structural parameters obtained from the GIXRR analysis are kept fixed while processing SXR data. This approach reduces the number of variable parameters in the fitting process of the soft X-ray reflectivity data. In this scenario, the only variables are the optical constants (δ & β) of the different layers used in the model.

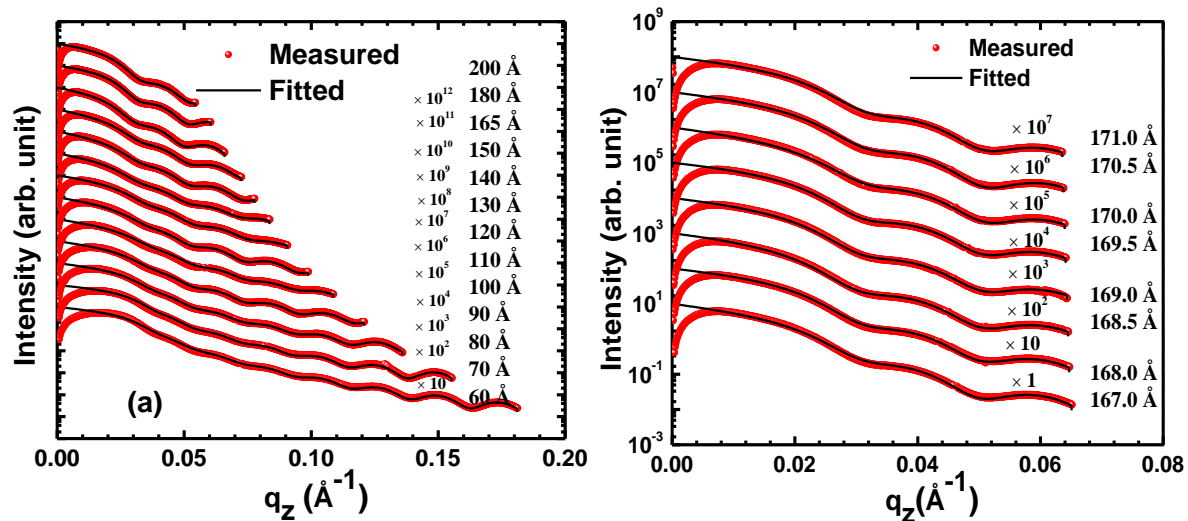


Figure 3-4 Measured (circle) and fitted (solid line) angle dependent SXR spectra of aluminium oxide thin film are shown for different wavelengths in (a) 60-200 Å (~206-62 eV) region. (b) Near the Al L absorption edge (170Å/73 eV). For the sake of clarity the curves are vertically shifted by a constant factor as shown in the figure.

In Figure 3-5 the experimentally determined values of optical constants and Henke's values obtained from the CXRO website for Al_2O_3 film calculated for the density values of 3.97 g/cc (bulk density) & 2.93 g/cc (as obtained from GIXRR analysis) are shown. The experimentally obtained optical constants values are also listed in the Table 3-2.

In case of aluminum oxide layer the obtained delta and beta values are 5-33% higher than the tabulated values except near the Al L absorption edge ($\sim 170 \text{ \AA}/73 \text{ eV}$) where the delta values are 50-120 % higher and the beta values are 7-20% lower.

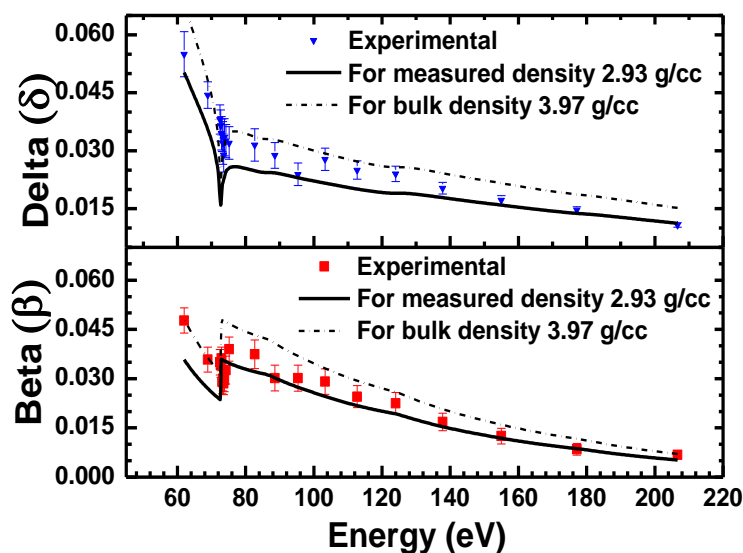


Figure 3-5 The measured optical constants of the aluminium oxide thin film (principal layer) are compared with the Henke's tabulated values obtained from the CXRO website for bulk density as well as for the measured density of 2.93g/cc.

To understand this variation in optical constants of the present film with stoichiometric Al_2O_3 data, the optical constants for two different density case a) 2.93 g/cc as obtained from GIXRR analysis and b) 3.97 g/cc bulk density are also calculated and compared with the obtained experimental results. It seems that the measured optical constants values are closer to the Henke's values for reduced density.

Table 3-2: Measured values of optical constants of off stoichiometric aluminum oxide thin film are listed along with Henke's tabulated values of Al_2O_3 for reduced density 2.93 g/cc in the 60–200 Å (~206–62 eV) region

Energy (eV)	Wavelength (Å)	δ (exp)	δ (Henke)	β (exp)	β (Henke)
206.64	60	0.0108	0.01123	0.007	0.00523
177.12	70	0.0147	0.01379	0.008	0.00867
154.98	80	0.017	0.01594	0.012	0.01186
137.76	90	0.020	0.01787	0.017	0.01538
123.98	100	0.024	0.019	0.022	0.01929
112.71	110	0.025	0.02009	0.024	0.02179
103.32	120	0.028	0.02161	0.029	0.0246
95.37	130	0.024	0.02301	0.030	0.02737
88.56	140	0.029	0.02426	0.030	0.03025
82.65	150	0.031	0.02483	0.037	0.03212
75.14	165	0.032	0.02548	0.039	0.03474
74.24	167	0.032	0.02467	0.032	0.03517
73.80	168	0.033	0.02327	0.029	0.03539
73.58	168.5	0.029	0.02256	0.028	0.03551
73.36	169	0.032	0.02184	0.03	0.03562
73.14	169.5	0.034	0.02112	0.029	0.03574
72.93	170	0.034	0.01793	0.036	0.03586
72.71	170.5	0.036	0.01606	0.034	0.02745
72.51	171	0.038	0.01735	0.035	0.02364
68.88	180	0.044	0.03559	0.036	0.02703
61.99	200	0.055	0.05027	0.048	0.03579

In the soft X-ray region the measured values of optical constants of Al_2O_3 film is reported by Palik¹³² and Hagemann¹³³ also. The results of their finding are plotted in Figure 3-6 (a) & (b) and compared with the present experimental data. Henke's data obtained from the CXRO website for Al_2O_3 of bulk density 3.97 g/cc and reduced density 2.93 g/cc are also shown. It is obvious that both the Palik and Hagemann data exhibit a large deviation from the Henke tabulated values. The data reported by Hagemann was measured on vacuum evaporated amorphous alumina film where the sample may have significant deviation in film stoichiometry. Interestingly the feature corresponding to $L_{2,3}$ spin orbit coupling is visible in Hagemann beta values near 158.9 (78 eV) and 159.9 Å (77.5 eV) whereas the Palik data shows a smooth variation in this region.

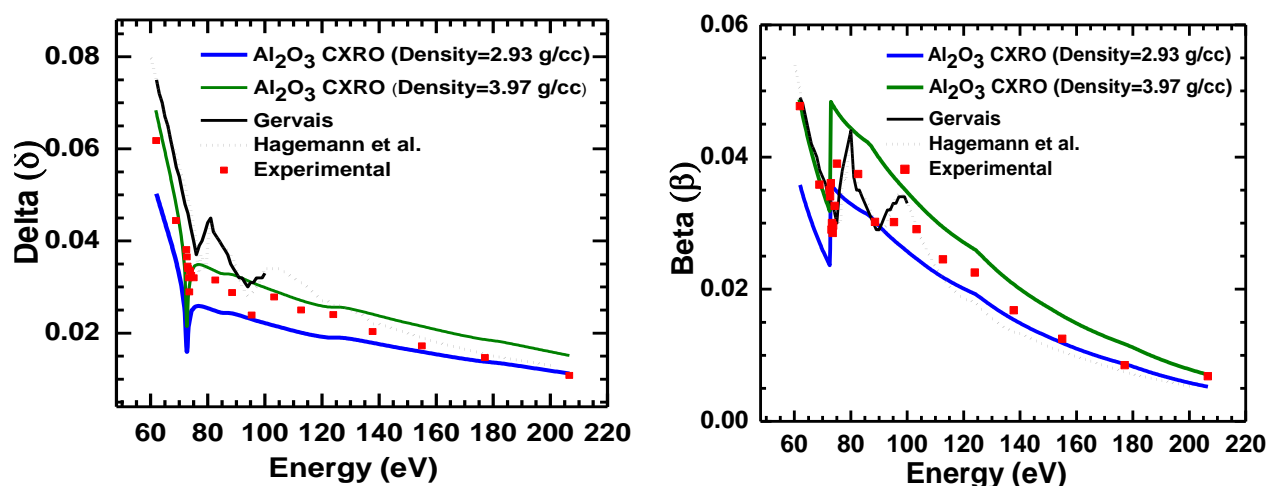


Figure 3-6 Comparison of (a) delta (δ) and (b) beta (β) of aluminum oxide thin film obtained from Henke, Palik, and Hagemann literature with the present experimental data.

Further, the delta values reported by Palik and Hagemann are higher compared to those of Henke values whereas the beta values of Hagemann and Palik are lower to those of Henke values. This discrepancy generally cannot be understood if their film comprised stoichiometric Al_2O_3 phase. Increase in delta and decrease in beta value could be possible if unreacted Al and Oxygen are present in a significant amount. From the density point of view, if the film density varies it leads to change in delta (δ) and beta (β) values simultaneously. In the present study both delta (δ) and beta (β) values are found to be less than the Henke data corresponding to bulk density. It seems that the reduced film density and off stoichiometric nature of the present film are mainly responsible for a large mismatch observed between the experimental values and the Henke's tabulation. To correlate the experimentally obtained optical constants values with the film composition further analysis is carried out.

3.3.3 Optical constants spectra of α - Al_2O_3 near Al $L_{2,3}$ and O K-edge.

In the next step we have determined the optical constants of α - Al_2O_3 near the Al $L_{2,3}$ and O K-absorption edge regions utilizing energy dependent soft x-reflectivity(SXR) technique. The

measurements were carried out at an incidence angle of 5° & 3° respectively for the Al $L_{2,3}$ and O K-edges using s-polarized radiation. The reason behind the choice of the incidence angle is discussed in Chapter 1. Applying the Kramers-Krönig (KK) relations to the energy dependent SXR data, the phase $\phi(E)$ of the reflected electric field is calculated. Finally knowing the phase as well as the reflectivity, the optical constants (δ & β) are evaluated using the Fresnel's reflection co-efficient formula for s-polarized light.

The optical constants profile near the Al $L_{2,3}$ absorption edge region shows the resolved L_2 and L_3 features separated by an energy value of 0.4 eV, i.e., spin orbit splitting (SOS) value is 0.4 eV. The features appearing in the optical constants profile near the O K-edge region are comparatively broader. The appearance of these broad features is in accordance with the absorption spectra available in literature and also with the TEY spectrum measured at soft X-ray reflectivity beamline (BL-03)¹⁰⁶ of Indus-2 synchrotron radiation source. The origin of these features appearing near the edge region is also discussed.

3.3.1.1 Energy dependent SXR measurements

Soft X-ray reflectivity measurements were carried out in the energy region of 45-150 eV covering Al $L_{2,3}$ edge at metrology beamline of synchrotron SOLEIL.¹³⁴ While measurement the resolution is maintained at 2500 through the complete energy range of 45-150 eV with the slit size of 100 & 200 μm . The reflected beam is recorded using a soft X-ray silicon photodiode detector with Al coating. The measurements were carried out at different incidence angles of 5° , 7° & 10° . However, the spectra measured at 5° was considered for the evaluation of optical constants profile near the Al $L_{2,3}$ edge region since the critical angle of α - Al_2O_3 in this energy region is above 5° .

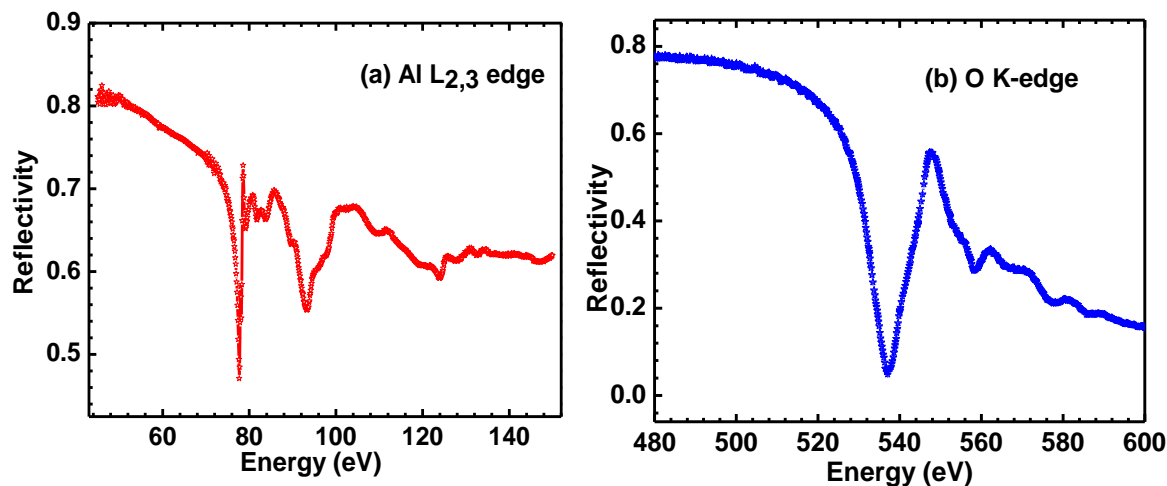


Figure 3-7 (a) Shows the reflectivity spectrum of α - Al_2O_3 measured at an incidence angle of 5° covering the Al $L_{2,3}$ edge region. (b) Shows the reflectivity spectrum near the O K-edge region measured at an incidence angle of 3° .

On the other hand, measurement near the O K-absorption edge was carried out at BL-03 of Indus 2 at an incidence angle of 3° . Figure 3-7 (a) shows the energy dependent soft X-ray reflectivity spectrum of α - Al_2O_3 near the Al $L_{2,3}$ edge measured at a grazing incidence angle of 5° , whereas (b) shows the data near the O K-edge region measured at 3° . To evaluate the optical constants profile of the sample near the Al L- & O K-edge region we have used the reflectivity spectra measured at these two different edges. From the knowledge of the measured reflectivity profile the phase information has been retrieved using the KK relation. To minimize the error in the phase determination using KK relations, the reflectivity data outside the measurement range is calculated. This calculation is carried out using the optical constants extracted from the CXRO database outside the measured energy range. Finally the obtained spectrum is stitched with the experimental spectra on both the higher and lower energy side of the absorption edge region where experimental data is not available. In the present analysis, the phase error term of $\pm\pi$ is also considered in phase calculations. Once we know the phase, using the Fresnel's reflection formula for s-polarized radiation, the optical constants profiles of the films are evaluated for both the absorption edge region.

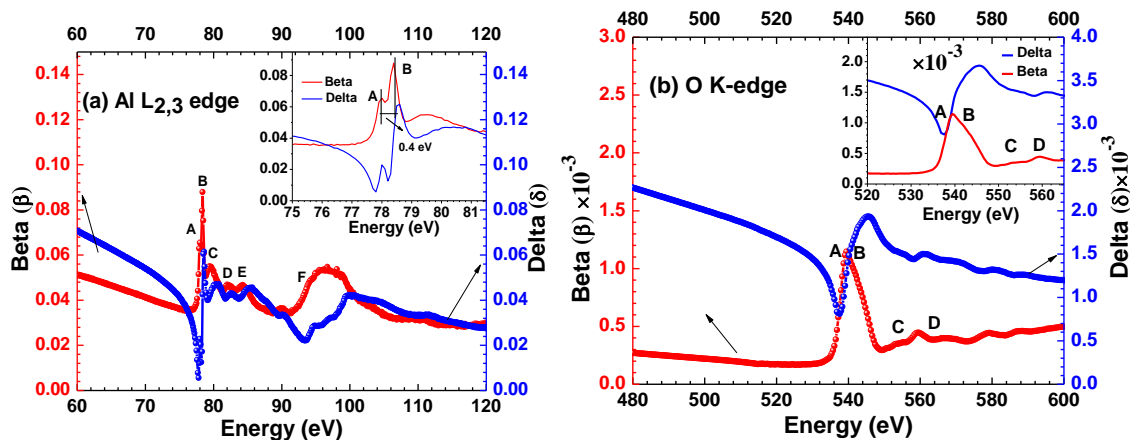


Figure 3-8 (a) shows the obtained optical constants (δ & β) profile near the Al $L_{2,3}$ edge region where the features are marked from A to F. Inset shows the well resolved L_2 and L_3 edge features with a SOS of 0.4 eV. (b) shows the optical constants (δ & β) profile near the O K-edge region where the salient features are marked from A to D.

Figure 3-8 (a) shows the optical constants profile obtained in the 45-150 eV energy region covering Al $L_{2,3}$ edge region. The obtained beta (β) profile matches quite well with the Al $L_{2,3}$ absorption spectrum^{135,136} in terms of energy position. Unlike the conventional absorption spectrum which is arbitrary in nature, beta (β) profile provides absolute information about the absorption co-efficient of a material. Together with the beta (β) and delta (δ) value the complex index of refraction of a material can be known.

The features appearing in Figure 3-8 (a) are marked from A to F. On the other hand, the inset of the Figure 3-8 (a) shows the edge region with well resolved peaks A & B separated by an energy value of 0.4 eV. These well resolved peaks correspond to the L_2 & L_3 feature of Al in α - Al_2O_3 and are located at an energy position of 78.0 eV (Peak A) & 78.4 eV (Peak B) respectively. According to literature^{137,138,139} the doublet features A & B are often referred to as Al $L_{2,3}$ exciton. The spin orbit splitting is found to be 0.4 eV which is slightly less than the literature value of 0.47 eV but well within the resolution of measurement. There are several speculations about the origin of the core-hole/exciton features (marked as A & B in our case) for α - Al_2O_3 . It is described in refs.^{137,138} that the exciton is formed from an Al 3s level which is pulled down in

the band gap under the influence of core-hole potential. According to ref. ¹²³ the presence of a short Al-Al bond is responsible for the appearance of excitonic like feature in α - Al_2O_3 . The short Al-Al bond leads to the overlap of these two wave-functions on the cationic sites.

In simple words, α - Al_2O_3 , being a strong insulator with prominent ionic character has less screening due to absence of valence electron on the cation (Al^{3+}) site. This strengthens the core-hole potential on the cationic site that leads to the appearance of Al $L_{2,3}$ exciton doublet marked as A & B. The higher energy features marked from C to F are related to the transitions from Al 2p state to the Al d (t_{2g} and e_g) states. The appearance of the higher energy features is also related to the molecular fields of the oxygen atoms on the Al absorption process.¹³⁶ The intensity ratio of the peaks corresponding to L_2 and L_3 edges is found to be 1.34 which is slightly less than the literature value of 1.65.

Figure 3-8 (b) shows the optical constants profile obtained in the 480-600 eV energy range covering O K-absorption edge region of α - Al_2O_3 . The features appearing in the spectrum are marked from A to D. In the O K-edge, no excitonic feature is observed. This is due to the fact that the core-hole potential associated with O K-edge gets weakened due to screening by the valence electrons on the anion (O^{2-}) site. The origin of the features marked as A & B can be described as a result of transitions occurring from the O 1s states to O 2p states hybridized with Al 3d states which is splitted by crystal field effect. On the other hand the higher energy features marked as C and D originate due to transitions occurring from O 1s to O 2p hybridized with the Al 4s and 4p states. These features are much less intense as compared to the broad feature A & B.

3.3.3.2 Comparison of Optical Constants of $\alpha\text{-Al}_2\text{O}_3$ with that of thin film.

Figure 3-9 shows the comparison of the experimentally investigated fine optical constants spectra of $\alpha\text{-Al}_2\text{O}_3$ with an energy step of 0.1 eV with that of the obtained optical constants of the reactive sputtered aluminum oxide thin film measured at discrete photon energies.

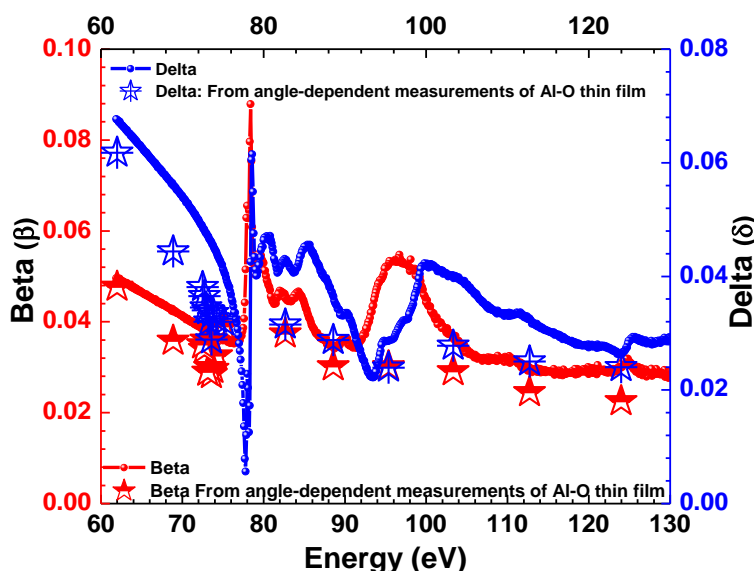


Figure 3-9 Comparison of the experimentally obtained optical constants δ & β of the sapphire ($\alpha\text{-Al}_2\text{O}_3$) with that of the aluminum oxide thin film having a thickness of 240 Å.

It is clearly evident that away from the absorption edge the trend of the optical constants of bulk $\alpha\text{-Al}_2\text{O}_3$ and the thin film matches well with slight difference. Near the Al L-edge region the scenario is different and is difficult to distinguish. The absorption edge energy seems to be different for the two samples because of different Al:O chemical shift. Thus, one can conclude that the optical constants are highly dependent on the state of the sample and also on the deposition technique.

Comparison of optical constants evaluated from Angle & Energy-Dependent SXR techniques

Soft X-ray reflectivity techniques in both the angle & energy-dependent modes can be utilized for investigation of the optical constants in the X-ray region. However, it is also important to

note that there are certain differences in the information obtained from these two techniques which are discussed below.

Angle dependent SXR technique is mostly suitable in case of thin film structure rather than thick crystal owing to its limitation in the angular resolution. In case of angle dependent SXR technique, a complete idea of the layered model of the thin film i.e, its structural as well as the optical constants (δ & β) of the individual layers can be easily determined. However, near the absorption edges, the behavior of the optical constants (δ & β) changes drastically, thus there is a need of angle-dependent measurement at small steps of wavelength/energy. Thus, precise determination of optical constants near the absorption edge using angle-dependent SXR measurement, takes a lot of effort. Another issue lies with the accuracy of the obtained optical constants from this technique, especially near the absorption edges. Near the edge region, the absorption(β) is dominant, thus, the β/δ ratio becomes greater than 1 leading to an exponential like shape in the reflectivity curve. This leads to difficulty in the fitting of the measured angle-dependent reflectivity curve and as a consequence there is an uncertainty in the determined optical constants (δ & β) for most of the materials.

On the other hand, in energy dependent SXR technique, one can easily evaluate the optical constants (δ & β) of a crystal or principal layer of thin film. There is no difficulty in evaluation even near the absorption edge region. However, the only experimental limitation of this technique is that no information about the layered structure of a thin film and its structural parameters are obtained.

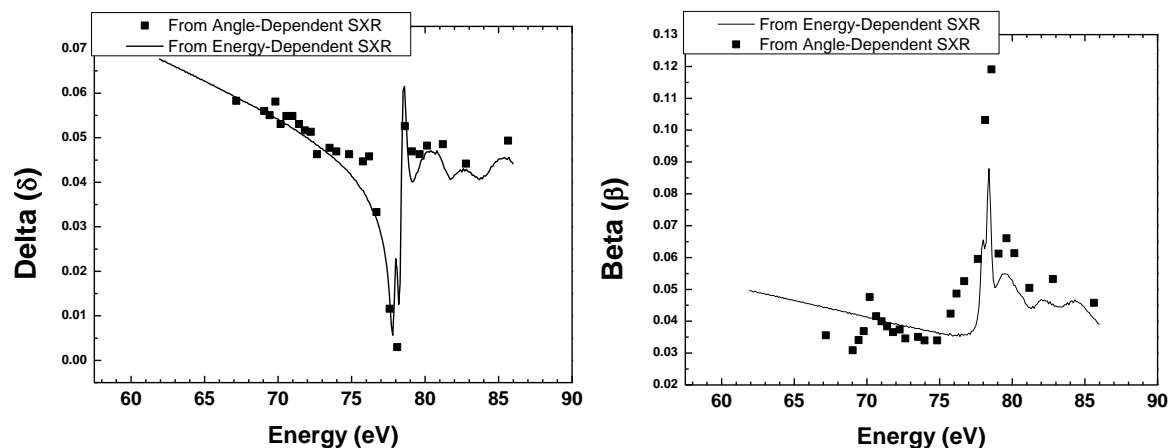


Figure 3-10 shows the comparison of the optical constants of sapphire crystal evaluated from angle-dependent and energy-dependent Soft X-ray reflectivity (SXR) measurements.

Figure 3-10 shows the comparison of the optical constants (δ & β) of sapphire crystal evaluated from the two techniques as mentioned above. For this comparison the optical constants (δ & β) data of sapphire crystal evaluated from the angle-dependent SXR measurements are taken from the earlier work carried out at the Indus-1 soft X-ray reflectivity beamline by Arijeet et al.¹⁴⁰. In their study the R v/s angle measurements were performed near the Al L-edge region with the beamline operating at relatively lower resolution of $\lambda/\Delta\lambda \sim 200$ near the Al $L_{2,3}$ absorption edge energy.

From the figure it is seen that the optical constants investigated from the energy-dependent technique shows the fine features in the spectra clearly, whereas, for the angle-dependent data the features are not clear due to lack of enough measurements near the edge region. It is also evident that the optical constants (δ & β) of sapphire crystal investigated using two different modes of SXR matches well except in the vicinity of the absorption edge. The optical constants evaluated from angle-dependent techniques are found to be over-estimated at the edge region and the reason behind this is already explained in the beginning of this section.

3.3.4. Depth Resolved Compositional analysis of off-stoichiometric film.

It is known that in the soft X-ray region, optical response of a material can be quantified in terms of optical constants which are more sensitive near the absorption edges of the constituent elements. This sensitivity can be attributed to the fact that near the absorption edges the optical properties are largely influenced by the local environment of the material. Thus precise determination of the optical constants near the absorption edges yields in-depth compositional details of the material. The details of the measurements carried out and the modelling approach considered are described below-

3.3.4.1 GIXRD analysis

In case of PVD grown films, high deposition rate leads to the formation of metastable structures as the atoms does not get much time to rearrange themselves so that they can achieve the most energetically favourable position. A number of metastable phases of alumina are reported in literature. These metastable phases can be categorized on the basis of the arrangement of the close packed oxygen sub-lattice.¹⁴¹ Thus it is very important to analyze the phases present in the aluminum oxide thin film. Figure 3-11 shows the glancing angle X-ray diffraction (GIXRD) pattern of aluminum oxide thin film measured at a glancing angle of 0.8° . From the obtained XRD pattern as shown in Figure 3-11 the peak position of 38.5° corresponds to Al (111) plane with slight shift from the actual value and that at 55.2° confirms the existence of rhombohedral phase of aluminum oxide (Al_2O_3). These values are verified from the JCPDS database (JCPDS 46-1212). One can conclude that the film is polycrystalline in nature. Using Debye Scherer formula the particle size is calculated to be 92.8 \AA . The X-ray diffraction pattern does not

provide further information about the composition of the film throughout its depth which led us to explore using other techniques.

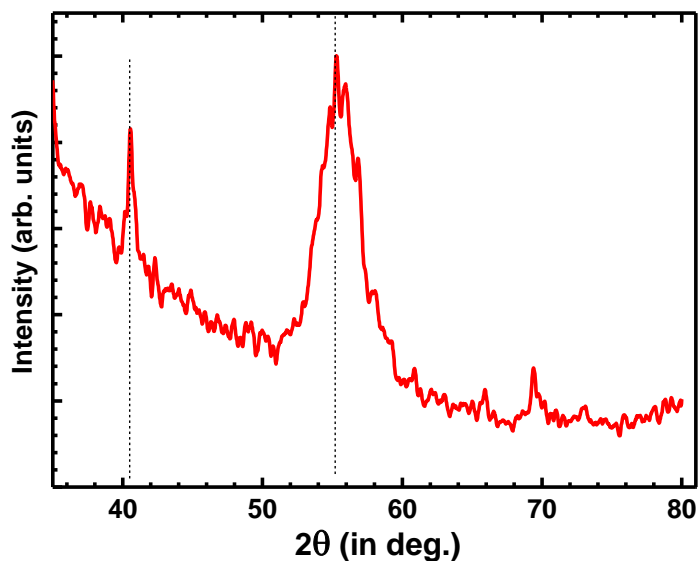


Figure 3-11 GIXRD spectrum of aluminum oxide thin film is shown. The vertical dotted line represents the peak positions of aluminum (Al) & aluminum oxide (Al_2O_3).

3.3.4.2 XPS analysis

To analysis the chemical composition of the film in-depth we have carried out X-ray Photoelectron spectroscopy (XPS) measurement for the as-deposited film as well as after sputtering the film for a time interval varying from 5 minutes to 25 minutes. Figure 3-12 shows the Al 2s, Al 2p and O 1s core levels XPS spectra of the aluminum oxide thin film after sputtering for a time interval of 10 minutes.

The high value of FWHM of Al 2s, 2p and O 1s core level spectra indicates the presence of more than one combined chemical composition of Al and O. The de-convolution of the XPS spectra corresponding to different core levels are carried out using XPS Peak fit software. The binding energy positions and the area of the different phases obtained from the de-convolution method

are tabulated in Table 3-3. The binding energy value of the various core levels as shown in

Figure 3-12 seems to be slightly shifted from the literature value as shown in dotted lines.

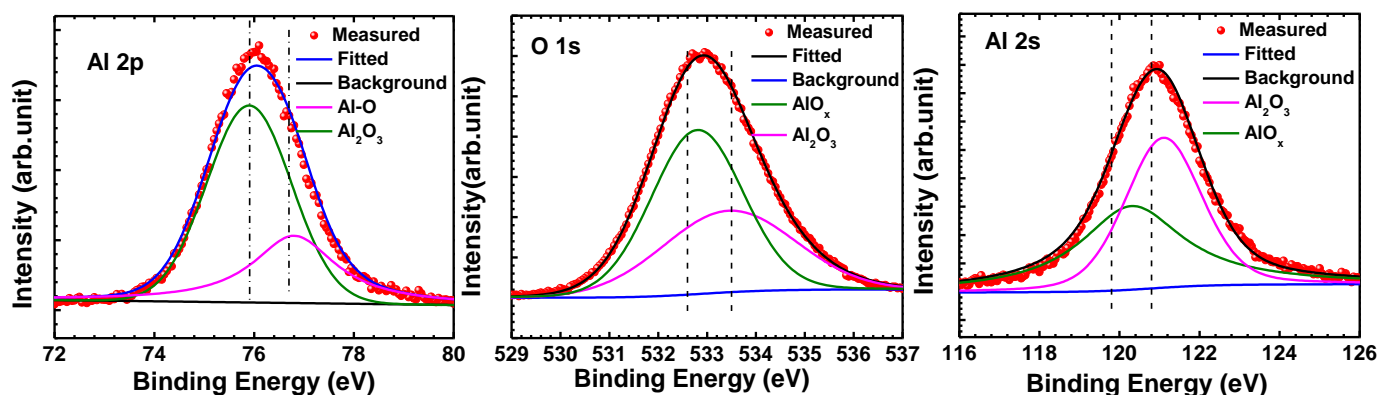


Figure 3-12 XPS spectra of Al2p, 2s & O 1s core levels of aluminum oxide thin film measured after sputtering for 10 minutes. Sputtering leads to removal of the top contamination layer.

Table 3-3. Elemental concentration for different sputtering cycle obtained from the XPS spectra of Al 2s and O 1s core levels

Etching time (min)	Al 2s			O 1s		Elemental Concentration	
	Binding energy (eV)	Phase	At%	Binding energy (eV)	At %	Al (%)	O (%)
5	120.3	AlO_x	52.47	532.8	66.76	31.057	68.943
	121.1	Al_2O_3	47.53	533.5	33.24		
10	120.3	AlO_x	50.24	532.8	58.96	31.81	68.19
	121.1	Al_2O_3	49.76	533.44	41.04		
15	120.4	AlO_x	44.19	532.8	55.84	32.49	67.51
	121.2	Al_2O_3	55.81	533.5	44.16		
20	120.45	AlO_x	44.7	532.84	53.28	32.65	67.35
	121.2	Al_2O_3	55.3	533.5	46.72		
25	120.4	AlO_x	28.75	532.81	33.9	44.11	55.89
	121.3	Al_2O_3	71.25	533.45	66.1		

It is also identified from the analysis of XPS spectra of various core-levels that two phases corresponding to AlO_x and Al_2O_3 are present in the film. Reference position of AlO_x and Al_2O_3 phases based on literature values obtained from NIST XPS database¹⁴² are marked as vertical dashed lines in the figures. From the analysis of area under the peaks the percentage

contribution of Al_2O_3 and AlO_x phases are calculated for different sputtering cycles for different core levels and are tabulated in the same table.

It is observed that upto 10 minutes sputtering cycle the percentage contribution of AlO_x is more or less stable around 50-52% but suddenly after 20 min the percentage contribution of AlO_x decreases whereas that of Al_2O_3 increases. This is so because huge percentage of the stoichiometric oxide deposited gets buried inside the film and the top layers mostly consists of AlO_x , however the oxidation may differ slightly.¹⁴³ The O/Al ratio as calculated from the peaks corresponding to Al_2O_3 phase is found to be 1.52. Similarly, the value of x is calculated from the ratio of the area corresponding to the AlO_x peak in O 1s and Al 2s core level and is found to be 1.97. These ratios are calculated by considering the area of the peaks of the corresponding phases at the O 1s and Al 2s/ Al 2p core level along with the contribution of the photoelectric cross section of the different core levels. The O/Al ratio for different sputtering cycles gives an idea about the approximate composition of the thin film at various depths. Though we have taken into account the photoelectric cross section of the different core levels, but other factors like mean free path of the electron for different energy range of the different core levels are not considered. Thus, this may result in an inaccuracy of the obtained stoichiometry results. However, carrying out the analysis for two different core levels of Al enhances the accuracy of the stoichiometry estimation using XPS technique. The primary limitation of this technique lies in its limited probing range of photoelectrons following its disability to probe the interfacial layer formed at the film/substrate interface. For the present case non-destructive soft X-ray reflectivity technique comes to the rescue.

3.3.4.3 In-depth compositional study using SXR analysis

We consider the optical constants profile obtained from the analysis of the angle-dependent soft X-ray reflectivity for the investigation of the composition of the principal layer. The disagreement of experimental profile with that of Al_2O_3 profile indicates about the absence of pure stoichiometric aluminum oxide as revealed from the XPS measurements also. The evaluation of the composition of the film is carried out by modelling the obtained experimental optical constants profile. To obtain a best fit for experimental optical constants profile the fractional composition of these two phases are considered. It is found that a contribution of 50% AlO_x ($x=1.6$) and Al_2O_3 gives the experimental profile a best fit. This exercise has been carried out for various $\text{AlO}_x + \text{Al}_2\text{O}_3$ combination where the value of x is varied from 1 to 2, but the best fit is found for $\text{AlO}_{1.6} + \text{Al}_2\text{O}_3$ combination. It is very important to assume a correct density of these two phases while calculating the optical index of these two phases. For this reason we have calculated the optical index of these phases assuming different possible densities ranging from 2.90 g/cc to the bulk density of Al_2O_3 i.e., 3.97 g/cc.

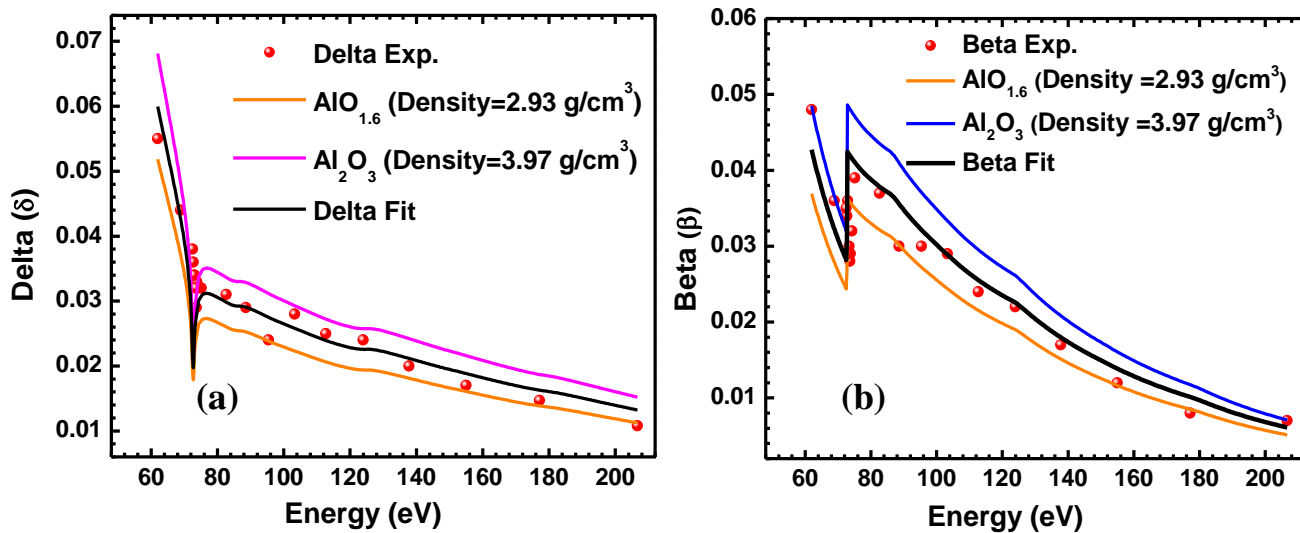


Figure 3-13 Optical index profile (a) δ and (b) β for AlO_x ($x=1.6$), Al_2O_3 are calculated for 2.93 g/cm³ and 3.97 g/cm³ density respectively and compared with experimentally measured profile of aluminum oxide thin film. The combination of 50% AlO_x ($x=1.6$) + 50% of Al_2O_3 gives best fit to the experimental data

The calculated profile of $\text{AlO}_{1.6}$ (high oxygen content) and Al_2O_3 along with experimental profile is shown in Figure 3-13 (a) and (b) respectively. From this figure it is evident that the experimental profile of the aluminum oxide thin film lies in between that of AlO_x ($x=1.6$) and Al_2O_3 profiles.

In next step we studied the compositional details of the interface formed at the aluminum oxide film/substrate interface using the optical index profile of interface layer. The evaluation of the optical index profile of the interface layer is carried out from the analysis of the angle-dependent reflectivity measurements. Generally, a silicon substrate has a 30-50 Å thick native oxide layer therefore we assumed that the interface layer could be of SiO_2 but the comparison of experimental optical index profile with that of SiO_2 do not have any resemblance. Further the Si substrate was RCA cleaned hence the possibility of pure SiO_2 layer is rather minimum.

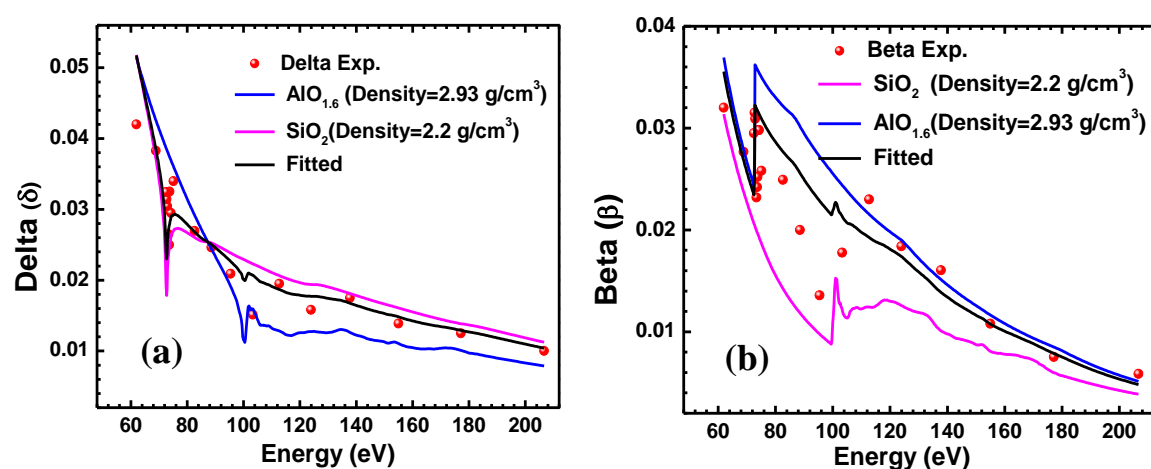


Figure 3-14 Optical index profile (a) δ and (b) β for interfacial layer formed at film/substrate interface. The experimental profile matches reasonably well with 25% SiO_2 and 75 % AlO_x ($x=1.6$) composition.

The most possible explanation behind the formation of an interfacial layer other than the native oxide can be understood from the film deposition process. It might have happened that while the sputtering of Al target in oxygen environment, the oxygen could react with Si substrate as well as with the sputtered Al atoms. In such a case it is possible that the silicon oxide and aluminum

oxide phases coexist in the initial stage of growth and then it is buried under the principal layer of aluminum oxide.

It is also likely that during the initial stage of deposition the Al can share two electrons with oxygen and another electron with the dangling bond of the Si substrate forming a Si-Al-O bonding.¹⁴⁴ Therefore in the interface region the formation of the AlO_x ($x=1.6$) phase along with silicon oxide is more probable.¹⁴⁵ All these fact has been considered in the optical modeling of the interface layer. The optical index profile of interface layer is therefore compared with that of SiO_2 and AlO_x ($x=1.6$) in Figure 3-14 (a) & (b) respectively. The fractional composition of 25% SiO_2 and 75% AlO_x ($x=1.6$) phase gives a best fit to the experimental profile of interface layer.

3.4 Conclusions

GIXRR results suggest that the film density is lower (2.93 g/cc) from that of bulk alumina (3.97 g/cc). The experimentally obtained δ & β are found to be 5-33% higher than the tabulated Henke's values for reduced density alumina of 2.93 g/cc. Near Al L- absorption edge, δ are 50-120% higher whereas β are lower by 7-20%. The variation in optical constant values are attributed to lower film density and mixed phases found in the present sample as revealed from the GIXRR and the XPS analyses. The optical constants of the film at discrete photon energy are also compared with the values available from other databases and that of fine spectra of α - Al_2O_3 . It is evident that for the thin film the beta (β) values are lower than that of α - Al_2O_3 , making it more suitable as a spacer layer in multilayers.

For α - Al_2O_3 well resolved peaks corresponding to the L_2 & L_3 absorption edge of Al are observed in both dispersion (δ) and absorption (β) which are located at an energy position of

78.0 eV & 78.4 eV respectively. These doublet feature are also termed as Al $L_{2,3}$ excitonic feature as cited in literature.

Compositional analysis of the principal layer as well as the interfacial layer of the aluminum oxide film was estimated quantitatively using the SXR technique. The best fit of the optical index profile of the principal layer over 60-200 Å (~206-60 eV energy) wavelength region was obtained by taking into account the composition of 50% AlO_x ($x=1.6$) and 50% Al_2O_3 . SXR analysis further reveals that the interface layer at the film/substrate region comprised of SiO_2 and AlO_x ($x=1.6$). The intermixing of these two leads to form an aluminum silicate compound at the interface region. The SXR technique gives compositional details of principal layer and interface region both in a non-destructive manner unlike the conventional XPS technique where one needs to sputter the film to obtain in-depth information.

Chapter 4.

Study on Structural and Optical Properties of MgO

This chapter deals with the investigation of optical properties in extreme ultraviolet (EUV)/ Soft X-ray region along with the characterization of surface and interface of MgO thin film deposited on Si substrate. The underlying physical aspects of the optical properties of MgO and its correlation with the electronic structure are investigated using energy-dependent reflectance spectroscopy. We utilized the energy-dependent reflectance data in order to extract the values of dispersion & absorption (optical constants) in 40-300 eV photon energy range covering the Mg L-edge (~50 eV). Interestingly, the effect of core hole on the optical properties of MgO is also shown.

For real application point of view we have also provided insights about the structural as well as surface and interface properties of MgO thin film using non-destructive EUV/SXR, Secondary Ion Mass Spectrometry (SIMS) and surface sensitive absorption (in total electron yield mode) techniques.

4.1 Introduction:

Magnesium oxide (MgO) is a versatile material that exhibits excellent dielectric property and has wide range of applications in various emerging fields of science and technology. It is used as a barrier layer in magnetic tunnel junctions.^{146,147} It is also regarded as one of the potential dielectric materials that has ample of applications in the semiconductor integrated devices. It is also well known for its use as a substrate in depositing high quality oxide films.¹⁴⁸ The utility of Magnesium oxide (MgO) thin film for various EUV/Soft X-ray optics applications are already discussed in Chapter 1. The scientific desire to obtain a fundamental understanding on the structural and optical properties of the thin film in the soft X-ray/ VUV region for applications in the field of multilayer mirror is an important requirement and is emphasized in Chapter 1. There we have also discussed about the relation between the optical properties with the electronic structure of a material.

Very few studies are available which provide unprecedented insight into the connection between the optical properties with the electronic structures.^{149,150,151,152} Among them most of the studies are based on the optical properties in the IR and visible region of the electromagnetic spectrum which lies below the band gap energy of semiconductor or insulator materials. Studies on the correlation between electronic structure & optical properties in the EUV/ Soft X-ray region covering the core-level absorption edges of the constituent elements of compound materials are scarce.^{153,154} Recent progress in the instrumentation of the beamlines using synchrotron radiation sources enables one to map the optical properties of materials with respect to the modification in the electronic structures.^{155,156} In the introduction of Chapter 3, we have provided references of few possible materials like Al₂O₃, MgO & SiO₂, where the influence of core-hole effect on the absorption spectrum near the edge region of cation is observed. In the same chapter itself, we

have also shown how the optical properties are dependent on the crystalline state, electronic structure & composition in case of aluminum oxide. There are several other oxide materials like TiO_2 , CaO ¹⁵⁷ and minor actinide dioxides like NpO_2 & AmO_2 ¹⁵⁸ in which this effect is observed from theoretical calculations and are reported. Calandra et al.¹⁵⁹ reported that shakeup processes occur at the K-edge XAS spectra of NiO , CoO , and CuO . According to their study, charge-transfer satellites occurring in X-ray Photoelectron core-hole spectra gives rise to shakeup satellites in the corresponding X-ray absorption (XAS) spectra.

In EUV/ Soft X-ray region there is no satisfactory understanding achieved so far, on extracting optical constants in the near edge region of strong ionic-insulators having strong core-hole effects. In this endeavor a joint experiment-theory effort using synchrotron radiation source and a computer time-space effective first principles method is the main aim of this Chapter.

Reflection spectroscopy performed in EUV and soft X-ray region close to the absorption edges of constituent elements serve as a powerful tool to probe optical constants in this energy region. Near the absorption edges, the response functions are being perturbed leading to additional fine features corresponding to the local atomic and electronic structures. These features are similar to that observed in near edge X-ray absorption spectroscopy results.¹⁶⁰ However, these results represent absorption features, while there is no direct way to estimate the dispersion features. One can use conventional Kramers-Kronig relation on the obtained absorption spectrum to derive the dispersion curve. Similarly, from the energy dependent reflectivity spectrum one can estimate both the optical constants simultaneously using Kramers-Krönig (KK) relation where several fine features near the edges along with small shifts may appear. These fine features account for core excitations and different bonding configurations associated with electronic

structure respectively. Once we understand the origin of these fine features we can easily correlate the relation of the electronic structure with that of the optical properties.

In literature, although electron energy loss spectroscopy (EELS) and X-ray absorption spectroscopy (XAS) measurements of MgO are available, no reports of optical constants above the photon energy of 29 eV is available. Previously, ref.¹⁶¹ obtained the optical constants of MgO for the energy range of 4-29 eV, by Kramers-Kronig analysis of their reflectance data. Brien et al.¹³⁷ also carried out soft X-ray reflection spectroscopy measurements in the energy range of 50-85 eV. However, the prime inadequacy of their work was that, they measured relative reflection, not the absolute one. In this way, their information failed to provide information about optical constants of MgO.

Optical constants are highly dependent upon the structural details of the thin film which is again dependent upon its deposition technique. The advancement in thin film deposition techniques enables one to fabricate high precise low thickness film (~ nm) along with spatial uniformity. However, the nature of interaction of the deposited film on the substrate is not always known. Sometimes interface formation due to inter-diffusion, formation of rough surfaces, presence of buried layer may deteriorate the quality of the deposited film resulting in the degradation of its performance. Thus, it is a prerequisite to carry out proper material characterization i.e. determination of structural parameters with high accuracy, in-depth density profile, surface and interface composition of the film along with its optical constants. Soft X-ray reflectivity and soft X-ray absorption spectroscopy are powerful techniques used to investigate the surface, interface and the structural characterization of a material as discussed in Chapter 1.

There are several instances in literature where SXR-TEY techniques are used to successfully describe the interfaces buried deep down the surface. Borrero et al.¹⁶² carried out site selective

spectroscopy of transition metal oxide (LaCaMnO₃/YBCO) heterostructures using reflectivity and X-ray absorption spectroscopy. Filatova et al.¹⁶³ have shown the evolution of near edge absorption fine structure of HfO₂ thin film using simultaneous TEY and X-ray reflection spectroscopy technique. Alders et al.¹⁶⁴ also carried out grazing incidence reflectivity and absorption spectroscopy of NiO near Ni 2p edge. In this work we have carried out a detailed characterization of surface/ interface quality of MgO thin film using soft X-ray reflectivity and soft X-ray absorption spectroscopy. However, in order to achieve the calculated performance from a thin film/ multilayer devices it is prerequisite to characterize the surfaces/ interfaces quality in actual energy/wavelength regime. Studies on soft X-ray behavior of MgO thin film are scarce in literature, which motivates us to understand the soft X-ray optical behavior.

In the present study, we present experimentally obtained optical constants of magnesium oxide (MgO) thin film in 40 - 300 eV energy range (~300-40 Å) covering the complete soft X-ray region available in the reflectivity beamline of Indus-1 synchrotron radiation source. To the best of our knowledge, ours is the first experimental study which covers optical constants of MgO thin film in wide energy range of 40-300 eV, where various fine features observed in the absorption spectra near the Mg L edge are explained using first principles density functional calculations. The measured optical constants indicating the presence of fine features near the Mg L edge region are compared with the Henke's tabulated values obtained from the CXRO website. Henke data available from the CXRO website does not explain the effects of core-hole on the optical constants of MgO near the Mg absorption edge region. Whereas, our results give clear evidence of effect of core-hole on the MgO optical constants which has been confirmed by theoretical calculations carried under the framework of density functional theory. We have also carried out angle-dependent soft X-ray reflectivity measurements of MgO thin film deposited

over Si substrate over the wavelength range of 120-190 Å. From the analysis of the soft X-ray reflectivity data the in-depth delta profile is obtained, which gives a clear picture of the density variation of the surface and interface below and above Si L-edge (~125 Å). The model, as assumed for the analysis of the soft X-ray reflectivity data is correlated with the secondary ion mass spectra. On the other hand, the X-ray absorption measurements (XAS) in total electron yield mode were carried out near the O K-edge providing information about the top surface layer and the structure of the film.

4.2 Core-hole effect and its implication on electronic structure

When a photon having an energy equivalent to the Mg L-edge energy gets impinged on MgO thin film sample, formation of core-hole at Mg L shell occurs as a result of knocking out of an electron. After the formation of the core hole, it may be screened by the surrounding electron cloud present in the system leading to the formation of bound exciton like states. The main principle behind the formation of these states can be attributed to the Coulomb interaction between the excited electron and the core hole formed. Since these states are localized deep within the atomic cores and are incapable of hopping from one atomic site to another, these can be named as core-exciton states. The electron associated with a core exciton faces an excess strong potential of the core-hole as a result of which an observable change in the electronic structure near the vicinity of the absorption edge can be noticed. However, the strength of the core-exciton effects may vary from system to system (e.g; semiconductor, insulators). The degree of the effect primarily depends on the response of the remaining electrons in the solid that attempt to screen the core hole from the high-energy unoccupied states. Thus, in case of insulators the core-hole effect plays a key role in the modifications of the electronic structures near the vicinity of the absorption edges as compared to metals and

semiconductors. There are ample of literatures showing the core-exciton features in the absorption spectrum, especially near the edge region.^{165,166,126} The theory of the absorption spectrum is based on the famous principle of quantum mechanics- the Fermi Golden rule, where two factors such as, site and symmetry projected density of states and the transition matrix elements play the major role. However, the origin of the features corresponding to the core-hole effect can't be completely interpreted from these two terms. In order to understand this, we present a schematic understanding of the core-hole or equivalently core-excitonic effect in our case shown in Figure 4-1.

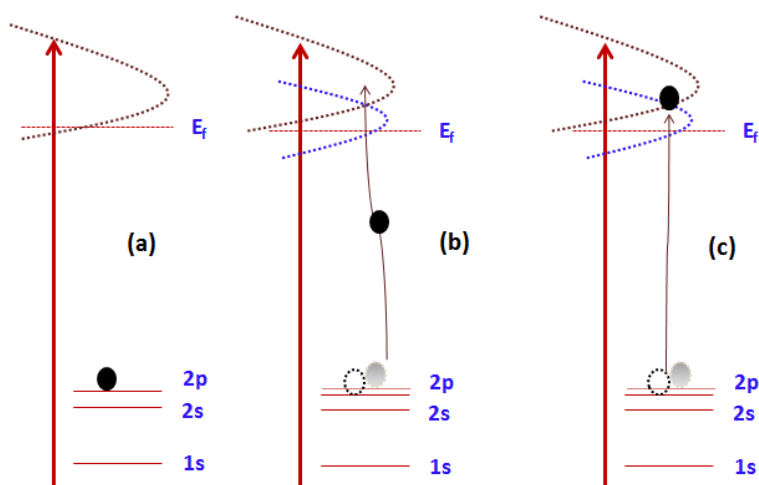


Figure 4-1 Schematic representation of the formation of core-exciton state as a consequence of core-hole effect (a) shows the ground state of MgO (b) shows the transition state where formation of core-exciton state occurs & (c) shows the final effect of core-hole.

The figure at the left shows the ground state (or initial state) - with the electron of the 2p state being excited by the X-ray photon. The middle figure shows that an electron making a transition to the unoccupied valence states are pulled down in energy due to the presence of the hole in the 2p state. The curve on the right is the spectrum in the final state with a hole in the 2p and a photoelectron in the valence band shifted down in energy due to the attractive core hole.

In reality, the probing electron (in case of EELS) or X-ray photon (in case of photon spectroscopy) interacts with the sample under study that has already been perturbed by the probe. This perturbation results in the removal of an inner shell electron or generation of a core-hole. After the generation of the core hole, the relaxation of the system also occurs simultaneously. This phenomenon is replicated in the experimental spectrum. Thus, proper explanation of the experimental absorption spectra near the edge region especially for oxides is a challenging task since it involves the contribution of many other effects which are explained below.

The core-hole formed owing to the ejection of the photoelectron remains localized on a particular atomic site. Thus, of the most popular approach adopted by researchers of DFT community is to introduce a core hole i.e., to reduce the electron occupation in the core level and simultaneously apply supercell approximation. Another way to confirm the origin of the different features appearing in the experimental absorption spectra is to simultaneously perform ground state XANES calculation.

4.3 Experimental details

The magnesium oxide films were deposited by ion-beam sputtering (IBS) technique. The ion source used produces an ion beam of desired gas of Argon, Nitrogen and Oxygen. The ion source has a diameter 30 mm with energy lying in the range of 200-1200 eV and beam current lies within 20-100 mA. The ion source uses RF to ignite plasma and a RF electron source to neutralize the ion beam. This enables the IBS system to sputter both conducting as well as insulating materials. Other details of the system can be found in¹⁶⁷. Before the deposition, the Si substrate was ultrasonically cleaned with acetone. The sputtering of pure MgO target (99.99% purity) was carried out in an argon (Ar) environment at a working pressure of 2×10^{-3} Pa. The

target was sputtered with an argon ion beam having energy of 1000 V and a beam current of 30 mA. With MgO being an insulator, to avoid the sample charging effect a neutralizer was flown at a rate of 5 sccm while deposition. Prior to the deposition, the chamber was maintained at a base pressure of 4.2×10^{-5} Pa.

Reflectivity measurements were performed at reflectivity beamline of Indus-1 synchrotron radiation source with the use of two mirror harmonic suppressor system. Details are given in Section 0.

Depth profiling using Secondary Ion Mass Spectrometry (SIMS) was carried out on magnesium oxide (MgO) sample deposited on Si substrate. The primary beam consists on Cs^+ ion bombarded with energy of 1 keV and a current of 80 nA on an area of $300 \mu\text{m} \times 300 \mu\text{m}$ of sample surface. The analysis was carried using bismuth ion (Bi^+) at energy of 300 keV and a current of 4.7 pA on an area of $100 \mu\text{m} \times 100 \mu\text{m}$ on the crater.

4.4 Results and discussions:

4.4.1 Surface/ Interface study of Magnesium oxide thin film

Angle dependent Soft X-ray reflectivity measurements were carried out in the wavelength region of 120-190 Å to investigate the structural parameters and the layer model of the thin film. Figure 4-2 shows the measured (star) and fitted (black solid line) angle-dependent reflectivity curves of 500 Å thick magnesium oxide (MgO) thin film using photon beam in the 120 Å to 190 Å wavelength range. In order to obtain a best fit, it is found that a simple three layer model consisting of the top surface layer, principal MgO layer and the interfacial layer consisting of native oxide of the substrate is not sufficient to fit the measured data. To improve

the fit quality an additional layer near the film/substrate interface is assumed after the native oxide layer on the substrate.

The model which gives a best fit consists of the top surface layer, the principal MgO layer, an interfacial layer consisting of Mg-Si compound and the native oxide layer on the silicon substrate. From the analysis of the reflectivity data, the structural parameters i.e., thicknesses and roughness of each layer comprising the film was evaluated along with their corresponding delta (δ) variation with thickness. The structural parameters i.e., thicknesses and roughness of the different layers as obtained from the SXR analysis are tabulated in Table 4-1.

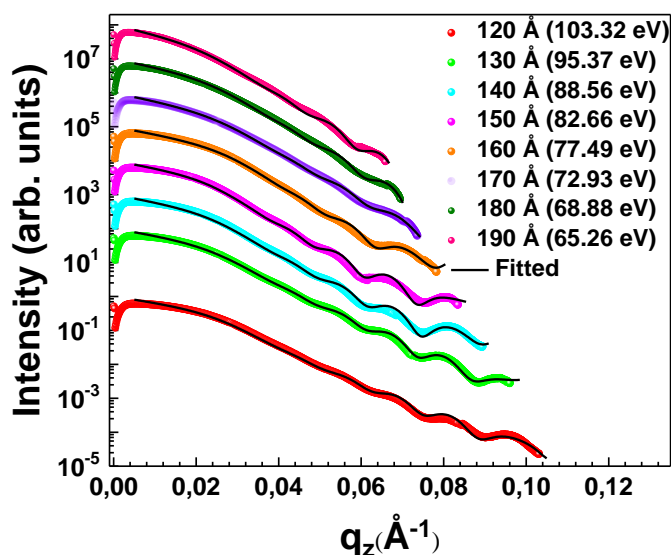


Figure 4-2 Measured (star) and fitted (continuous solid line) angle dependent soft X-ray reflectivity curve of magnesium oxide (MgO) thin film over the wavelength range of 120-190 Å.

The structural parameters obtained were valid over the complete region of wavelength (120-190 Å) where reflectivity measurements were performed.

From the delta (δ) values of the top surface and principal layer MgO layer it was found that the delta (δ) of the top surface layer is ~33% less than that of principal layer. The layer model as

considered for analysis of reflectivity data was confirmed from secondary ion mass spectrometry (SIMS) measurements too. Our SIMS data as shown in Figure 4-3 also suggests that the surface layer is comprised of MgO, and its low density could be due to surface roughness and presence of unreacted oxygen etc. as evident from reflectivity analysis.

Table 4-1 Structural parameter of the magnesium oxide thin film obtained from angle-dependent SXR.

Layer	Thickness (Å)	Roughness σ (Å)
Top surface	35±0.6	9.3
Principal MgO	434±0.7	9.2
Interface	47±0.8	7.9
	40±0.8	3.6
Si substrate	INF	3.3

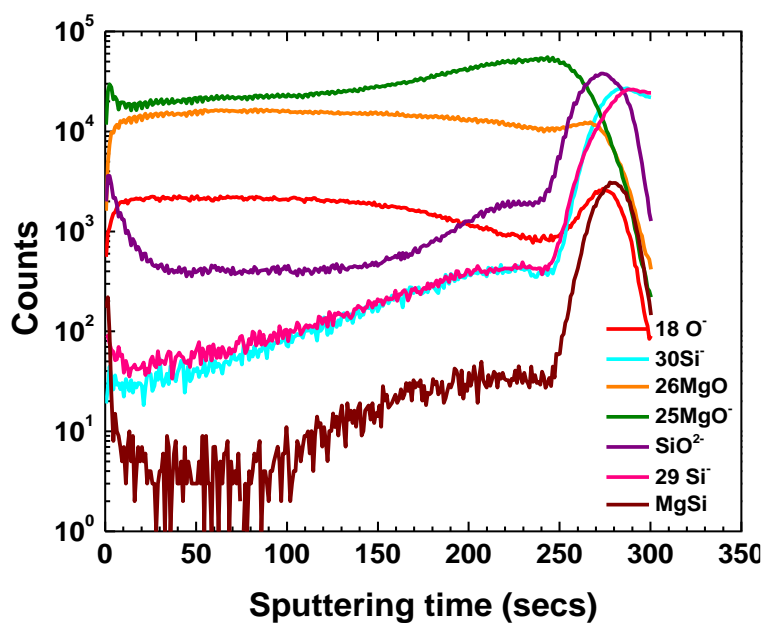


Figure 4-3 Secondary ion mass spectrometry (SIMS) spectra of magnesium oxide (MgO) thin film.

The in-depth composition of the magnesium oxide thin film can be well understood from the optical density (δ) profile obtained by modelling the reflectivity data over the wavelength range of 120 to 190 Å and is shown in Figure 4-4. The optical density profile (ODP) as obtained

from SXR analysis ensures the fact that the top layer has low density in comparison to the principal MgO layer. It is also evident that the principal layer is almost uniform except near the air/film and the film/substrate interface. The effect of surface roughness is included in the calculation of in-depth ODP as evident in Figure 4-4, where a gradual change in density (δ) is observed between the interfaces of various layers as assumed in the model. The surface roughness effect is considered in accordance to the Névot-Croce model where an error function instead of a step function is assumed near the interface of different layers. Near the film/substrate interface, formation of some interfacial layer is observed. Previously, Singh et al.¹⁶⁸ carried out X-ray reflectivity measurements of Fe/MgO/Fe multilayer stack where MgO buffer layer was deposited on Si substrate to prevent silicide formation at the Si/Fe interface. They observed that the obtained reflectivity pattern matched well with the simulated one on consideration of a SiO_x and Mg_2Si_x layer above the Si substrate.

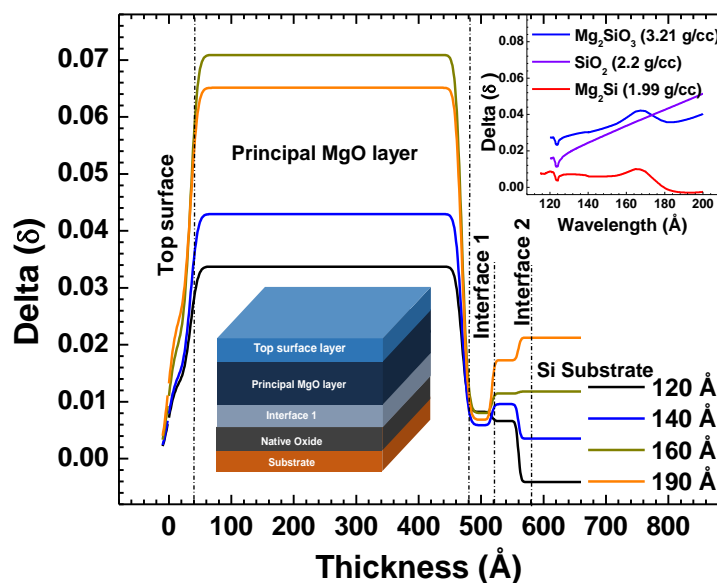


Figure 4-4 In-depth optical density profile obtained from modelling the soft X-ray reflectivity data. Inset shows the Henke tabulated delta values in the wavelength range of 120-190 Å for bulk Mg_2SiO_3 , SiO_2 , and Mg_2Si .

In our study also we have considered two layers of different densities between the principal MgO and Si substrate. To identify the composition of this interface layer we tried to make a comparison between the Henke tabulated-delta values of bulk Mg_2SiO_3 , Mg_2Si and SiO_2 .

For 120 Å, the in-depth delta profile shows that the interfacial layer is actually composed of two different layers having a slight contrast in delta i.e. having slightly different densities. The two interfacial layers are nothing but Mg-Si-O and Si-O layers. At 120 Å, the delta value of the 1st interfacial layer is slightly higher than that of the 2nd one, while at 140 Å this trend reverses. This is evident from the inset of Figure 4-4, where we can see that the delta value of bulk SiO_2 lies between that of Mg_2SiO_3 having a bulk density of 3.21 g/cc and Mg_2Si with a density of 1.99 g/ c.c. If we consider that the 1st interfacial layer is composed of Mg-Si-O then its delta value must lie somewhere between the delta profile of bulk Mg_2SiO_3 and Mg_2Si , which is true for our case. Moreover, according to the trend of the delta profile of bulk SiO_2 , it is quite evident that the delta value at 140 Å for Si-O must be higher as compared to Mg-Si-O. It is also evident that after 170 Å, the delta value of the Mg-Si-O layer is quite lower than the Si-O layer. If we observe the inset of Figure 4-4, we can see that delta value of both bulk Mg_2SiO_3 and Mg_2Si follows a decreasing trend as wavelength increases after 170 Å. To confirm the correct picture of the model obtained by analysis of the soft X-ray reflectivity we have carried out secondary mass ion spectroscopy (SIMS) measurements. SIMS being a destructive technique provides the real picture of the in-depth composition of the thin film. Figure 4-3 shows the SIMS spectra of the magnesium oxide thin film, where it is observed that the principal MgO layer is almost uniform throughout the depth of the film except at the film/substrate interface. Near the interface, presence of both SiO_2 - and Mg-Si is evident. It is evident from the spectra that the Si atoms from the substrate diffused towards the principal MgO layer upto some extent. The Si

atoms along with MgO form a complex Mg-Si-O compound. Thus the SIMS results corroborates well with the optical density profile (ODP) obtained by modelling the soft X-ray reflectivity data.

4.4.2 Investigation of optical constants of MgO thin film and its relation to electronic structure

4.4.2.1 Investigation of optical constants near Mg L-edge from energy-dependent SXR measurement.

Figure 4-5 shows the energy-dependent reflectance spectra in the 40-300 eV range for a fixed incident angle of 5° .

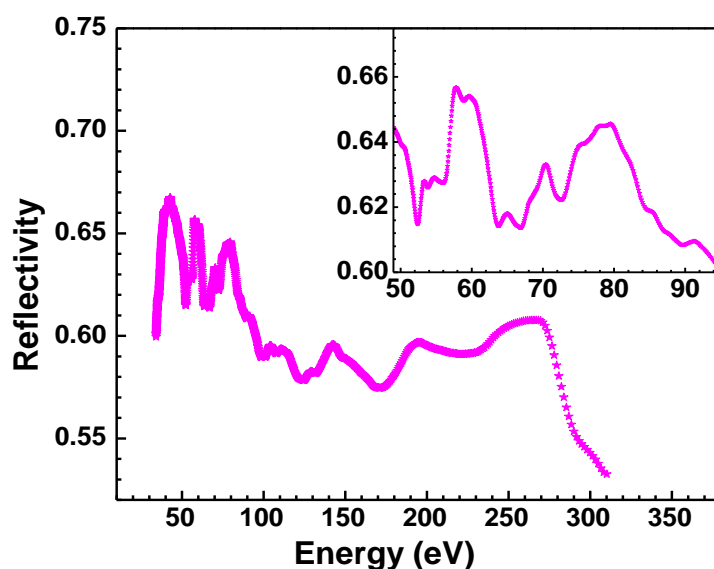


Figure 4-5 Measured reflectance spectrum of an MgO thin film at a fixed glancing angle of $\theta = 5^\circ$ in the energy range 40–300 eV. The inset shows thereflectance spectra neat the Mg L-edge.

To perform Kramers-Kronig integration we need reflectivity data over broader energy range (zero to infinity), thus to satisfy this condition we have stitched our experimental data of 40-300 eV range with the simulated reflectivity data of 300 to 30,000 eV range. Finally the phase of the

reflected wave field was retrieved using the Kramers-Kronig relation as shown in Equation (1-10).

Figure 4-6 (a) and (b) shows the optical constants (δ & β) of MgO thin film obtained by applying KK relation. The obtained optical constants over the continuous spectral range of 40-300 eV are compared with the only optical constants available from the CXRO website. The present study of optical constants measurements of MgO thin film in 40-300 eV photon energy range has two different regions 1) Near Mg L absorption edge, 40-100 eV (as shown in inset of Figure 4-6 (a) and (b)) and (2) Away from absorption edge, 100-300 eV. It is evident that the fine features are observed in the first region i.e. 40-100 eV. On the other hand, no distinct features are observed in 100-300 eV range. The features as observed in the profile of optical constants near the Mg L absorption edge region are completely different from the features appearing in the Henke tabulated values. The calculation of penetration depth suggests that the photons of 40-100 eV

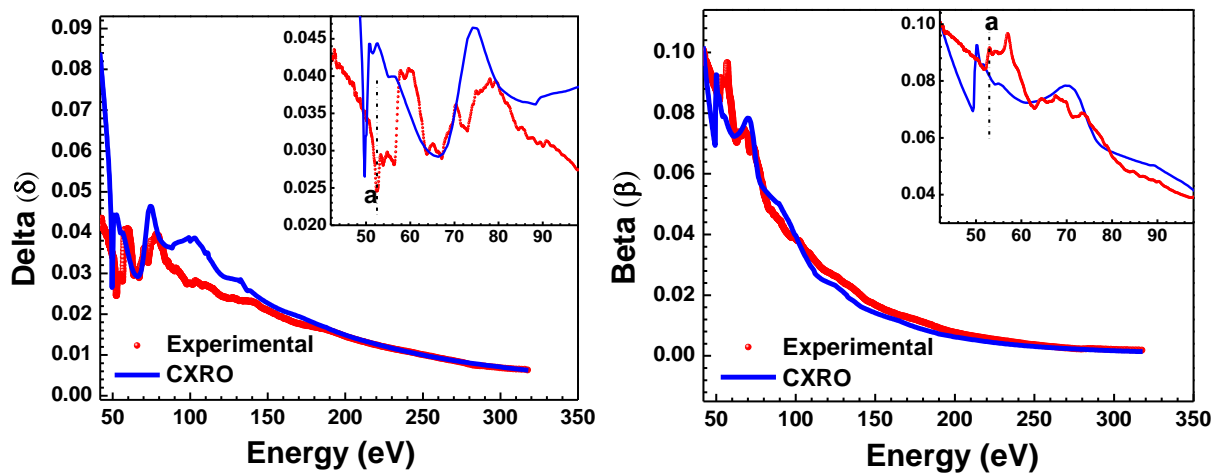


Figure 4-6 Measured values of (a) delta (δ) and (b) beta (β) obtained from the KK analysis of reflectivity versus photon energy data are compared with tabulated values obtained from the CXRO database. The inset shows the 40–100 eV region where several fine features are evident.

penetrate a thickness of more than 5.0 nm and thus they interact with principal MgO layer. This suggests that the fine features as observed in the 40-100 eV energy range are correlated with

principal MgO layer. On the other hand in the 100-300 eV energy region, the penetration depth lie within a thickness of 3.0-4.5 nm, thus representing the optical constants of low density MgO surface layer. From the inset of Figure 4-6 (a) and (b) it is also evident that the energy position of the feature marked 'a' as determined from the experimental reflectance spectra lies at 52.8 eV which is almost consistent with ref.¹³⁷. On the other hand, according to Henke tabulated optical constant profile obtained from CXRO database, the Mg L-edge is located at an energy value of 49.6 eV, which actually corresponds to that of pure Mg. This shift could be well understood as the Henke tabulated data are calculated using the weighted sum method and near the absorption edge region the weighted sum approach fails. For example, Mg and O atoms forms an ionic bond and resultant overlapping of atomic wave functions lead to formation of new molecular wave function for compound MgO. In the weighted sum approach, the role of this overlapping wave function is not accounted and therefore the edge energy of the tabulated data corresponds to that of Mg.

4.4.2.2 Investigation of optical constants near O K-edge from X-ray absorption measurement.

It is well known that the total electron yield (TEY) spectrum measured in normal incidence mode is proportional to the absorption co-efficient or the beta (β) spectrum. The limitation of Henke tabulated database is that it lacks the details of the fine features near the absorption edge region. However, far away from the edge region it provides accurate information about the optical constants. Thus, if we record total electron yield spectrum over a larger energy range (~50 eV from both sides of the edge region) and scale with respect to the Henke tabulated beta (β) values away from the edge region to match, we obtain the beta spectrum with all the possible fine features. Figure 4-7 shows the X-ray absorption spectrum of the 500 Å thick MgO thin film

measured in total electron yield mode scaled with respect to the Henke tabulated beta (β) values taken from CXRO database.

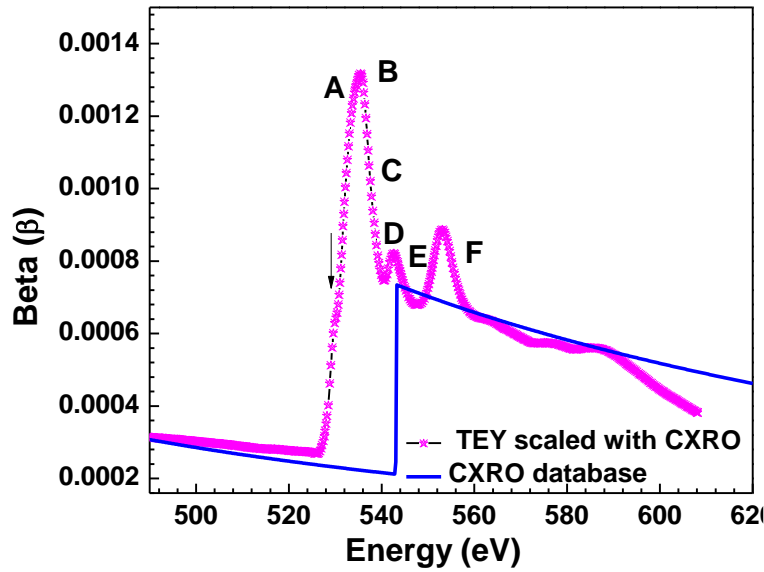


Figure 4-7 Experimental X-ray absorption spectra of MgO thin film measured near O K-edge in total electron yield mode scaled with respect to the Henke tabulated beta values taken from CXRO database.

In the next step we have used the Kramers-Kronig (KK) relation for the extraction of the dispersion part, delta (δ) from the scaled total electron yield spectrum representing beta (β). The KK relation used in this case is given in Equation (1-12). It is evident that the integration limit of energy in the above KK relation extends from zero to infinity, while our measured experimental range is limited. Thus, to avoid the truncation error in the evaluation of delta (δ) we have stitched our experimental beta spectrum with the Henke tabulated beta values from the energy range of 40 eV to 10000 eV.

The obtained delta spectrum in the energy range of 480-600 eV covering O K-edge is compared with that of the Henke tabulated value taken from CXRO database. It is evident that away from the edge region the deviation between the experimental beta (β) values with respect to the tabulated one decrease, which is quite obvious. At the O K-edge region deviation between

experimental beta (β) values with respect to the tabulated one is higher and the edge position is found to be shifted by 11.5 eV with respect to Henke.

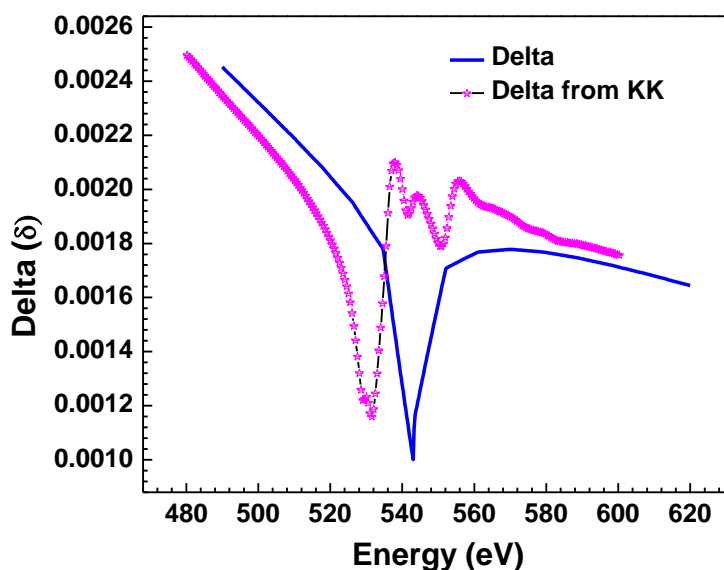


Figure 4-8 Measured values of delta (δ) obtained from the KK analysis of beta (β) values as obtained by scaling of total electron yield spectra with respect to Henke tabulated data. Comparison of the measured delta (δ) values with the Henke data available in CXRO database is also shown.

This shift could be well understood as the Henke tabulated data are calculated using the weighted sum method and near the absorption edge region the weighted sum approach fails due to Mg-O bonding resulting in chemical shift.

The origin of the fine features appearing near the O K-edge in both the dispersion (δ) & absorption (β) spectra will be discussed in the next section.

4.4.2.3 Relation between electronic structure & the investigated optical constants.

To correlate the optical constants near the Mg L-edge & O K-edge with the electronic structure of MgO thin film it is necessary to understand the origin of the various transitions which lead to the appearance of several fine features near the edge region. In our experimental results, some fine features are observed in the optical constants spectrum near the Mg L edge region as well as

O K-edge region. From few of evidences in literature we assume that the appearance of some fine features can be accounted to the creation of an excitonic like state as a consequence of core-hole effect. In case of MgO, the exciton is created in the band edge and it is due to the transition $2p^6 \rightarrow 2p^5 3s^1$ in the cation site.¹³⁷ The excitonic like state formed leads to the modification in the oscillator strength for transitions at higher energies.¹⁶⁵ The creation of the core exciton state as a result of the core-hole effect can be referred to as a modification in the electronic structure which is reflected in the optical constants profile of MgO. In order to ensure the fact that the fine features arises as a result of the presence of core-hole effects, it is necessary to provide theoretical evidences.

DFT calculations

There are several instances in literature where core level spectrum calculations have been carried out using different methods based under the framework of DFT. The accuracy of most of these calculations depend on the choice of correct pseudopotentials which takes into account the effect of the electron hole interaction of an excitonic like state. Ref ¹⁶⁹ studied the influence of supercell size on calculated absorption spectra of MgO using the conventional Z+1 approximation. They have also generated pseudopotentials for excited states, for Mg, both with a large core (1s, 2s, 2p orbitals) and a small core (1s orbital only). The corresponding calculations were found to have a very good agreement with the results from the Z+1 calculation for the Mg-K edge only. Ref¹⁷⁰ carried out calculations of Mg-K edge absorption spectra of MgO using WIEN2k employing a supercell. In their approach, the calculations were carried out by removing one core electron and adding it as uniform background charge to avoid renormalization. References ^{165, 166}, investigated the near edge structure of the Mg L_{2,3} edge of MgO under the framework of Bethe-Salpeter Equation (BSE) within two-particle method. The

Bethe-Salpeter Equation (BSE) takes into account the effect of electron-hole interaction in a rigorous manner and thus provides more accurate results. However, absorption calculation using this equation is very cumbersome requiring higher computational cost.

In this study, we have reproduced the fine features appearing in the optical constant spectra near the Mg L absorption edge using first principles calculations in CASTEP. Gao et al.¹⁷¹ carried out calculation of absorption spectra of MgO using CASTEP; however their study was focused on Mg-K absorption edge only. While performing our calculations we have considered MgO to have a rocksalt cubic structure, similar to that of a single crystal MgO, and the comparison were made with the experimental absorption spectra of MgO thin film. In order to support our stand to compare optical constants results with single crystal MgO, we have carried out total electron yield (TEY) measurements on both MgO thin film and substrate (single crystal) near O-K edge region as shown in Figure 4-9. From the TEY results, it was confirmed that the MgO thin film has similar rocksalt structure as that of a single crystal.

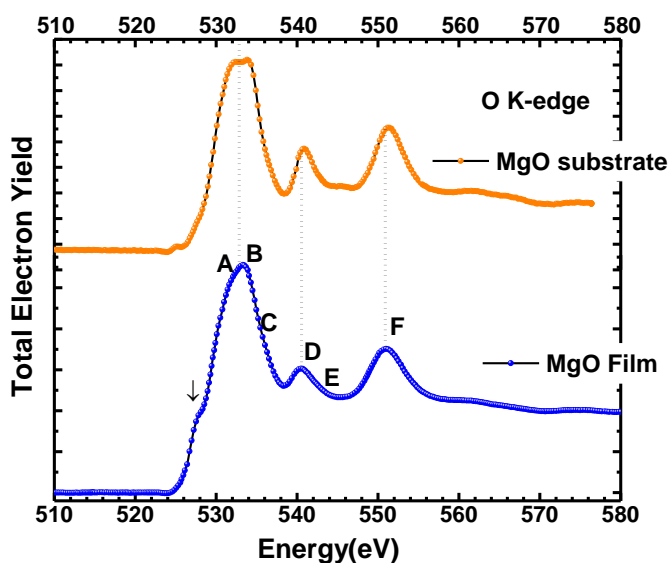


Figure 4-9 X-ray absorption spectra of 500-Å-thick MgO thin film and that of a MgO substrate measured in total electron yield mode near the O-K absorption edge region.

To study core level spectroscopy using CASTEP, $3 \times 3 \times 3$ supercell is used. In our approach both the advantages of reduced computational cost, the ability to study very large systems and the accuracy of all-electron methods are retained. This is in contrast to the methods like BSE as mentioned above. Calculations with core hole are designed to describe the electronic structure of MgO containing highly excited ion with a hole in Mg-L core shell. Such calculations are relevant to the description of excitation and relaxation of these excited states. The calculations are carried out in two modes: without core-hole and considering a core-hole on an Mg atom. Figure 4-10 demonstrates the detailed comparison of the experimental spectra with the calculated one. The spectrum with legend named 'Experimental' in Figure 4-10 represents the variation of the optical constant beta (β) with respect to energy near the Mg L edge. The features appearing in the spectrum are marked from 'a' to 'g'. The calculated spectrum considering core-hole effect matches very well with the experimental one in terms of the location of the features which are marked as 'a' to 'g'.

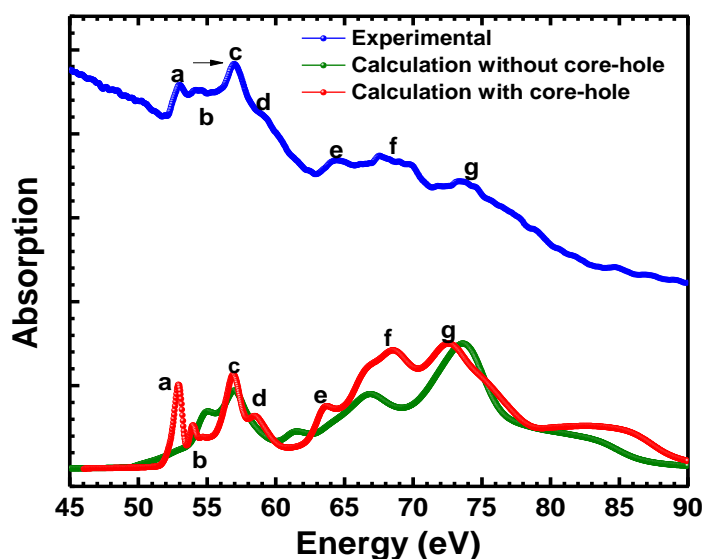


Figure 4-10 Experimental absorption spectra of MgO near the Mg $L_{2,3}$ -edge shown along with the theoretical spectra. The experimental spectra match well with the theoretical spectra obtained by considering the core-hole effect.

However, differences in terms of strength of the features in the experimental and the calculated spectrum are observed. The reason behind the differences in the experimental and the calculated spectrum can be attributed to the consideration of a single crystal like periodic system instead of the polycrystalline nature of the thin film where presence of defects and impurities are quite expected. We have considered the width of the core-hole to be 0.25 eV in order to match with the experimental spectrum. The effect of core-hole is self-evident as one compares the absorption spectra in absence and presence of core-hole effect. On comparison of the 'Experimental' and the 'calculated spectrum considering core-hole' it is clear that the features marked as 'a' and 'b' originate as a consequence of the core hole effect.

A detailed study on the various angular momentum projected partial density of states (PDOS) of MgO as shown in Figure 4-11 may provide significant light on this. However, it is not possible to justify the origin of every absorption features marked from 'a' to 'g' from the calculated angular momentum projected density of states in absence or presence of core hole. Below the Fermi energy level, the negative energy states represent the occupied energy states while the positive energy states are the unoccupied ones.

Thus from the calculated PDOS one can conclude that the absorption features of the experimental spectrum in Figure 4-10 root from the transition of Mg p to Mg s, d and hybridized states of Mg s and O s states respectively.¹²¹ Features 'c' and 'd' originate due to the transition from Mg 2p to the hybridized Mg and O states respectively. Higher energy absorption features marked from 'e' to 'g' appears as a result of transitions to Mg 3d states. While the origin of the features marked as 'a' and 'b' could be explained from the calculated PDOS in absence of core-hole. Thus, it is ensured that these two features appear as a consequence of the core-hole.

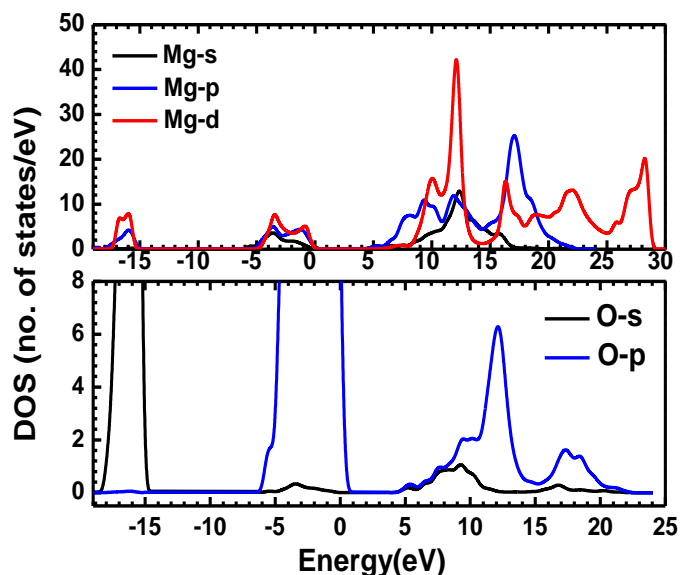


Figure 4-11 Calculated partial density of states (PDOS) of MgO in the absence of a core-hole.

Now, we will discuss about the features appearing in the optical constants spectra near the O K-edge of MgO. Here we observe 5 features which are designated as A, B, C, D, E and F as shown in Figure 4-7 and Figure 4-9. The three features named as A, B and C arises due to Oxygen p states to hybridized states of Mg 1s and Mg 2s states, where 1 and 2 stands for first and second nearest neighbors of Mg atoms respectively. The feature D is due to strong anti-bonding interaction with Mg p orbitals and the feature E and higher energy features are mainly due to Oxygen p to hybridized states of Mg 1d anti-bonding interactions.¹⁷² One of the features shown by arrow in the spectra could be due to core-exciton which generally expected to appear in the vicinity of the absorption edge.

4.4.2.4 Checking the accuracy of the optical constants of MgO thin film.

To check the accuracy of the obtained optical constants we have simulated the reflectivity spectrum for different angle of incidence and compared with the experimental one. For

simulation we have used the structural parameters i.e. the thickness & roughness of the different layers of the film along with the investigated optical constants.

On comparison of the simulated reflectivity spectra using the investigated optical constants with the measured one, we find that towards higher energy side a deviation of around 1-2% is present whereas in the 40-100 eV region a deviation of 0.4-1.0% prevails.

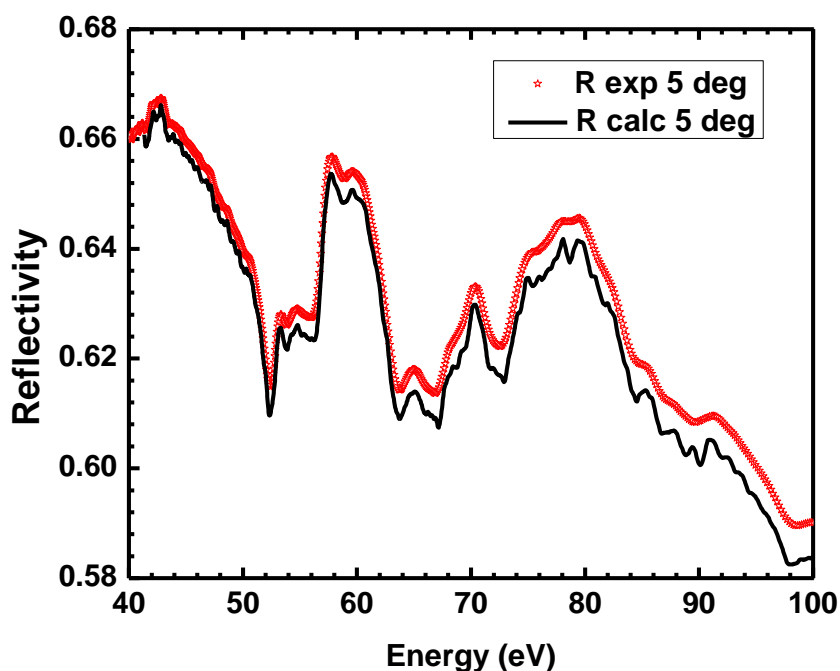


Figure 4-12 Comparison of the measured energy-dependent soft X-ray reflectivity spectra at incidence angles of 5° with the simulated one.

4.5 Conclusions:

Soft X-ray characterization of MgO thin film has been carried out using soft X-ray reflectivity and absorption spectroscopy. X-ray absorption spectroscopy in surface sensitive total electron yield mode near the O K-edge, confirms that the top surface of the film is nothing but MgO only. The rock-salt structure of the thin film is also confirmed. Angle-dependent soft X-ray reflectivity measurements provide information about the structural parameters and the

composition at the film/substrate interface. The optical density profile obtained from SXR analysis confirms the presence of Mg-Si-O and Si-O layers at the film/substrate interface. In-depth profile of the film as obtained from SIMS has also been found to be consistent with in-depth optical density profile.

In the next step we have investigated the optical constants (δ and β) of magnesium oxide thin film in the 40-300 eV energy range covering Mg L-edge from energy-dependent reflectivity measurements. Appearance of fine features is evident from the energy range of 50-75 eV covering the Mg L-edge region. The origin of these features is discussed in details. We have also determined the optical constant (δ) in the energy region of 480-600 eV covering the O K-edge utilizing X-ray absorption results. The origin of the fine features appearing near the O-K edge is also discussed.

Thus, we have conclusively demonstrated the influence of core-hole effect near the Mg L edge on the optical constants (δ and β) through reflectance spectroscopy and first principles DFT studies. The optical constants obtained are also compared with the Henke tabulated values obtained from CXRO website. Intense features appearing as a result core-hole effect as obtained from first principles simulation agrees well with that of the experimentally measured one. Agreement between simulated and measured absorption (β) spectra near the Mg L edge is excellent in terms of peak positions and their relative strength etc.

Chapter 5.**Structural and optical properties of zirconium oxide**

This chapter deals with the investigation of optical properties in extreme ultraviolet (EUV)/ Soft X-ray region along with the characterization of surface and interface of ZrO₂ thin film deposited on different type of substrates like Si & GaAs. The underlying physical aspects of the optical properties of ZrO₂ and its correlation with the electronic structure are investigated using both angle & energy-dependent reflectance spectroscopy. We used the Kramers-Kronig (KK) relations to the energy-dependent reflectance data in order to extract the absolute values of dispersion & absorption (optical constants) from 500-600 eV covering the O K-edge. The various factors associated with the calculation of fine spectrum of optical constants using KK relations and its implications are discussed.

5.1 Introduction:

Zirconium oxide (ZrO_2) thin films have wide range of applications in science and technology owing to their attractive mechanical, thermal and chemical properties¹⁷³. The various applications of zirconium oxide as optical elements in EUV/ Soft X-ray region have already been discussed in Chapter 1. Despite of several use of ZrO_2 in soft X-ray region no experimental data of optical constants are available. Moreover, formation of surface/interface and the nature of interaction with other substrate/layer material and their relation with the optical constants are also scarce. The electronic properties of the thin films are generally found to be different from its bulk counterpart. Thus, experimental investigation of the relation of optical constants with the electronic structure of the film is also an important requirement.

In literature, few studies on the compositional analysis of zirconium oxide thin film are available. N.L. Zhang et al.¹⁷⁴ studied the interfacial and microstructural properties of zirconium dioxide thin film on silicon substrate using X-ray photo electron spectroscopy (XPS) technique. XRD analysis suggests that the film was amorphous upto 700°C, above this it became polycrystalline. Moreover, transmission electron microscopy (TEM) analysis confirmed the formation of interfacial layer in 700°C annealed film, which is attributed due to the interaction between diffused oxygen from annealing ambient and Si.

S. Harasek et al.¹⁷⁵ carried out the compositional analysis of metal-organic chemical vapour deposited (MOCVD) zirconium dioxide film using Auger electron spectroscopy. Presence of fluorine along with oxygen vacancies was confirmed in the as-deposited film, while for the annealed film fluorine was not present and the oxygen content was increased remarkably ensuring stoichiometric ZrO_2 film.

In the present study optical constants of e-beam deposited ZrO_2 thin film (450 Å thick) deposited on GaAs substrate are measured in 55 – 150 Å wavelength region (~80-225 eV energy region) covering Zr $M_{4,5}$ edge using angle dependent reflectivity technique. Soft X-ray reflectivity (SXR) measurements are performed using reflectivity beamline at Indus-1 synchrotron radiation source. Optical constants obtained from the fitting of reflectivity data are then compared with Henke's tabulated values. We have also carried out a detailed depth graded compositional analysis using soft X-ray reflectivity and X-ray photoelectron spectroscopy technique. SXR has been used to obtain the optical index profile and to obtain the depth graded compositional details of the thin film quantitatively. In depth composition of the film is obtained from the best fit of optical density profile. Further, XPS technique is used to obtain the chemical composition of the film, the results obtained are compared.

We have also investigated the fine optical constants spectrum of zirconium oxide thin film on Si substrate near the O K-edge region. The initial investigation of the structural parameters of the film is carried out by grazing incidence X-ray reflectivity (GIXRR) technique using 1.54 Å wavelength. Thereafter, energy-dependent soft X-ray reflectivity and absorption measurements in total electron yield mode are carried out simultaneously at different grazing angles of the films covering the O K-edge region.

5.2 Experimental details:

The zirconium oxide films were prepared using electron beam evaporation technique. One set of thin film was deposited on a Gallium Arsenide (GaAs) substrate using an electron beam deposition system (EBG-PS-3K, Hind HIVAC). The deposition was carried out at a constant pressure of 6×10^{-4} Pa with a typical deposition rate of ~3–4 Å/s at 80°C. ZrO_2 pellets of

>99.97% purity were used as a source material for the deposition in the e-beam coating unit. The thickness of the film was monitored in situ using a quartz crystal monitor.

Another set of film was deposited on silicon substrate. Prior to deposition, the substrate were cleaned with acetone ultrasonically. The deposition was carried out at a pressure better than 2.6×10^{-4} Pa with a typical deposition rate of 0.3 \AA/s .

5.3 Results and Discussions:

5.3.1 Initial Characterization: GIXRD & GIXRR

Initial characterization of the ZrO_2 thin film deposited on GaAs substrate was carried out using Grazing incidence X-ray diffraction (GIXRD) & GIXRR to determine the structural parameter and crystallinity of the film.

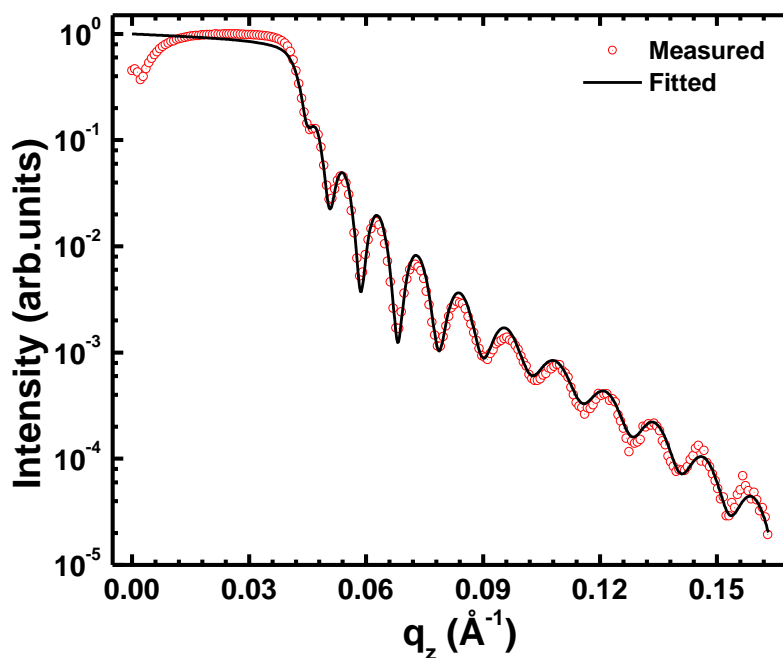


Figure 5-1 Measured (circle) and fitted (solid line) GIXRR spectra of ZrO_2 thin film for $\lambda = 1.54 \text{ \AA}$ are shown.

GIXRD measurement confirms that the film is polycrystalline in nature. The peaks (101), (110), (200) and (211) are assigned to the tetragonal phase of ZrO_2 . It has been reported that the

lattice oxygen vacancies (due to change in partial pressure of oxygen during deposition) are mainly responsible for tetragonal phase of ZrO_2 . Details of GIXRD results are given in Ref.¹⁷⁶

GIXRR measurements are carried out to determine thickness, density and surface/interface roughness. Figure 5-1 shows the measured and fitted GIXRR curves of 450 Å thick ZrO_2 thin film using Cu $K\alpha$ radiation ($\lambda=1.54\text{\AA}$). In order to get the best fit, different models i.e. 2-layer, 3-layer and 4-layer are tried. The consistent fit parameters, which could give a best fit for all R versus θ curves ($\lambda=1.54\text{\AA}$ and soft X-ray wavelengths), were obtained with 3-layer model as shown in Figure 5-2. The model comprised of a native oxide layer on the substrate, a ZrO_2 principal layer and a top layer formed due to contamination/oxidation. Rigorous analysis of GIXRR data reveals the thickness and roughness of the film as given in Table 5-1.

Table 5-1 Structural parameters of ZrO_2 thin film deposited on GaAs substrate as obtained from GIXRR analysis.

Layer	Thickness (Å)	Roughness (Å)
Top	30±1.0	8.6
Principal ZrO_2	465±1.5	11
Interface	31±2.0	6.2
Substrate	--	7.9

Figure 5-2 shows the variation of Scattering Length Density (SLD) with respect to film thickness as derived from the fit parameters of GIXRR data. It is evident from the figure that the film is uniform across the depth except near the air/film interface and film/substrate interface region. The analysis reveals the density of the film as ~4.5 g/cc, which is ~80% of the bulk density (5.68 g/cc) of stoichiometric ZrO_2 . The reduced density could be attributed to the presence of oxygen and voids in the film.

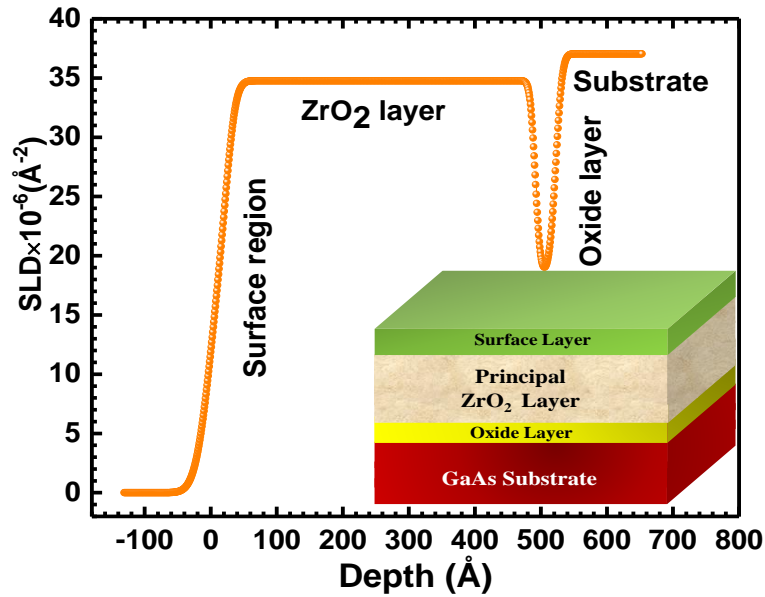


Figure 5-2 Variation of Scattering length density (SLD) with respect to thickness as derived from the GIXRR fit of the measured data of ZrO_2 thin film is shown. Schematic of the three-layer model used for the fitting is also shown.

Further a dip in the ODP profile near the Substrate/Film interface indicates the presence of native oxide layer. In GaAs substrate the native oxide layer is attributed to Ga_2O_3 and/or As_2O_3 . The information of structural parameters obtained from GIXRR fit is used for SXR data analysis to determine optical constants of the ZrO_2 thin film.

As discussed in Chapter 3, the measurement error in density analysis is obtained from the relation $-\frac{d\rho}{\rho} = 2 \left(\frac{dq}{q_c} \right)$. For zirconium oxide $\rho = 4.50 \text{ g/cc}$, (as obtained from the fit value of δ), the step size of momentum transfer (q_z) is 0.0007 \AA^{-1} and the critical angle in terms of q_c is 0.0417 \AA^{-1} which yields an error in density determination to be $\sim 0.15 \text{ g/cc}$.

The analysis error in density determination can be estimated by calculating the difference between critical angle of measured and fitted GIXRR curve. From Figure 5-1, the difference between the critical angle (θ_c) of the fitted and the measured GIXRR curve is found to be $\Delta\theta_c \approx 0.006$. Thus, the analysis error in density is $d\rho = 0.189 \text{ g/cc}$.

5.3.2 Investigation of optical constants of ZrO_2 covering Zr $M_{4,5}$ edge.

To determine the optical constants in the soft X-ray region of 55-150 Å (~225-82 eV), the angle-dependent SXR measurements are carried out at Indus-1 Reflectivity beamline. Figure 5-3 shows the measured and fitted SXR curves in 55-150 Å (~225-82 eV) wavelength region measured in 10 Å step.

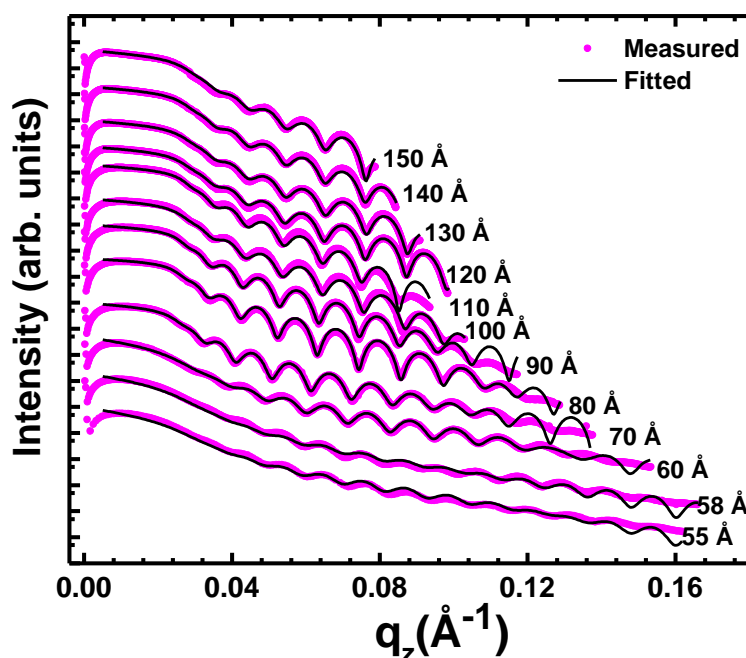


Figure 5-3 Measured (circle) and fitted (solid line) SXR curves of ZrO_2 thin film are shown for different incident wavelengths in the 55–150 Å wavelength region. Reflectivity data are fitted with the same model used in GIXRR data analysis. Curves are vertically shifted for the sake of clarity.

In the close vicinity of the Zr $M_{4,5}$ absorption edge, SXR measurements are carried out in 1 Å and 0.5 Å step increment and results of those are shown in Figure 5-4 along with their best fit. SXR data are fitted with the same three layer model (1-oxide layer, 2- ZrO_2 principal layer and 3-surface/contamination layer) as used for GIXRR data analysis. To obtain more reliable values of optical constants and to reduce the number of fit parameters, thickness and roughness values obtained from the GIXRR fit are kept fixed. Values of optical constants are varied in a

controlled manner to obtain a best fit. This approach reduces the number of variable parameters in χ^2 minimization process just to obtain optical constants delta (δ) and beta (β) only.

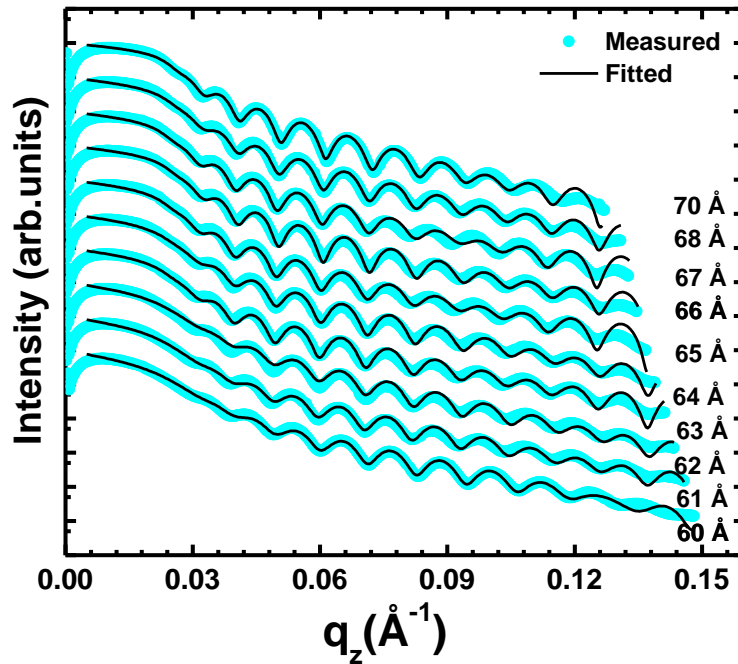


Figure 5-4 Measured (circle) and fitted (solid line) angle-dependent SXR curves of ZrO₂ thin film near the Zr M_{4,5} edge are shown. Curves are vertically shifted for the sake of clarity.

Table 5-2 Experimental and tabulated optical constants of ZrO₂ in the 55-150 Å wavelength region (~225-82 eV).

Energy (eV)	Wavelength (Å)	δ (Exp)	δ (Tab)	β (Exp)	β (Tab)
225.42	55	0.005(8)	0.00578	0.004(8)	0.00464
213.76	58	0.0064(0)	0.00623	0.005(1)	0.00455
206.64	60	0.006(7)	0.00631	0.004(7)	0.00394
204.94	60.5	0.006(6)	0.00646	0.004(1)	0.00367
203.25	61	0.006(7)	0.00666	0.003(5)	0.00344
199.97	62	0.007(0)	0.00723	0.003(1)	0.00306
196.80	63	0.007(1)	0.00789	0.003(0)	0.00289
193.72	64	0.007(3)	0.00847	0.003(3)	0.00287
190.74	65	0.007(5)	0.00895	0.002(9)	0.00282
187.05	66	0.008(2)	0.00946	0.002(8)	0.00275
185.05	67	0.007(9)	0.01004	0.002(9)	0.00270
182.33	68	0.008(8)	0.01061	0.003(3)	0.00275
177.12	70	0.009(4)	0.01159	0.003(1)	0.00279
154.98	80	0.012(9)	0.01691	0.003(7)	0.00377
137.76	90	0.017(2)	0.02235	0.004(5)	0.00507
123.98	100	0.021(2)	0.02831	0.006(9)	0.00670
112.71	110	0.028(0)	0.03476	0.006(9)	0.00866
103.32	120	0.032(6)	0.04185	0.010(8)	0.01091
95.37	130	0.0387(6)	0.04949	0.012(9)	0.01353

88.56	140	0.045(6)	0.05792	0.014(0)	0.01651
82.65	150	0.053(8)	0.06716	0.018(2)	0.01988

We have also tried to show the accuracy of experimentally obtained optical constants measured from X-ray reflectivity technique. The accuracy of the optical constants depends on β/δ ratio.^{1,3} If this ratio is less than one ($\beta/\delta < 1$), i.e., absorption is not dominant, then the critical angle θ_c can be calculated from the relation- $\theta_c = \sqrt{2\delta}$. This can be done easily because in this case the reflectivity pattern has a well-defined shoulder and thus δ and β can be uniquely determined. As $\frac{\beta}{\delta} \rightarrow 1$, the reflectivity pattern becomes exponential like due to dominance of absorption. If the β/δ ratio is greater than one ($\beta/\delta > 1$) then the critical angle region in reflectivity pattern is not distinguishable and it is not possible to determine δ and β uniquely. So for the region with $\beta/\delta > 1$, the uncertainty in determination of δ and β is very high.

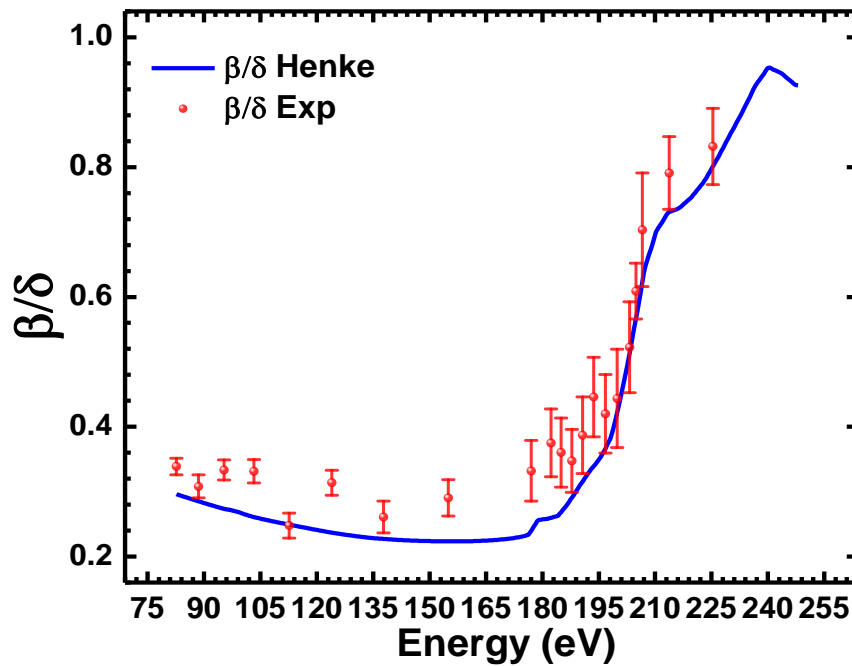


Figure 5-5 β/δ ratio for experimentally derived optical constants (in circle) along with the β/δ ratio for Henke's tabulated values (in solid line) are shown.

Figure 5-5 shows the β/δ ratio for experimentally derived optical constants of ZrO_2 principal layer along with the β/δ ratio for Henke's tabulated values. It is evident that β/δ ratio is less than one (also in close agreement to β/δ ratio for Henke's values) in the whole wavelength region suggesting that the measured optical constant values have minimum uncertainty. The experimentally measured optical constants for ZrO_2 are listed in Table 5-2 along with the tabulated Henke values and same are plotted in Figure 5-6.

It is evident from the figure that in 70-150 Å wavelength region (~177-82 eV) the measured δ values are consistently lower than the tabulated Henke values. The measured delta values are lower by 19 to 24%. Below 70 Å wavelength (near Zr $M_{4,5}$ absorption edge/ 177 eV) the measured δ values are lower by 3 to 21%. The mismatch between tabulated and experimentally obtained δ values show an inconsistent picture as beta values are lower by 1-8% in 70-150 Å wavelength region but at some points this deviation increased to 20% value. Below 70 Å wavelength region (55-70 Å) β values are higher than the Henke values by 3 to 20%.

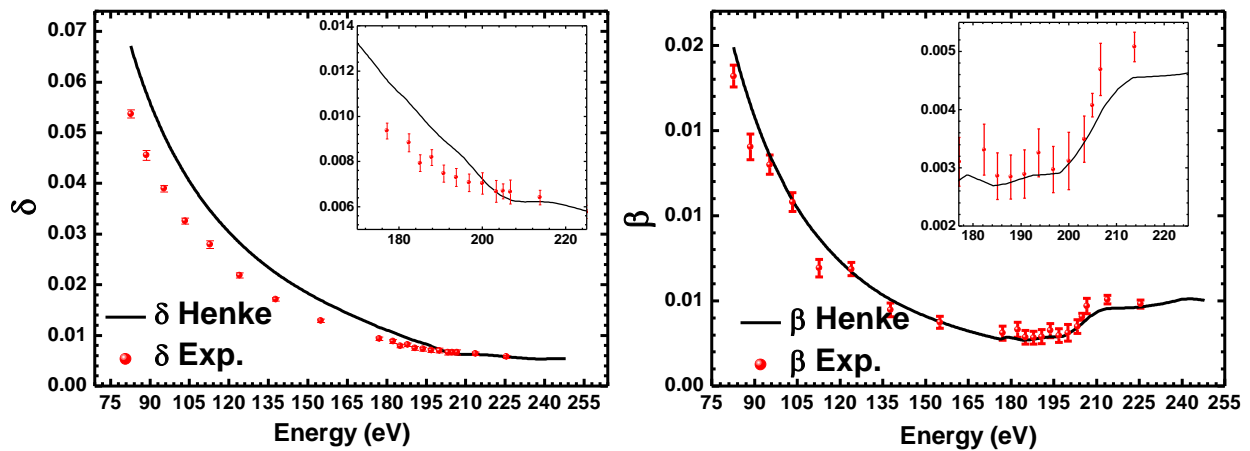


Figure 5-6 Experimentally evaluated optical constants of ZrO_2 thin film are shown as discrete points along with the error bars. In the inset, optical constants near the Zr $M_{4,5}$ edge are shown.

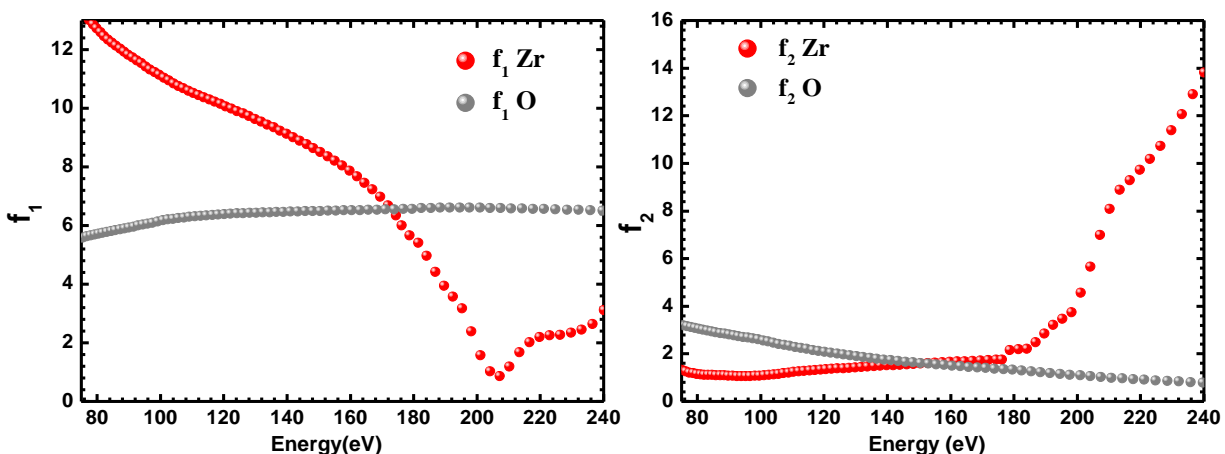


Figure 5-7 Real and imaginary parts of atomic scattering factor f_1 and f_2 , respectively, are plotted in the 80-240 eV (within 55–150 Å) energy region for Zr and O as obtained from the CXRO website.

It is interesting that the measured delta values are consistently lower than the Henke data whereas the change in beta values is slightly inconsistent. This could be understood if the behavior of atomic scattering factors for Zr and O are separately analyzed.

Figure 5-7 shows the atomic scattering factor f_1 and f_2 for Zr and O in the 55-150 Å (~225-82 eV) region which are obtained from the CXRO website. The real and imaginary part of the atomic scattering factor suggest that the f_2 values of Zr and O are very close in 55-150 Å wavelength region (~225-82 eV), whereas the f_1 values of these two elements are significantly different (see Figure 5-7). This suggests that the change in Zr: O ratio (due to presence of oxygen and voids) will not affect the beta values much, but it will lower the delta values significantly. Since density of the film for GIXRR data is found to be ~80% of the bulk density, this indicates the possibility of oxygen and voids which in turn may change the Zr: O ratio. Similar behavior has been observed in optical constant analysis of Zirconium Carbide (ZrC),³² where there was significant mismatch in delta values while the beta values were in close agreement because f_2 values for Zr and C were very close and f_1 values were significantly different.

5.3.3 Optical constants spectra of ZrO₂ thin film near the O K-edge

In the next step we have determined the optical constants of ZrO₂ thin film near the O K-absorption edge regions using energy dependent soft x-reflectivity measurements.

The extraction of optical constants is carried out in similar manner as described in Chapter 4 using the KK relations. The optical constants profile near the O K-absorption edge region shows relatively prominent ϵ_g and t_{2g} features marked as A & B at an energy position of 531.0 & 533.6 eV respectively. Other features appearing in the optical constants profile near the O K-edge region are comparatively broader which is in accordance with the absorption spectra available in literature and also with the TEY spectrum measured at soft X-ray reflectivity beamline (BL-03)¹⁰⁶ of Indus-2 synchrotron radiation source.

5.3.3.1 GIXRR Analysis

For initial characterization of the films Grazing Incidence X-ray reflectivity measurements using Cu K α source ($\lambda=1.54$ Å) is carried out. Figure 5-8(a) shows the measured (scatter) and fitted (solid line) GIXRR data of the zirconium oxide thin film. In order to obtain a best fit of the reflectivity patterns, various models are tried but the best fits are obtained using a three-layer model as discussed earlier. The structural parameters i.e. the thicknesses and roughnesses of the various layers considered in the modelling of the films of different thicknesses are tabulated in Table 5-3.

For initial characterization of the films Grazing Incidence X-ray reflectivity measurements using Cu K α source ($\lambda=1.54$ Å) is carried out. Figure 5-8(a) shows the measured (scatter) and fitted (solid line) GIXRR data of the zirconium oxide thin film. In order to obtain a best fit of the reflectivity patterns, various models are tried but the best fits are obtained using a three-layer

model as discussed earlier. The structural parameters i.e. the thicknesses and roughnesses of the various layers considered in the modelling of the films of different thicknesses are tabulated in Table 5-3.

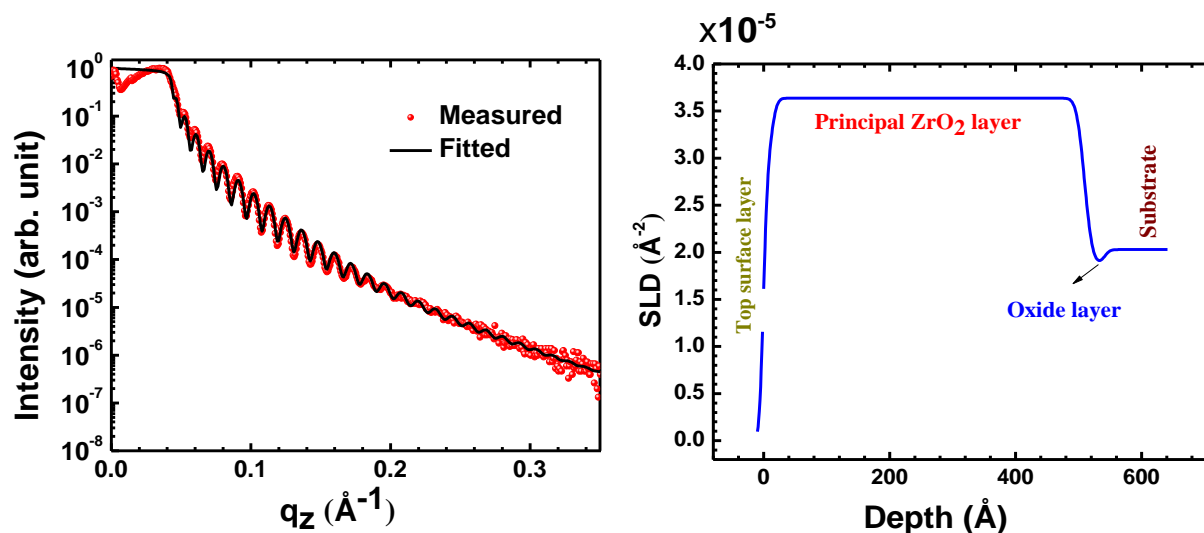


Figure 5-8 (a) Measured (scatter) and fitted (solid line) GIXRR curves of as-deposited 500 Å ZrO₂ thin film. The curves are vertical shifted for clarity. (b) Variation of δ along the depth of the as-deposited 500 Å. ZrO₂ films obtained from the modelling of the GIXRR data.

Table 5-3 Structural parameters of different layers of the as-deposited 500 Å ZrO₂ film as obtained from the analysis of the GIXRR data.

Layer	Thickness (Å)	Roughness (Å)
Top	11±2.0	4.9
Principal	499±2.0	7.9
Interface	32±3.0	10.0
Substrate	--	6.5

Figure 5-8(b) shows the variation of scattering length density (SLD) along the film depth. It is confirmed that the density variation of the film is uniform along the depth except at the film/substrate and the air/film interfaces. The density of the film is found to be 83% of the bulk density (5.68 g/cc). However, the information obtained using an X-ray probe source of 1.54 Å,

which is far away from the absorption edges of both Zr as well as O fails to provide complete picture of the local environment of the films.

From the analysis of the GIXRR data, $\rho = 4.71 \text{ g/cc}$, (as obtained from the fit value of δ), the step size of momentum transfer (q_z) is 0.0007 \AA^{-1} and the critical angle in terms of q_c is 0.042 \AA^{-1} . Thus the measurement error in density determination is found to be $\sim 0.16 \text{ g/cc}$.

As discussed earlier, the analysis error in density determination can be estimated by calculating the difference between critical angle of measured and fitted GIXRR curve. From Figure 5-1, the difference between the critical angle (θ_c) of the fitted and the measured GIXRR curve is found to be $\Delta\theta_c \approx 0.005$. Thus, the analysis error in density determination is, $d\rho = 0.157 \text{ g/cc}$.

5.3.3.2 Energy dependent SXR measurements

Soft X-ray reflectivity measurements were carried out in the energy region of 500-565 eV covering O K-edge with an energy accuracy of 0.5 eV. The measurements were carried out at an incidence angle of 2° , 3° & 5° . The spectra measured at 2° were considered for the evaluation of optical constants profile near the O K-edge region.

Figure 5-9 shows the measured energy dependent soft X-ray reflectivity spectrum of ZrO_2 thin film covering O K-edge. From the measured reflectivity profiles the optical constants profiles of the films are evaluated for using the same methodology as mentioned in Chapter 2.

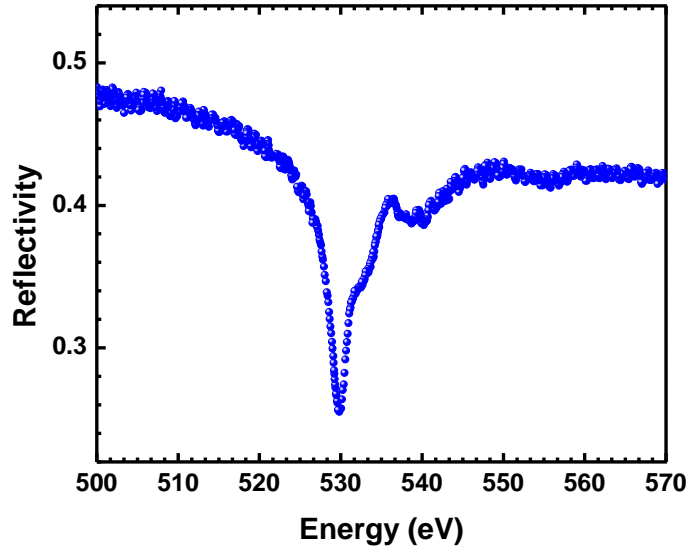


Figure 5-9 Shows the reflectivity spectrum of ZrO_2 measured at an incidence angle of 2° covering the O K-edge region.

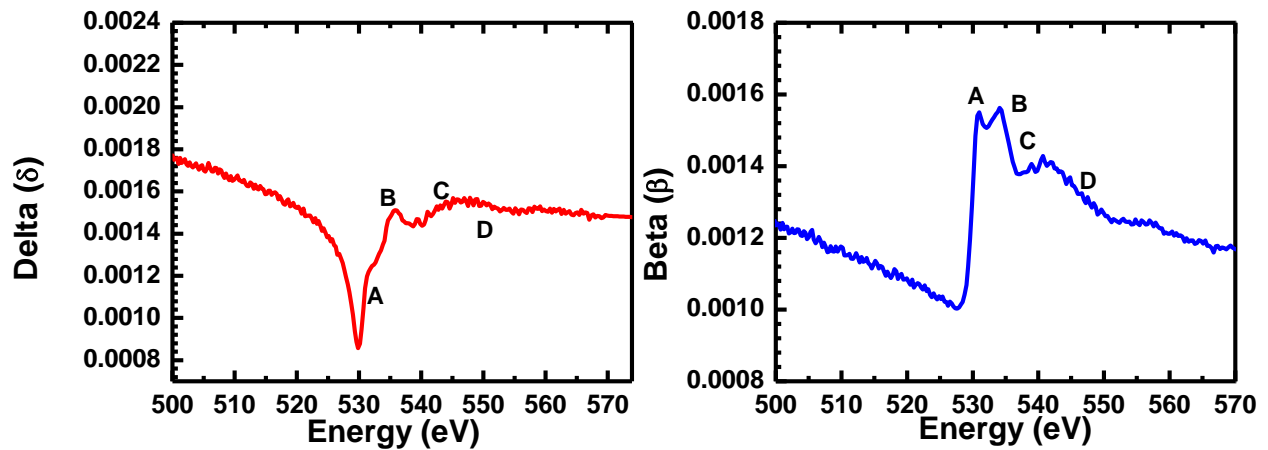


Figure 5-10 Measured values of delta (δ) & beta (β) obtained from KK analysis of reflectivity versus photon energy data near O K-absorption edge.

Figure 5-10 shows the optical constants (δ & β) profiles of the zirconium oxide thin film near the O K-edge region as determined from the reflectivity spectra obtained at an incidence angle of 2° . The prime features appearing in the beta spectrum are marked as A-D and these matches well with the absorption spectrum available in literature.^{177,178} The obtained beta spectrum also matches well with the measured TEY spectra at normal incidence as shown in Figure 5-11.

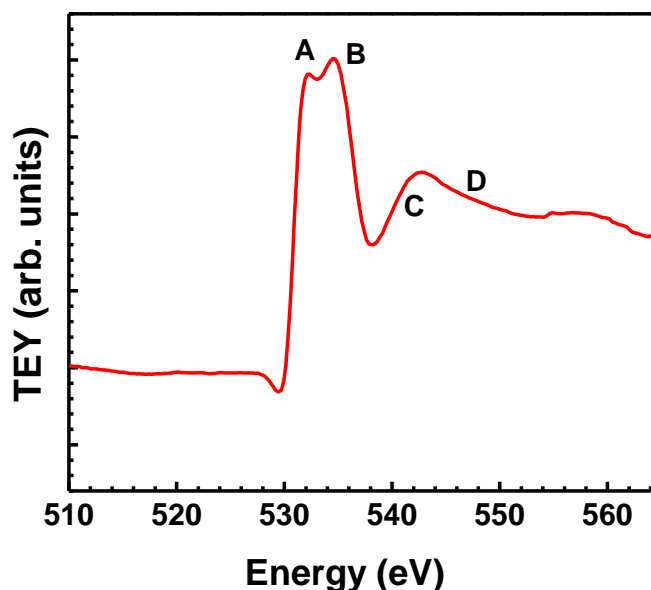


Figure 5-11 X-ray absorption spectrum (XAS) of ZrO₂ thin film measured in total electron yield mode at normal incidence geometry.

The background subtraction of the measured TEY data is carried out using ATHENA software.¹⁷⁹ The origin of the features in the energy range of 530–540 eV can be attributed due to the transitions from O 1s states to O 2p final states, which are hybridized with the Zr 4d states, split by the crystal field effects. The two peaks in this region, located at the energy position of ~531.0 and ~533.8 eV are of e_g and t_{2g} symmetry. Above 540 eV the features appearing are attributed due to transitions from O 1s states to oxygen 2p states mixed with Zr 5s states. From degeneracy arguments, the e_g : t_{2g} intensity ratio must be 2:3 (0.66). However, in our case this ratio is found to be 0.95 i.e., it deviates significantly from the standard value. This deviation is generally related to a difference in distribution of the O 2p weight among the e_g and t_{2g} states in the compounds.

Above 540 eV the features appearing in the TEY spectra are marked as C and D. These features originate as a result of transition from oxygen 1s state to oxygen 2p states mixed with Zr 5s states, which are pushed up in energy due to the larger oxygen 2p–metal 5sp interactions.

5.3.3.3 Checking the accuracy of the optical constants near O K-edge of ZrO₂ thin film.

The next step was to check the accuracy of the obtained optical constants. For this we have used the structural parameters i.e. the thickness & roughness of the different layers of the film along with the investigated optical constants and simulated the reflectivity pattern.

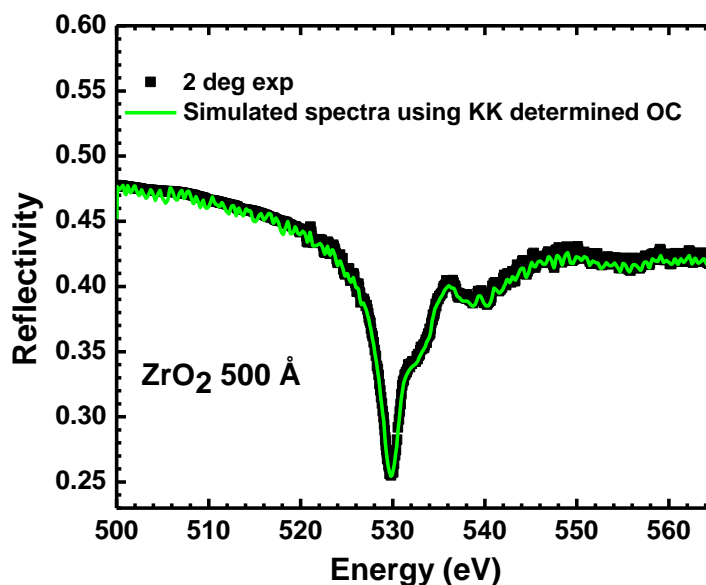


Figure 5-12 Comparison of the measured energy-dependent soft X-ray reflectivity spectra at incidence angles of 2° with the simulated one.

On comparison of the simulated reflectivity spectra using the investigated optical constants with the measured one, a difference of the order of ~ 0.005 is found which is extremely small, confirming the fact that the obtained optical constants are reliable and accurate.

5.3.4 Glancing Incidence TEY

Glancing angle absorption measurements are also performed covering the O K-edge region to understand the oxygen distribution throughout the depth of the film. However, there are several limitations of XAS measurement in total electron yield mode at glancing angle geometry. For example, in this case the effective sampling depth might be comparable to the X-ray penetration depth, resulting in the distortion of the TEY spectra. Thus, under this condition the TEY

spectrum is not equivalent to the absorption spectrum. In spite of this limitation, other useful information can be obtained from the glancing angle TEY spectrum, which is not explored by the researchers.

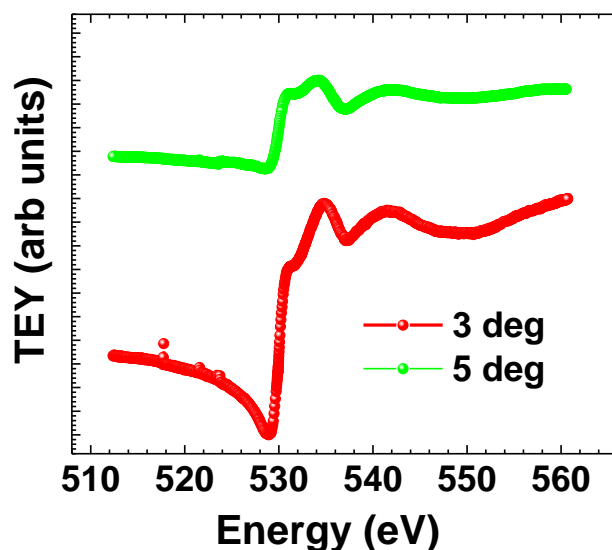


Figure 5-13 Total electron yield (TEY) spectra of zirconium oxide thin film measured at an glancing angle of 3 & 5 degree respectively.

Very few literatures are available which focuses on the spectral features appearing as a result of grazing incidence total electron yield (TEY) spectra. It is evident that in spite of its dissimilarity with the absorption spectra, grazing incidence TEY spectra provides a wealth of information especially for anisotropic samples.^{180,181} It also provides information about the hidden multiplet structures present in the absorption spectrum.¹⁶⁴ Figure 5-13 shows the measured total electron yield spectra at glancing incidence angles of 3 & 5 degree respectively. It is clear that at an angle of 3°, a dip is observed before the onset of the absorption edge. To understand this, we have simulated the total electron yield spectrum for 3°, taking into account the measured reflectivity data along with the obtained optical constants. However, the above consideration does not exactly replicate the total electron yield spectra. Following the work of Andreeva et al.

^{181,180}we tried to simulate the obtained yield spectra considering different contribution of the electrons arising from two different absorption processes.

$$Y = \left(\tau_{nres} \frac{2(1-\delta)\beta}{\lambda} + \tau_{res} \frac{2(1-\delta_{KK})\beta_{KK}}{\lambda} \right) E_f \frac{\lambda_e}{\lambda_e + \beta \lambda_e} \times \left[1 - \exp \left\{ \left(-\beta + \frac{1}{\lambda_e} \right) d \right\} \right] \quad (5-1)$$

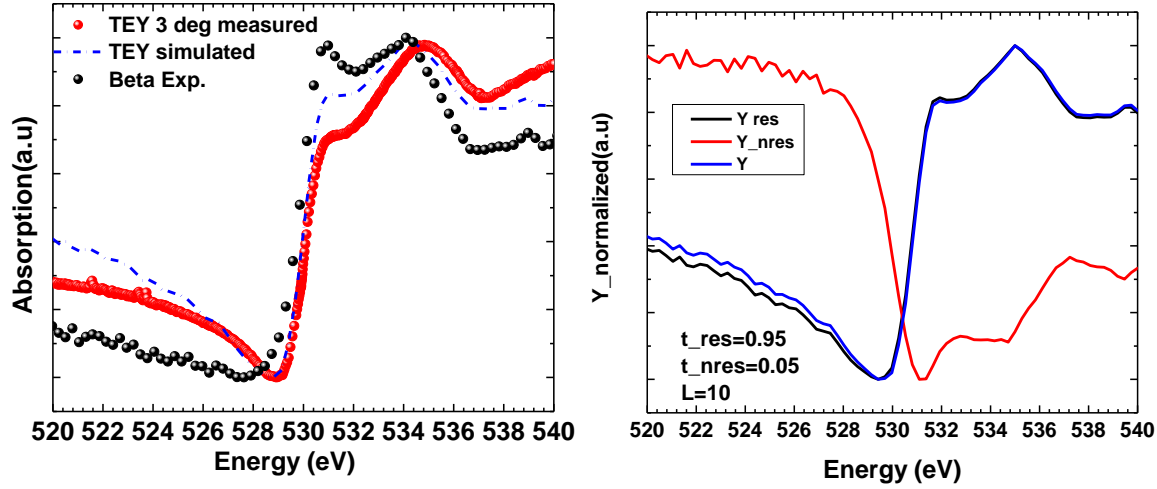


Figure 5-14 (left) Measured (red scatter) and simulated (blue short dot dash) total electron yield spectra considering the contribution of electrons originating from both resonant and non-resonant absorption processes separately. For a complete understanding we have also plotted our experimentally obtained beta (β) spectra normalized wrt the TEY spectra. (right) the behavior of the resonant and the non-resonant contribution along with the net total electron yield contribution covering the O K-edge of off-stoichiometric zirconium oxide thin film. The parameters of the simulated TEY spectrum are $\tau_{nres}=0.05$ and $\tau_{res}=0.95$, with the electron escape length of 10 Å. The energy scale of the simulated spectra is shifted to a certain value which is well within the energy resolution of beamline.

Equation (5-1) shows the expression of total electron yield where, $E_f = \left| E_0 + \right.$

$\left. \frac{\sin\theta - \sqrt{N^2 - \cos^2\theta}}{\sin\theta + \sqrt{N^2 - \cos^2\theta}} E_0 \right|^2$ is the internal electric field of radiation, $N=1-\delta+i\beta$ is the complex refractive

index, λ_e is the escape length of electrons, d is the film thickness, E is energy of incident photons & τ is a constant parameter determining the no. of photoelectrons for one absorbed photon. τ_{nres} & τ_{res} corresponds to the number of photoelectrons originated from two different absorption process- non-resonant i.e., where the Zr atoms also participates even when the sample is scanned through the O K-edge & the resonant process dominant near the absorption edge region. Taking into account the different contribution of τ_{nres} & τ_{res} the total electron yield spectra replicates well with the measured one.

5.4 Depth resolved compositional analysis using non-destructive SXR technique

5.4.1 XPS analysis

Figure 5-15 shows the Zr 3d and O 1s core levels XPS spectra of the ZrO_2 thin film for as deposited and 10 minutes sputtered film. The vertical dotted lines corresponds to the peak position of binding energies of different phases as obtained by fitting and verified from the values as reported in refs.^{142,182}. The higher value of FWHM of Zr 3d and O 1s core level spectra indicates the presence of more than one combined chemical composition of Zr and O. Thus the XPS spectra corresponding to O 1s & Zr 3d are de-convoluted using Gaussian de-convolution method and the percentage contribution of each phase for different core levels are summarized in Table 5-4.

In the analysis of Zr 3d spectra the intensity ratio was locked to 3:2 for Zr 3d_{5/2} and Zr 3d_{3/2} respectively. XPS analysis confirmed the presence of ZrO_2 and ZrO_x with percentage contributions of 98.1% and 1.9% respectively for the as-deposited film. The binding energy value of ZrO_2 at the Zr 3d core level are 183.5 eV (3d_{5/2}) and 185.9 eV (3d_{3/2}) respectively, while for ZrO_x the binding energy value corresponding to 3d_{5/2} and 3d_{3/2} are 180.9 eV and 183.2 eV respectively. Thus, it is difficult to identify separately the peak corresponding to Zr 3d_{3/2} core level of ZrO_x . Similarly, the analysis of the O 1s core level confirms the presence of ZrO_2 phase along with chemisorbed oxygen (possibly from oxygen voids) having the percentage contributions of 35.7% and 64.3 % respectively. The analysis of as deposited XPS spectra of O 1s core level suggests the presence of strong oxygen on the surface.

Table 5-4: Percentage contribution of various phases obtained from de-convolution of XPS spectra from Zr 3d and O 1s respectively.

Coating	Zr (3d)				O (1s)		
	Phase	Area	BE (eV)		at%	Phase	at%
ZrO ₂ As-deposited	ZrO ₂	41596 27730	183.59 185.98	98.13	ZrO ₂ O	35.7 64.3	531.25 532.39
	ZrO _x	790 526	180.84 183.28	1.87			
ZrO ₂ Sputter etched 10 min	ZrO ₂	64891.3 43260.87	183.54 185.94	94.38	ZrO ₂ O	84.06 15.94	531.39 533.33
	ZrO _x	3857.9 2571.94	180.9 183.2	5.62			

Just after the sputtering of 10 minutes, a change in the intensity of the spectra is observed and the percentage contributions of both the ZrO₂ and ZrO_x phases in Zr 3d core level are found to be 94.4% and 5.6% respectively.

Similarly for O 1s core level spectrum, a remarkable change is observed and the percentage contributions of ZrO₂ phase and the chemisorbed oxygen is found to be 84 % and 16% respectively. After 10 minute of sputtering, ~16% chemisorbed oxygen is present, indicating the possibility of oxygen voids in the depth of ZrO₂ thin film. Since the ZrO₂ film in the present study have a large thickness of 450 Å, XPS technique cannot provide the complete in-depth information of the film. Also the changes in the film from Ar ion sputtering in depth profiling are unknown.

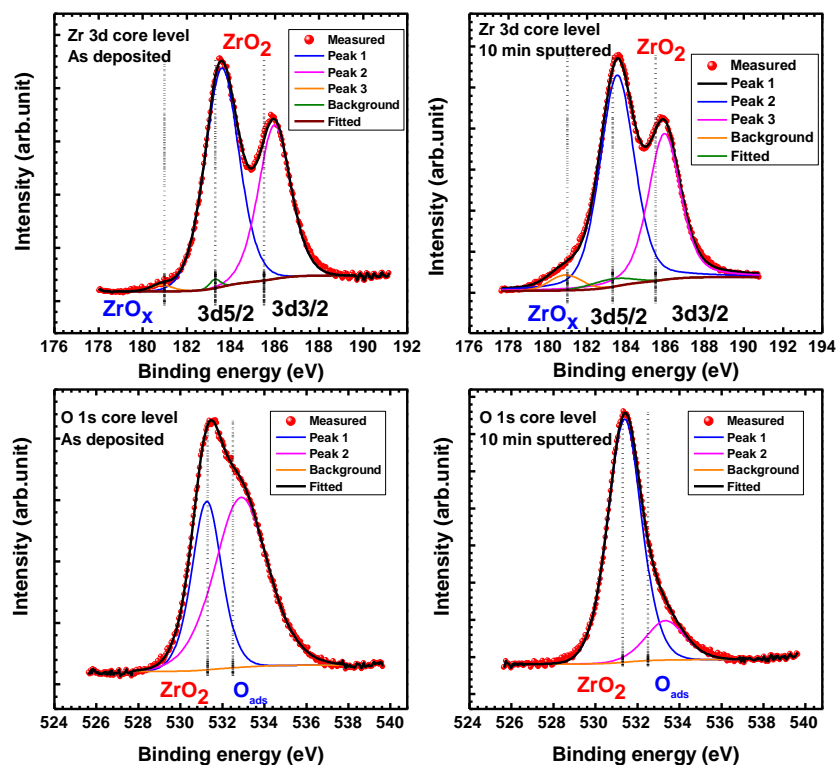


Figure 5-15 XPS spectrum of zirconium dioxide thin film at Zr 3d and O 1s core levels for as-deposited and 10 min sputtered film. The spectra are deconvoluted using Gaussian de-convolution method and two different phases of ZrO_x and ZrO_2 are identified along with the presence of oxygen.

5.4.2 Investigation of chemical composition by SXR in qualitative manner

The next approach adopted for determining the chemical composition of the film qualitatively is the SXR technique. The main advantage of this technique is that it can provide an overall description of the composition of the principal as well as the interfacial layer. The optical density profile corresponding to few discrete photon energies obtained from the modelling of the SXR data are shown in Figure 5-16.

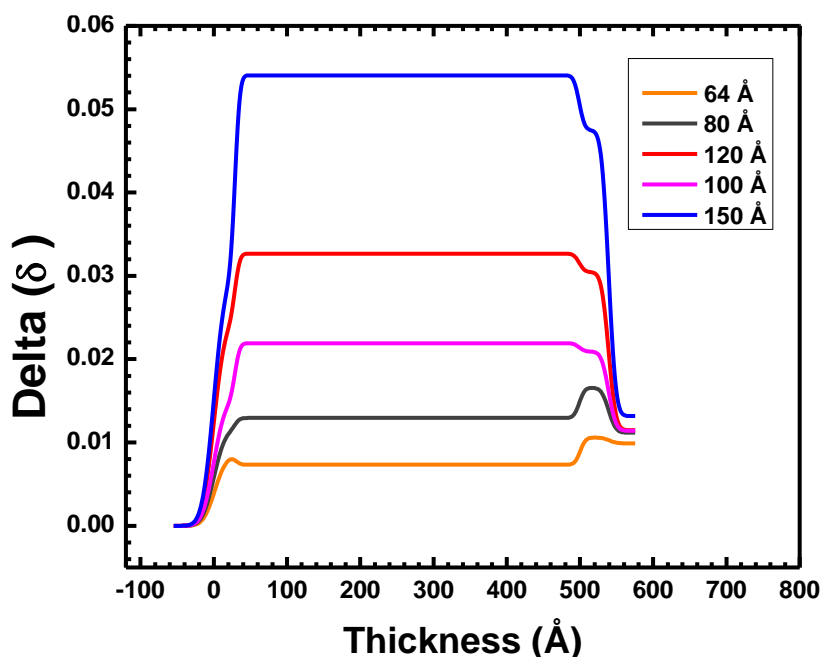


Figure 5-16 In-depth optical index profiles of 450 Å zirconium oxide thin film using $\lambda = 64 \text{ Å}$, 80 Å , 100 Å , 120 Å and 150 Å wavelengths are shown. The different regions in the film are marked.

From Figure 5-16 it is clear that the film is uniform across the depth except near the air/film interface and the film/substrate interface regions. It is obvious from the figure that near the film/substrate interface the optical index profile shows a hump and the value of it is slightly higher than that of optical index value of principal layer at $\lambda = 64 \text{ Å}$ and 80 Å . Whereas in case of profile determined using $\lambda = 100 \text{ Å}$, 120 Å and 150 Å there is a shoulder near the film/substrate interface region and the height of it is marginally lower than the principal layer optical index value. Before we explain this let us first recall the optical index value of Ga_2O_3 and As_2O_3 for 80 % of the bulk density at 64 Å and 80 Å both. At $\lambda = 64 \text{ Å}$ $\delta_{\text{Ga}_2\text{O}_3} = 1.22\text{e-}2$ and $\delta_{\text{As}_2\text{O}_3} = 1.104\text{e-}2$ and this is near to the obtained experimental delta value of the interfacial layer ($\delta = 7.953\text{e-}3$). Further, the delta value for ZrO_2 corresponding to bulk density is $8.4\text{e-}3$ and corresponding to 80 % of bulk density it is $6.7\text{e-}3$. So the presence of hump at the interface region for $\lambda = 65 \text{ Å}$ and 80 Å profile is either due to presence of oxides of GaAs as delta value of either of two are higher

than that of ZrO_2 . Similarly for $\lambda=100\text{\AA}$, 120\AA and 150\AA the delta values of the principal ZrO_2 is higher in comparison that of the oxides of GaAs. The in-depth optical index profile also clearly indicates that the film composition at the interface and that at the principal layer region are totally different. Figure 5-17 shows the δ (left) and β (right) profile of the principal ZrO_2 layer obtained from the best fit as a function of photon wavelength. The optical constants determined are significantly different from the Henke's tabulated value. These changes may attributed to low density of the film as revealed from GIXRR analysis, where the density of the film is found to be 4.50 g/cc (80% of bulk density) and the absence of pure stoichiometric ZrO_2 as confirmed from the XPS analysis. XPS analysis revealed that the film has a complex composition consisting of different ZrO_x and ZrO_2 phases. To confirm this composition the optical constant profile as obtained from the SXR analysis are further analyzed. For comparison the tabulated values of optical constants of stoichiometric ZrO_2 , $\text{Zr}_{0.8}\text{O}_{2.2}$ and oxygen as obtained from CXRO database are shown in the Figure 5-17.

It is evident from Figure 5-17 that experimental δ values for ZrO_2 film is significantly less than the stoichiometric ZrO_2 . The optical constants which are found to differ from the tabulated values as obtained from the CXRO database are fitted considering the combined fractional contributions of ZrO_2 , $\text{Zr}_{0.8}\text{O}_{2.2}$ and also considering the presence of oxygen voids.

The best fit of the optical constant profile as shown in Figure 5-17 is obtained by taking into account the composition of 60% ZrO_2 , 20% $\text{Zr}_{0.8}\text{O}_{2.2}$ & 20% oxygen. As revealed from fitting of optical constant profile 20% oxygen is found through the depth of the film, which is consistent with XPS results where $\sim 16\%$ oxygen is found after 10 minutes of sputtering. From this composition of the two phases, the elemental concentration of Zr and O is found to be 25.3% and 74.7% respectively. Thus the overall O/Zr ratio is determined to be 2.95.

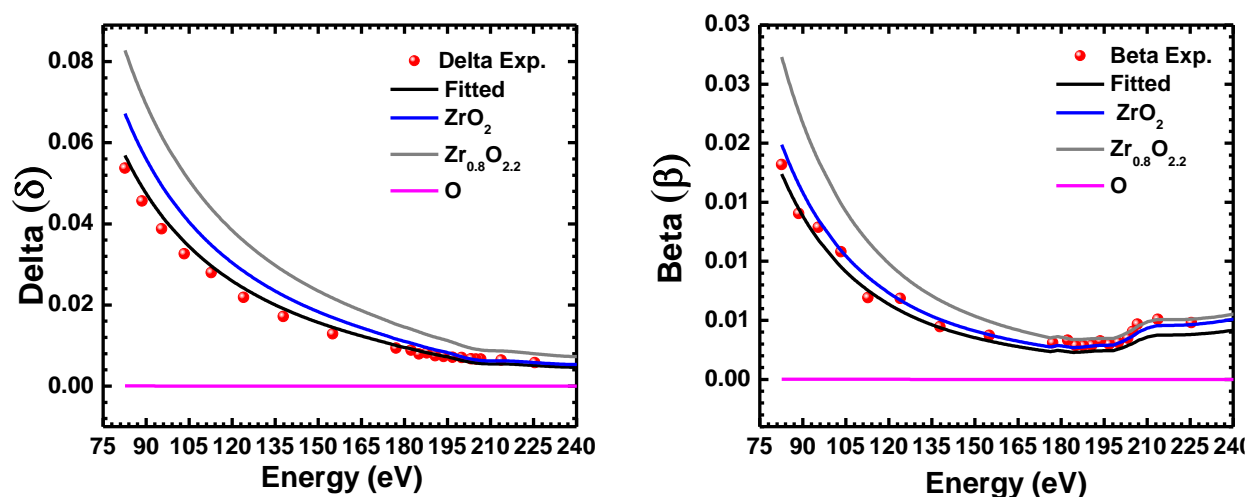


Figure 5-17 Optical constant profile for zirconium oxide thin film as a function of energy over 225–82 eV (55–150 Å) region. CXRO data for $Zr_{0.8}O_{2.2}$ and ZrO_2 are also plotted for comparison. Composition consisting of 60% ZrO_2 and 20% $Zr_{0.8}O_{2.2}$ & 20% oxygen vacancies gives the best fit to the experimentally obtained data.

The most important advantage of using SXR technique is that complete information of the interfacial layer is also obtained along with the principal layer. Figure 5-18Figure 5-17 shows the optical constants profile for interfacial layer of ZrO_2 thin film as a function of wavelength over 55–150 Å (225–82 eV) region. Since the substrate used is GaAs, the interfacial layer is comprised of Ga_2O_3 and As_2O_3 and this fact is clear from the optical density profile. The optical constant profile for Ga_2O_3 , As_2O_3 , ZrO_2 and oxygen are plotted for comparison with the optical constant profile of interfacial layer. The optical constant profile for the interfacial layer is fitted with the fractional composition of Ga_2O_3 , As_2O_3 , ZrO_2 and oxygen profile and the best fit is obtained. The best fit is obtained for 20% As_2O_3 , 25% Ga_2O_3 , 35% ZrO_2 and 20% oxygen.

Analysis suggests that SXR technique provides depth graded composition of the film, which is in good agreement with other techniques like XPS. The advantage of SXR technique is that one can quantitatively estimate the composition of the thin film at higher depths of the film whereas XPS fails to provide such information.

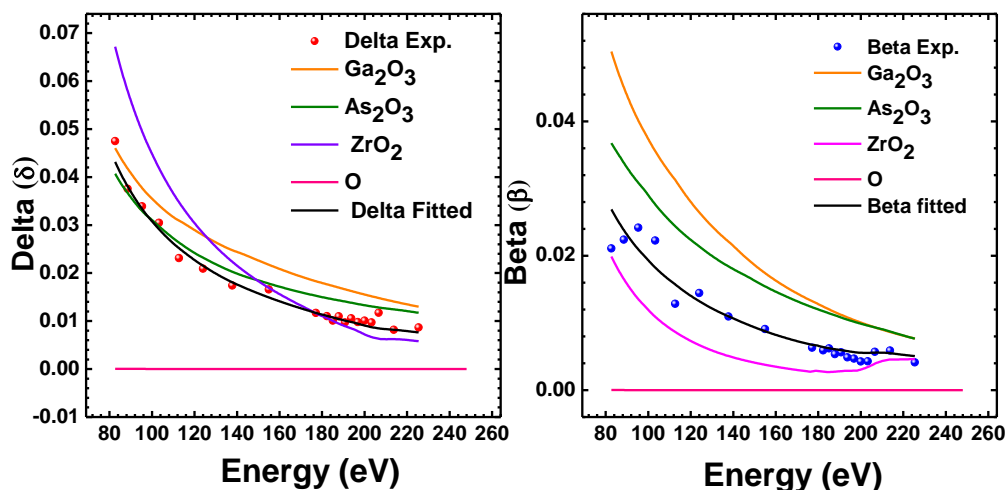


Figure 5-18 Optical constant profile for interfacial layer of zirconium oxide thin film as a function of energy over 225-82 eV (55–150 Å) region. CXRO data for Ga_2O_3 , As_2O_3 and ZrO_2 are also plotted for comparison. Composition consisting of 20% As_2O_3 along with 25% Ga_2O_3 , 35% ZrO_2 and 20% oxygen vacancies gives the best fit to the experimentally obtained data.

5.5 Conclusions:

In the present study angle dependent X-ray reflectivity measurements are used for the determination of optical constants of e-beam deposited ZrO_2 thin film in 55-150 Å (225-82 eV) wavelength region covering the Zr $M_{4,5}$ edge region. Experimental δ and β values are found to be lower by 1 -24 % as compared to tabulated Henke's value in 70-150 Å (177-82 eV) wavelength region i.e., above the Zr $M_{4,5}$ edge region. Below Zr $M_{4,5}$ edge region the measured β values are higher by 1-20% whereas the delta values are lower than the Henke values. The analysis of f_1 and f_2 curves of Zr and Oxygen suggest that the presence of oxygen and voids could lead to the decrement of delta values above 70 Å wavelength region (below 177 eV). We have also investigated the fine optical constants spectra of zirconium oxide film deposited on Si substrate near the O K-edge region. The effect of the crystal field splitting i.e.; the appearance of the e_g and the t_{2g} peaks at an energy position of 531 eV & 533.6 eV respectively is evident in the optical constants spectra. To the best of our knowledge this study presents the first reported

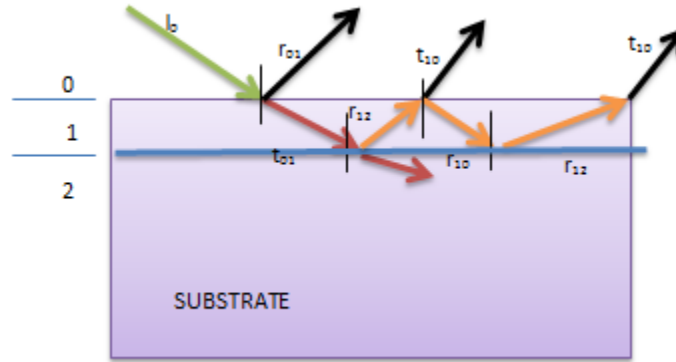
experimental values for optical constants for ZrO_2 compound material. Unlike, the other two material Al_2O_3 and MgO we haven't observed any core-hole feature

In this chapter, we also tried to address the issues associated with glancing angle total electron yield spectra. It is evident that at glancing angle condition the contribution of electrons originating from the resonant & non-resonant atoms varies and results in the creation of a dip before the onset of absorption edge.

In the next stage, SXR technique was used along with XPS to extract the in-depth compositional information of e-beam deposited ZrO_2 thin film. The compositional analysis of ZrO_2 film was estimated quantitatively by obtaining the best fit of the optical constant profile over 55-150 Å (225-82 eV) region. The best fit of the optical constant profile was obtained by taking into account the composition of 60% ZrO_2 , 20% $\text{Zr}_{0.8}\text{O}_{2.2}$ & the remaining part consists of oxygen vacancies. Moreover from our XPS analysis it was found that the peak position of Zr 3d & O 1s agrees well with the reported values and these corresponds to ZrO_x & ZrO_2 phases. Thus XPS analysis as well as the compositional analysis from the optical density profile index confirms that the principal layer is a mixture of stoichiometric and non-stoichiometric zirconium dioxide. In addition, the optical constant profile of the interfacial layer shows that it is not a mere substrate oxide layer. The profile matches well by taking into a composition of 20% As_2O_3 along with 25% Ga_2O_3 , 35% ZrO_2 and 20% oxygen vacancies.

Appendix

I. Reflection from a homogeneous slab deposited on a substrate²



Schematic diagram of reflection process occurring in a thin film of thickness d deposited on a substrate of semi-infinite thickness

We assume a thin film of thickness d deposited on a substrate of semi-infinite thickness (much higher thickness as compared to the layer thickness). The medium above the film is nothing but air/vacuum whose refractive index can be assumed to be $N=1$ and the layer is designated as 0, whereas the refractive index of the thin film layer is N_f and it is designated as 1 while the substrate is designated as 2 and its refractive index is N_s .

When an electromagnetic wave is incident upon the film surface the following phenomenon occurs in a step by step manner-

- i. As the incident wave strikes the surface of the film, reflection occurs at the interface of 0 to 1. The amplitude of reflection co-efficient can be written as r_{01} . A part of the incident wave is transmitted at the same 0 to 1 interface and the amplitude of the transmission co-efficient is t_{01} .

- ii. The transmitted beam undergoes reflection at the interface of 1 to 2, and a part of it gets transmitted too inside the substrate which does not contribute to the final reflection. The amplitude of reflection is written as $r_{1,2}$.
- iii. The reflected wave will now undergo transmission at the film/air interface and thus the transmission co-efficient can be written as $t_{1,0}$. Interestingly, at this point phase factor is introduced because of the path difference originated due to change of refractive index between the air/film interfaces. The phase factor is designated as $Z = e^{jQd}$ where Q is the momentum transfer along the z -direction of the film and is given by $Q = 2k_z = \frac{4\pi}{\lambda} N \sin\theta$

Thus, the final expression of reflectivity can be written as

$$r_{tot} = r_{0,1} + t_{0,1}r_{1,2}t_{1,0}Z + t_{0,1}r_{1,2}^2r_{1,0}t_{1,0}Z^2 + \dots \dots \dots$$

$$r_{tot} = r_{0,1} + t_{0,1}r_{1,2}t_{1,0}Z\{1 + r_{1,2}Z r_{1,0} + \dots \dots \dots\} = r_{0,1} +$$

$$t_{0,1}r_{1,2}t_{1,0}Z \sum_{m=0}^{\infty} (r_{1,2}Z r_{1,0})^m \quad (1)$$

Using the geometric series we get

$$\therefore r_{tot} = r_{0,1} + \frac{t_{0,1}r_{1,2}t_{1,0}Z}{1 - r_{1,2}Z r_{1,0}} = \frac{r_{0,1}(1 - r_{1,2}Z r_{1,0}) + t_{0,1}r_{1,2}t_{1,0}Z}{1 - r_{1,2}Z r_{1,0}}$$

Using Fresnel's formula for reflection from a single layer we get $r_{0,1} = \frac{Q_0 - Q_1}{Q_0 + Q_1}$ and $t_{0,1} = \frac{2Q_0}{Q_0 + Q_1}$

Thus, the reflection co-efficient from interface 0 to 1 is same as that of 1 to 0 with a negative sign i.e., $r_{0,1} = -r_{1,0}$ (2)

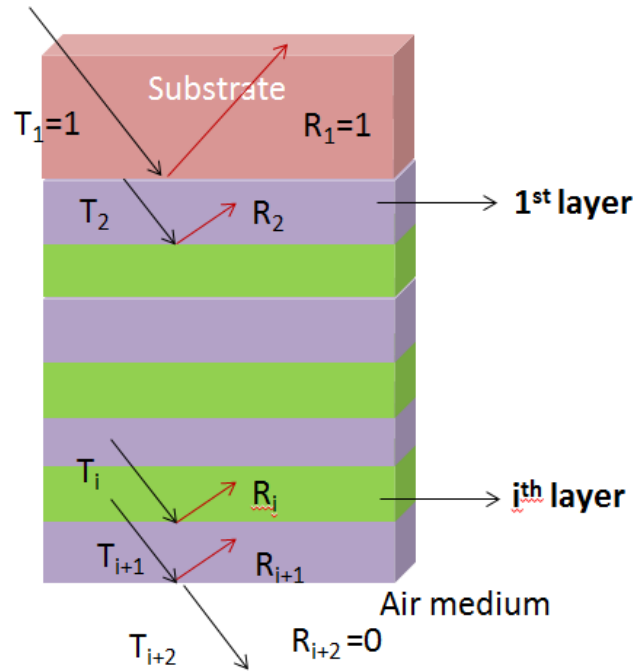
$$\therefore r_{tot} = \frac{r_{0,1} + r_{1,2}Z r_{1,0}^2 + t_{0,1}r_{1,2}t_{1,0}Z}{1 - r_{1,2}Z r_{1,0}}$$

$$= \frac{r_{0,1} + r_{1,2}Z (r_{1,0}^2 + t_{0,1}t_{1,0})}{1 - r_{1,2}Z r_{1,0}}$$

Calculating $(r_{1,0}^2 + t_{0,1}t_{1,0})$ using Fresnel's relation we get it equal to 1.

$$\therefore r_{tot} = \frac{r_{0,1} + r_{1,2}Z}{1 + r_{1,2}Z r_{1,0}} \quad (3)$$

II. Reflection from a multilayer-“Parratt Formalism”⁴⁶



Schematic of multilayer film showing reflected and transmitted amplitudes just above each interface.

We define a i -layer system multilayer film where R and T denotes reflection and transmission respectively. The substrate and the air medium is denoted in the schematic diagram.

Since there is no backscattered wave from air medium at the $i+1^{\text{th}}$ interface, we can write-

$$R_{i+2} = 0 \quad (1)$$

We define $X = R/T$, i.e., ratio of the reflected to transmitted intensity.

$$\therefore X_{i+2} = 0 \quad (2)$$

$$T_{i+2} = T_{i+1}t_{i+1,i+2} \quad (3)$$

$$R_{i+1} = T_{i+1}r_{i+1,i+2} \quad (4)$$

$$X_{i+1} = \frac{R_{i+1}}{T_{i+1}} = r_{i+1,i+2} \quad (5)$$

$$T_{i+1} = T_i t_{i,i+1} e^{j\phi_i} + R_{i+1} e^{2j\phi_N} r_{i+1,i} \quad (6)$$

$$R_i = T_i r_{i,i+1} + R_{i+1} e^{j\phi_i} t_{i+1,i} \quad (7)$$

$$\phi_i = \frac{2\pi}{\lambda} N_i d_i \sin \theta_i \quad (8)$$

where, d_i is the thickness, N_i is the refractive index and θ_i is the incidence angle of the i^{th} layer.

Dividing Eq. (6) by T_{i+1} ,

$$\begin{aligned} 1 &= \frac{T_i}{T_{i+1}} t_{i,i+1} e^{j\phi_i} + \frac{R_{i+1}}{T_{i+1}} e^{2j\phi_i} r_{i+1,i} \\ \Rightarrow \frac{T_{i+1}}{T_i} &= \frac{t_{i,i+1} e^{j\phi_N}}{1 + X_{i+1} r_{i,i+1} e^{2j\phi_i}} \end{aligned} \quad (9)$$

Using the relation $r_{i+1,i} = -r_{i,i+1}$ as derived using Fresnel's formula (shown in earlier section).

Dividing Eq. (6) by T_i ,

$$\frac{T_{i+1}}{T_i} = t_{i,i+1} e^{j\phi_i} + \frac{R_{i+1}}{T_i} e^{2j\phi_i} r_{i+1,i} \quad (10)$$

Equating equations (9) and (10),

$$t_{i,i+1} e^{j\phi_N} + \frac{R_{i+1}}{T_i} e^{2j\phi_i} r_{i+1,i} = \frac{t_{i,i+1} e^{j\phi_i}}{1 + X_{i+1} r_{i,i+1} e^{2j\phi_i}}$$

$$\frac{R_{i+1}}{T_i} = \frac{\frac{t_{i,i+1} e^{j\phi_i}}{1 + X_{i+1} r_{i,i+1} e^{2j\phi_i}} - t_{i,i+1} e^{j\phi_i}}{e^{2j\phi_N} r_{N+1,N} (1 + X_{N+1} r_{N,N+1} e^{2j\phi_N})}$$

$$\frac{R_{i+1}}{T_i} = \frac{t_{i,i+1} e^{j\phi_i} - t_{i,i+1} e^{j\phi_i} (1 + X_{i+1} r_{i,i+1} e^{2j\phi_i})}{e^{2j\phi_i} r_{i+1,i} (1 + X_{i+1} r_{i,i+1} e^{2j\phi_i})}$$

$$\frac{R_{i+1}}{T_i} = \frac{t_{i,i+1} X_{i+1} e^{j\phi_i}}{1 + X_{i+1} r_{i,i+1} e^{2j\phi_i}} \quad (11)$$

Dividing Eq. (7) by T_i ,

$$\frac{R_i}{T_i} = r_{i,i+1} + \frac{R_{i+1}}{T_i} e^{j\phi_i} t_{i+1,i}$$

Replace $\frac{R_{i+1}}{T_i}$ value from Eq. (11)

$$\frac{R_{i+1}}{T_i} = r_{i,i+1} + \frac{t_{i,i+1} X_{i+1} e^{j\phi_i}}{1 + X_{i+1} r_{i,i+1} e^{2j\phi_i}} e^{j\phi_i} t_{i+1,i}$$

$$X_i = r_{i,i+1} + \frac{(1 - r_{i,i+1}^2) X_{i+1} e^{2j\phi_i}}{1 + X_{i+1} r_{i,i+1} e^{2j\phi_i}}$$

where $(t_{i,i+1} t_{i+1,i} + r_{i,i+1}^2 = 1)$

$$X_i = \frac{r_{i,i+1}(1 + X_{i+1} r_{i,i+1} e^{2j\phi_i}) + (1 - r_{i,i+1}^2) X_{i+1} e^{2j\phi_i}}{1 + X_{i+1} r_{i,i+1} e^{2j\phi_i}}$$

$$\Rightarrow X_i = \frac{r_{i,i+1} + X_{i+1} e^{2j\phi_i}}{(1 + X_{i+1} r_{i,i+1} e^{2j\phi_i})}$$

where, ϕ_i is defined earlier.

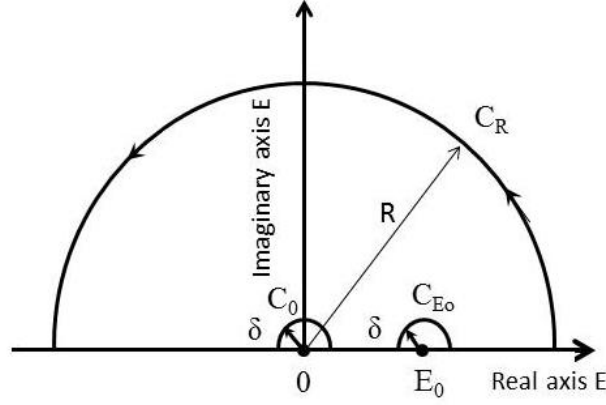
III. Kramers-Kronig relation in reflection mode^{57,59,39}

Refractive index (n) is a function of the angular frequency/energy and it has the following properties-

- 1) It is an analytic response function.
- 2) It does not take any real values at any finite point in the upper half part of the complex frequency plane except on the imaginary axis, where it decreases monotonically from $\epsilon > 1$ at $E = j0$ to 1 at $E = j\infty$.⁵⁹

The next important step is the choice of the kernel and the contour. Nash et al.⁵⁷ have made use of the kernel having the form

$$f(z) = \frac{\ln[r(z)]}{z(z - E_o)}$$



In this approach one calculates the integral I with the consideration of pole at $z=0$:

$$I = \oint \frac{\ln[r(z)]}{z(z - E_o)} dz$$

Within and on the contour as shown in fig. the kernel is analytic and therefore according to Cauchy's integral theorem $I=0$.

The integral can be expressed as:³⁹

$$\begin{aligned} I = & \int_{C_R} \frac{\ln[r(z)]}{z(z - E_o)} dz + \int_{-R}^{-\delta} \frac{\ln[r(E)]}{z(z - E_o)} dE + \int_{+\delta}^{-\delta+E_o} \frac{\ln[r(E)]}{z(z - E_o)} dE \\ & + \int_{\delta+E_o}^R \frac{\ln[r(E)]}{z(z - E_o)} dE + \int_{C_o} \frac{\ln[r(z)]}{z(z - E_o)} dz + \int_{C_{E_o}} \frac{\ln[r(z)]}{z(z - E_o)} dz \end{aligned}$$

From the contour figure it is well evident that the limits R and δ can be easily taken as $R \rightarrow \infty$ & $\delta \rightarrow 0$.

Under this condition the integral

$$I_1 = \int_{C_R} \frac{\ln[r(z)]}{z(z - E_o)} dz \rightarrow 0$$

Moreover, since the kernel is finite in the upper half of the complex energy plane we can write:

$$I_2 + I_3 + I_4 = \int_{C_R} + \int_{-R}^{-\delta} \frac{\ln[r(E)]}{E(E-E_o)} dE + \int_{+\delta}^{-\delta+E_o} \frac{\ln[r(E)]}{E(E-E_o)} dE + \int_{\delta+E_o}^R \frac{\ln[r(E)]}{E(E-E_o)} dE \rightarrow$$

$$P \int_{-\infty}^{+\infty} \frac{\ln[r(E)]}{E(E-E_o)} dE$$

We define

$$I_5 = \int_{C_o} \frac{\ln[r(z)]}{z(z-E_o)} dz = \varphi(E_o) \int_{C_o} \frac{dz}{z} + \int_{C_o} \frac{\varphi(z)-\varphi(0)}{z}$$

Using $z = \delta \exp(j\theta)$ in the first integral of the above equation and integrating with θ as a variable from π to 0 gives:

$$I_5 = -i\varphi(0)\pi + \int_{C_o} \frac{\tau(z) - \tau(0)}{z}$$

Since $\tau(z)$ is continuous at $z=0$, which means that for all $\varepsilon > 0$ there exists a value η such that if $|z| < \eta$, then $|\tau(z) - \tau(0)| < \eta$, thus we get-

$$\left| \int_{C_o} \frac{\tau(z) - \tau(0)}{z} dz \right| \leq \frac{\varepsilon}{\eta} \left| \int_{C_o} \frac{dz}{z} \right| = \frac{\varepsilon}{\eta} \pi \sigma = \varepsilon$$

which means that it can be made smaller than any pre-assigned number.

$$I_5 = j \frac{\ln[r(0)]}{E_o} \pi$$

Similarly, defining $I_6 = \int_{C_{E_o}} \frac{\ln[r(z)]}{z(z-E_o)} dz = -j \frac{\ln[r(E_o)]}{E_o} \pi$

Thus $I = I_1 + I_2 + I_3 + I_4 + I_5 + I_6$

$$I = P \int_{-\infty}^{+\infty} \frac{\ln[r(E)]}{E(E-E_o)} dE + j \frac{\ln[r(0)]}{E_o} \pi - j \frac{\ln[r(E_o)]}{E_o} \pi = 0$$

Taking real part of the above equation we get:

$$Im[\ln[r(E_o)]] = Im[\ln[r(0)]] - \frac{2E_o}{\pi} P \int_0^{+\infty} \frac{Re[\ln[r(E)]]}{E^2 - E_o^2} dE$$

IV. Derivation of optical constants from energy-dependent reflectivity spectrum¹⁸³

The complex reflection coefficient in term of reflectivity and phase is represented by

$$r(E) = \sqrt{R(E)}e^{-j\varphi(E)} \quad (1)$$

Here $r(E)$, R , $\varphi(E)$ is the reflection co-efficient, reflectivity and phase of the reflected electric field respectively.

Fresnel reflection coefficient for s polarized radiation can be written as-

$$r_s = B = \frac{\sin\theta - \sqrt{N^2 - \cos^2\theta}}{\sin\theta + \sqrt{N^2 - \cos^2\theta}} \quad (2)$$

Here θ , N is the grazing incident angle and complex refractive index respectively.

Substitute $N^2 - \cos^2\theta = A$ in eq. (2).

$$B = \frac{\sin\theta - \sqrt{A}}{\sin\theta + \sqrt{A}} \quad (3)$$

$$\sqrt{A} = \frac{\sin\theta(1-B)}{(1+B)} \quad (4)$$

Substitute the value of A in eq. 4

$$N^2 - \cos^2\theta = \frac{\sin^2\theta(1+B^2-2B)}{(1+B^2+2B)}$$

$$N^2 = \frac{(1+B^2+2B\cos 2\theta)}{(1+B^2+2B)} \quad (5)$$

Substitute the value of B from eq. (1) to eq. (5)

$$N^2 = \frac{(1 + R.e^{-2j\phi(E)} + 2.\sqrt{R}e^{-j\phi(E)}. \cos 2\theta)}{(1 + R.e^{-2j\phi(E)} + 2\sqrt{R}.e^{-j\phi(E)})} \quad (6)$$

$$N^2 = \frac{(1 + R \cos 2\phi(E) + 2\sqrt{R} \cos \phi(E). \cos 2\theta) - j(R \sin 2\phi(E) + 2\sqrt{R} \sin \phi(E). \cos 2\theta)}{(1 + R \cos 2\phi(E) + 2\sqrt{R} \cos \phi(E)) - j(R \sin 2\phi(E) + 2\sqrt{R} \sin \phi(E))} \quad (7)$$

Substitute $N = (1 - \delta) + i\beta$ in eq. (7)

$$\begin{aligned} & (1 - \delta)^2 - \beta^2 \\ &= \frac{(1 + R \cos 2\phi(E) + 2\sqrt{R} \cos \phi(E). \cos 2\theta).(1 + R \cos 2\phi(E) + 2\sqrt{R} \cos \phi(E)) + (R \sin 2\phi(E) + 2\sqrt{R} \sin \phi(E). \cos 2\theta).(R \sin 2\phi(E) + 2\sqrt{R} \sin \phi(E))}{(1 + R \cos 2\phi(E) + 2\sqrt{R} \cos \phi(E))^2 + (R \sin 2\phi(E) + 2\sqrt{R} \sin \phi(E))^2} \end{aligned} \quad (8)$$

$$\begin{aligned} & 2\delta\beta \\ &= \frac{(R \sin 2\phi(E) + 2\sqrt{R} \sin \phi(E) \cos 2\theta).(1 + R \cos 2\phi(E) + 2\sqrt{R} \cos \phi(E)) - (1 + R \cos 2\phi(E) + 2\sqrt{R} \cos \phi(E) \cos 2\theta).(R \sin 2\phi(E) + 2\sqrt{R} \sin \phi(E))}{(1 + R \cos 2\phi(E) + 2\sqrt{R} \cos \phi(E))^2 + (R \sin 2\phi(E) + 2\sqrt{R} \sin \phi(E))^2} \end{aligned} \quad (9)$$

By solving eq.(8) and (9)

$$(1 - \delta)^2 - \beta^2 = \left[\frac{1 + R^2 + (4R \cos(2\theta)) + (2R \cos(2\phi(E))) + 4\sqrt{R} \cos \phi(E) \cos^2(\theta)(1 + R)}{1 + R^2 + 4R + 2R \cos(2\phi(E)) + 4\sqrt{R} \cos \phi(E)(1 + R)} \right] \quad (10)$$

$$2(1 - \delta)\beta = \left[\frac{4\sqrt{R} \sin \phi(E) \sin^2(\theta)(1 - R)}{1 + R^2 + 4R + 2R \cos(2\phi(E)) + 4\sqrt{R} \cos(\phi(E))(1 + R)} \right] \quad (11)$$

Let us assume,

$$\frac{1 + R^2 + 2R \cos(2\phi(E)) + 4R \cos 2\theta + 4\sqrt{R} \cos \phi(E) \cos^2(\theta)(1 - R)}{1 + R^2 + 4R + 2R \cos(2\phi(E)) + 4\sqrt{R} \cos(\phi(E))(1 + R)} = p$$

$$\frac{4\sqrt{R} \sin \phi(E) \sin^2(\theta)(1 - R)}{1 + R^2 + 4R + 2R \cos(2\phi(E)) + 4\sqrt{R} \cos(\phi(E))(1 + R)} = q$$

And putting these in eq. (10) and (11) respectively we get,

$(1 - \delta)^2 - \beta^2 = p$ and $2(1 - \delta)\beta = q$ by solving these equations

$$(1 - \delta)^2 = \frac{p + \sqrt{p^2 + q^2}}{2} \text{ and } (1 - \delta)^2 = \frac{p - \sqrt{p^2 + q^2}}{2} \quad (12)$$

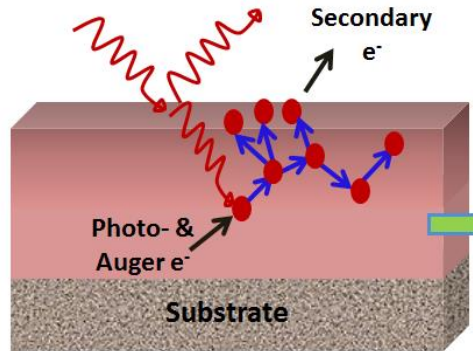
$$\beta = \frac{q}{(1 - \delta)} \quad (13)$$

Equation (12) and (13) is used for determination optical constants.

V. Derivation of Total electron yield (TEY)^{66,180,181}

Now, we will derive the expression for the yield signal assuming different models that we have used in this thesis-

Assuming the contribution of the secondary electrons only



In this case one assumes that the primary electron does not contribute to the yield signal since the secondary electrons are created just at the point of creation of the primary electron due to the photon absorption process.

If R is the reflection coefficient, then the intensity of photons transmitted inside the sample is given as $-I_{ts} = [1 - R(\varphi)]I_o$ where, I_o is the intensity of the incident X-ray photon.

Thus, the probability of the absorption of the transmitted X-ray photon in a layer of differential thickness dz at a distance z from the sample surface is –

$$[1 - R(\varphi)]\mu' \exp(-\mu' z) dz \quad (1)$$

Where $\mu' = \frac{\mu}{\sin\varphi'}$, μ is the linear absorption co-efficient and φ' is the angle of refraction.

If $E = h\nu$ is the energy of the incident photon and e is the required energy to create one secondary electron which overcome the barrier and gets collected contributing to the yield signal, then the number of secondary electrons created in the layer of differential thickness dz is-⁶⁶

$$N(z)dz = [1 - R(\varphi)]\mu' \exp(-\mu' z) \frac{h\nu}{e} dz \quad (2)$$

All the created secondary electron does not have the capability to overcome the surface barrier and contribute to the yield signal. Several factors are associated with the transmission of the created secondary electron into the vacuum. We define an escape function $L(z)$, which is nothing but the probability of the electrons collected by the electrometer. The choice of an escape function is a difficult task since various factors like multiple electron scattering resulting in electron loss, angular distribution of the created secondary electrons, change in potential barrier at the interface of the sample layers, refraction effects etc. contribute to its form. However, for simplicity we can ignore those effects and write the escape function as-

$$L(z) \propto \int_0^{2\pi} d\varphi \int_0^{\pi/2} \exp\left(-\frac{z}{\lambda_e \cos\psi}\right) \sin\psi d\psi = B \exp\left(-\frac{z}{\lambda_e}\right) \quad (3)$$

Where, λ_e is the escape depth of the secondary electrons and B is the escape probability of the electrons from the surface of the sample.

Thus, the total yield signal collected from the sample can be expressed as-

$$Y = \int_0^d N(z)F(z)dz = [1 - R(\varphi)] \frac{h\nu}{e} B \int_0^d \mu' \exp(-\mu'z) \exp\left(-\frac{z}{\lambda_e}\right) dz$$

The advantage of this model to explain the yield signal is its simplicity, though it fails to explain most of the time since the yield signal not only consists of the secondary electrons, Auger electrons & the primary electrons also contribute to the yield signal directly. Moreover, the generation of the secondary electron does not occur just at the point of creation of primary electron. The created primary electron traverses a certain distance in the sample and undergoes ionization with the other electrons present in the sample, resulting in the generation of secondary electrons along the track of the primary electron only.

Assuming the different contribution of the electrons from different absorption processes

The total electron yield signal can be written as-

$$Y = \int_0^d N(z)L(z)dz$$

Where $L(z)$ is the escape function, which can be expressed in exponential form as shown earlier & $N(z)$ is the number of electrons created at depth z as a result of absorption of X-ray photon. From the perspective of the two different absorption processes, we have to redefine the expression of $N(z)$.

According to electromagnetic theory, the general conservation law can be written as-

$$\text{div } \vec{S} + \frac{\partial u}{\partial t} = -Q \quad (1)$$

Where \vec{S} the Poynting vector averaged over time, u is the density of the electromagnetic energy & Q is the energy loss in unit volume at unit time.

In case of soft X-ray region, the energy loss factor Q determines the photon absorption and thus tells about the number of electrons created at a depth z , thus $N(z) \propto \tau Q$ (2)

where τ is a constant parameter determining the number of photoelectrons for one absorbed photon.

$$Q \propto \text{Imag}(\chi)|E|^2 \quad (3)$$

Where, χ is the electric susceptibility and E is the electric field or the X-ray field amplitude which is a function of depth, incidence angle and energy of the incident photon E_{ph} .^{180,181}

Thus, $N(z) \propto \tau Q \propto \epsilon |E|^2 = \frac{1}{\lambda} \epsilon |E|^2$, where the term $\frac{1}{\lambda}$ denotes that with increasing energy the number of created electrons will also increase because of higher penetration depth.

Relation between susceptibility and dielectric constant is- $\chi = \epsilon - 1$, where $\chi = \chi_1 + j\chi_2$ and $\epsilon = \epsilon_1 + j\epsilon_2$, χ_1 & χ_2 are the real and imaginary part of susceptibility and ϵ_1 & ϵ_2 are that of dielectric constant.

We get, $\chi_1 = \epsilon_1 - 1$ and $\chi_2 = \epsilon_2$. We can also represent dielectric constant in terms of refractive index $N=(1-\delta)+i\beta$ as- $\epsilon = N^2$

$$\text{Thus } \epsilon_2 = \chi_2 = 2(1 - \delta)\beta$$

Taking into account the contribution of different number of registered electrons originating from two different absorption processes we can express $N(z)$ as¹⁸¹-

$$N(z) = \left(\tau_{nres} \frac{2(1-\delta)\beta}{\lambda} |E(z, E_{ph}, \theta)|^2 + \tau_{res} \frac{2(1-\delta_{res})\beta_{res}}{\lambda} |E(z, E_{ph}, \theta)|^2 \right) \quad (4)$$

Deriving the expression of $Y(E_{ph}, \theta)$

We can write-

$$|E(z, E_{ph}, \theta)|^2 = |E_o + E_R|^2 e^{-\mu z} \quad (5)$$

E_o is the electric field of the incident photon, E_R is the electric field of the reflected photon and μ is the absorption co-efficient. The internal electric field is the superposition of the incident field and the reflected field which resultantly forms standing waves. The effect of E_R is higher at glancing angles only. The exponential term represents the fact that the field decays simultaneously because of X-ray absorption by the sample.

$$|E(z, E_{ph}, \theta)|^2 = |E_o|^2 \left| 1 + \frac{E_R}{E_o} \right|^2 e^{-4\pi\beta/\lambda z} \quad (6)$$

Where $\mu = 4\pi\beta/\lambda$, β being the imaginary part of the optical constant. The term $\frac{E_R}{E_o}$ is the reflection co-efficient which can be written according to Fresnel's formula as

$$\frac{E_R}{E_o} = \frac{\sin\theta - \sqrt{N^2 - \cos^2\theta}}{\sin\theta + \sqrt{N^2 - \cos^2\theta}}. \text{ Thus, we define } E_f = \left| E_o + \frac{\sin\theta - \sqrt{N^2 - \cos^2\theta}}{\sin\theta + \sqrt{N^2 - \cos^2\theta}} E_o \right|^2$$

Thus,

$$Y = \int_0^d N(z) L(z) dz$$

$$= \int_0^d \left(\tau_{nres} \frac{2(1-\delta)\beta}{\lambda} + \tau_{res} \frac{2(1-\delta_{res})\beta_{res}}{\lambda} \right) E_f e^{-4\pi\beta/\lambda z} \exp\left(-\frac{z}{\lambda_e}\right) dz$$

We rewrite δ_{res} as δ_{KK} and β_{res} as β_{KK} since we determined the optical constants near the edge region where resonant phenomena is dominant by performing energy dependent reflectivity measurement and applying KK relation to find the phase.

$$\therefore Y = \left(\tau_{nres} \frac{2(1-\delta)\beta}{\lambda} + \tau_{res} \frac{2(1-\delta_{KK})\beta_{KK}}{\lambda} \right) E_f \frac{\lambda_e}{\lambda_e + \beta\lambda_e} \times \left[1 - \exp\left\{\left(-\beta + \frac{1}{\lambda_e}\right) d\right\} \right]$$

Bibliography

- ¹ D. Attwood, “Soft X-rays and Extreme Ultraviolet Radiation” Cambridge University Press, Cambridge, UK, (1999).
- ² Jens Als-Nielsen and Des McMorrow, “Elements of Modern X-ray Physics” Second edition, John Wiley and sons Inc. (2011)
- ³ R Soufli Ph.D. Thesis “Optical Constants of Materials in the EUV/Soft X-ray Region for Multilayer Mirror Applications” Submitted to Ernest Berkeley Orlando Lawrence National Laboratory 1997
- ⁴ B. L. Henke, E. M. Gullikson, and J. C. Davis, “X-ray Interactions: Photoabsorption, Scattering, Transmission, and Reflection at $E = 50\text{--}30,000$ eV, $Z = 1\text{--}92$ ” *At. Data Nucl. Data Tables* **54**, 181–342 (1993).
- ⁵ C. M. Herzinger, B. Johs, W. A. Mc Gahan, J. A. Woollam, and W. Paulson, “Ellipsometric determination of optical constants for silicon and thermally grown silicon dioxide via a multi-sample, multi-wavelength, multi-angle investigation”, *J. Appl. Phys.* **83**, 3323–3336 (1998)
- ⁶ R.A. Synowicki and Thomas E. Tiwald, “Optical properties of bulk c-ZrO₂, c-MgO and a-As₂S₃ determined by variable angle spectroscopic ellipsometry”, *Thin Solid Films* **455–456**, 248–255 (2004).
- ⁷ Denis Joyeux, François Polack, and Daniel Phalippou, “An interferometric determination of the refractive part of optical constants for carbon and silver across soft X-ray absorption edges”, *Rev. Sci. Instr.* **70**, 2921–2926 (1999).
- ⁸ Regina Soufli and Eric M. Gullikson, “Reflectance measurements on clean surfaces for the determination of optical constants of silicon in the extreme ultraviolet–soft-X-ray region”, *Appl. Optics* **36**, 5499–5507 (1997).
- ⁹ Charles Tarrio, Richard N. Watts, Thomas B. Lucatorto, Jon M. Slaughter, and Charles M. Falco, “Optical constants of in situ-deposited films of important extreme-ultraviolet multilayer mirror materials”, *Appl. Optics* **37**, 4100–4104 (1998).
- ¹⁰ Regina Soufli and Eric M. Gullikson, “Absolute photoabsorption measurements of molybdenum in the range 60–930 eV for optical constant determination”, *Appl. Optics* **37**, 1713–1719 (1998).
- ¹¹ E. M. Gullikson, P. Denham, S. Mrowka, and J. H. Underwood, “Absolute photoabsorption measurements of Mg, Al, and Si in the soft-X-ray region below the L_{2,3} edges”, *Phys. Rev. B* **49**, 16283–16288 (1994).
- ¹² Jean Daillant and Alain Gibaud, “X-ray and Neutron Reflectivity: Principles and Applications” Springer-Verlag Berlin Heidelberg (2009).
- ¹³ Ullrich Pietsch, Vaclav Holy and Tilo Baumbach, “High-Resolution X-ray Scattering: From Thin films to Lateral Nanostructures” Springer-Verlag New York, Second edition (2004).
- ¹⁴ David L. Windt, Webster C. Cash, Jr., M. Scott, P. Arendt, B. Newnam, R. F. Fisher, and A. B. Swartzlander, “Optical constants for thin films of Ti, Zr, Nb, Mo, Ru, Rh, Pd, Ag, Hf, Ta, W, Re, Ir, Os, Pt, and Au from 24 Å to 1216 Å”, *Appl. Optics* **27**, 246–278 (1988).
- ¹⁵ Luis V. Rodríguez-de Marcos, Juan I. Larruquert, José A. Méndez, and José A. Aznárez, “Self-consistent optical constants of SiC thin films”, *Opt. Mat. Express* **6**, 3622–3637 (2016).
- ¹⁶ Y. Lifshitz, G. D. Lempert, E. Grossman, H. J. Scheibe, S. Voellmar, B. Schultrich, A. Breskin, R. Chechik, E. Shefer, D. Bacon, R. Kalish, and A. Hoffman, “Optical and photoemission studies of DLC films prepared with a systematic variation of the sp³:sp² composition”, *Diamond and Rel. Materials* **6**, 687–693 (1997).
- ¹⁷ Yuhong Cao, Ertao Hu, Jie Xing, Li Liu, Tong Gu, Jiajin Zheng, Kehan Yu, and Wei Wei, *Opt. Mat. Exp.* **9**, 234–243 (2019).
- ¹⁸ Amol Singh, Mohammed H. Modi, Parasmani Rajput, A. K. Sinha, and G. S. Lodha, “Influence of structural disorder on soft X-ray optical behavior of NbC thin films”, *J. Appl. Phys.* **117**, 175301 (1–7) (2015)
- ¹⁹ M. S. Dresselhaus, “Optical Properties of Solids”, *Solid State Physics, Part 2*, MIT Course lecture.
- ²⁰ Sokrates T. Pantelides, “Theory of core excitons in semiconductors”, *Solid State Comm.* **16**, 217–220 (1975).
- ²¹ F. Bassani, “Core excitons in solids”, *Appl. Optics* **19**, 4093–4100 (1980).
- ²² Harold P. Hjalmarson, Helmut Buttner and John D. Dow, “Theory of core excitons”, *Phys. Rev B* **24**, 6010–6019 (1981).
- ²³ Mangalika Sinha, Saurabh Sharma, Amol Singh, and M. H. Modi, “Optical constants of off-stoichiometric aluminum oxide thin film in 6–20 nm soft-X-ray/extreme ultraviolet region”, *Jpn. J. Appl. Phys.* **55**, 101101(1–5) (2016).
- ²⁴ S. Ben Amor, B. Rogier, G. Baud, M. Jacquet, and M. Nardin, “Characterization of zirconia films deposited by r.f. magnetron sputtering”, *Materials Science and Engineering* **B57**, 28–39 (1998).

- ²⁵ Pengtao Gao, L. J Meng, M. P dos Santos, V. Teixeira, and M. Andritschky, “Characterisation of ZrO₂ films prepared by rf reactive sputtering at different O₂ concentrations in the sputtering gases”, *Vacuum* **56**, 143-148 (2000).
- ²⁶ S. Venkataraj, Oliver Kappertz, Hansjörg Weis, Robert Drese, R. Jayavel, and Matthias Wuttig, “Structural and optical properties of thin zirconium oxide films prepared by reactive direct current magnetron sputtering”, *J. Appl. Phys.* **92**, 3599-3607 (2002).
- ²⁷ Regina Soufli, Andrew L. Aquila, Farhad Salmassi, Mónica Fernández-Perea, and Eric M. Gullikson, “Optical constants of magnetron-sputtered boron carbide thin films from photoabsorption data in the range 30 to 770 eV”, *Appl. Optics* **47**, 4633-4639 (2008).
- ²⁸ E O Filatova, A A Sokolov, I V Kozhevnikov, E Yu Taracheva, O S Grunsky, F Schaefer and W Braun, “Investigation of the structure of thin HfO₂ films by soft X-ray reflectometry techniques”, *J. Phys.: Condens. Mat.* **21**, 185012 (1-7) (2009).
- ²⁹ Ian W. Hamley and Jan Skov Pedersen, “Analysis of neutron and X-ray reflectivity data. I. Theory”, *J. Appl. Cryst.* **27**, 29-35 (1994).
- ³⁰ H. Zabel, “X-ray and neutron reflectivity analysis of thin films and superlattices”, *Appl. Phys. A* **58**, 159-168 (1994).
- ³¹ Pragma Tripathi, GS Lodha, MH Modi, AK Sinha, KJS Sawhney, RV Nandedkar, “Optical constants of silicon and silicon dioxide using soft X-ray reflectance measurements”, *Optics Communications* **211**, 215-223 (2002).
- ³² Amol Singh, Mohammed H Modi, G. S Lodha, “Optical constants of zirconium carbide in 60–200 Å wavelength region using X-ray reflectivity technique”, *Appl. Optics* **54**, 253-258 (2015).
- ³³ Amol Singh, Mangalika Sinha, R .K Gupta, Mohammed H Modi, “Optical constants of e-beam-deposited zirconium dioxide measured in the 55–150 Å wavelength region using the reflectivity technique”, *Appl. Optics* **55**, (2016).
- ³⁴ M. K. Sanyal, S. K. Sinha, A. Gibaud, K. G. Huang, B. L. Carvalho, M. Rafailovich, J. Sokolov, X. Zhao and W. Zhao, “Fourier Reconstruction of Density Profiles of Thin Films Using Anomalous X-ray Reflectivity”, *Euro Phys. Lett.* **21**, 691-696 (1993).
- ³⁵ Klaus Martin Zimmermann, Ph.D Thesis “Advanced analysis techniques for X-ray reflectivities: Theory and application” Submitted to Universität Dortmund, Kalrusche (2005).
- ³⁶ E. Filatova, V. Lukyanov, R. Barchewitz, J-M André, M. Idir, and Ph. Stemmler, “Optical constants of amorphous for photons in the range of 60-3000 eV”, *J. Phys. Condens. Matter* **11**, 3355-3370 (1999).
- ³⁷ E Filatova and Andrey Sokolov, “Effect of reflection and refraction on NEXAFS spectra measured in TEY mode”, *J. Synchrotron Rad.* **25**, 232-240 (2018).
- ³⁸ D. B. Tanner, “Use of X-ray scattering functions in Kramers-Kronig analysis of reflectance”, *Phys. Rev. B* **91**, 035123 (1-12) (2015).
- ³⁹ Jean-Michel André, Karine Le Guen, Philippe Jonnard, Nicola Mahne, Angelo Giglia, Stefano Nannarone, “On the Kramers-Kronig transform with logarithmic kernel for thereflection phase in the Drude model”, *J. Mod. Optics* **57**, 1504–1512 (2010).
- ⁴⁰ Mangalika Sinha, Mohammed H Modi, Haranath Ghosh, P. K Yadav, R. K Gupta, “Influence of the core-hole effect on optical properties of magnesium oxide (MgO) near the Mg L-edge region”, *J. Synchrotron Rad.* **25**, 771-776 (2018).
- ⁴¹ A. Gibaud, and S. Hazra, “X-ray reflectivity and diffuse scattering “, *Current Science* **78**, 1467–1477 (2000).
- ⁴² S. K. Sinha, E.B.Sirota, and S. Garoff, and H. B.Stanley, “X-ray and neutron scattering from rough surfaces”, *Phys. Rev. B* **38**, 2297-2311 (1988).
- ⁴³ J. D. Jackson, “Classical Electrodynamics” Wiley, New York NY, USA, 3rd edition, (1998).
- ⁴⁴ L. Nénot and P. Croce, “Caractérisation des surfaces par réflexion rasante de rayons X. Application à l'étude du polissage de quelques verres silicates”, *Rev. Phys. Appl.* **15**, 761-779 (1980).
- ⁴⁵ E. Spiller, “Soft X-ray optics” (SPIE, Bellingham, WA, USA) (1994).
- ⁴⁶ L.G. Parratt, “Surface Studies of Solids by Total Reflection of X-rays”, *Phys. Rev.* **95**, 359-369 (1954).
- ⁴⁷ F. Abeles, “Recherches sur la propagation des ondes électromagnétiques sinusoïdales dans les milieux stratifiés”, *Ann. Physique (Paris)* **12**, 596–640 (1950).
- ⁴⁸ A. Nelson, “Co-refinement of multiple-contrast neutron/X-ray reflectivity data using MOTOFIT”, *J. App. Cryst.* **39**, 273-276 (2006).
- ⁴⁹ M. H. Modi, G. S. Lodha, P. Mercere, and M. Idir, “Live simulator and data analysis tool for multilayer reflectivity using LABVIEW”, Presented at 9th Int. Conf. Physics of X-ray Multilayer Structures, 2008.

- ⁵⁰ M. H. A. Kramers, “La diffusion de la lumière par les atomes”, Atti Cong. Intern. Fisici, (Transactions of Volta Centenary Congress) Como. **2**, 545–557 (1927).
- ⁵¹ R. de L. Kronig, “On the theory of dispersion of X-rays”, J. Opt. Soc. Am. **12**, 547–557 (1926).
- ⁵² John S. Toll, “Causality and the Dispersion Relation: Logical Foundations”, Phys. Rev. **104**, 1760–1770 (1956).
- ⁵³ K. E. Peiponen, E. M. Vartiainen, and T. Asakura, “Dispersion, Complex Analysis and Optical Spectroscopy”, Springer (1999).
- ⁵⁴ D. M. Roessler, “Kramers-Kronig analysis of reflection data”, Brit. J. Appl. Phys. **16**, 1119–1123 (1965).
- ⁵⁵ B. Velický, “Dispersion Relation for Complex Reflectivity”, Czech J. Phys. B **11**, 542–543 (1961).
- ⁵⁶ G. H. Goedecke, “Dispersion relations and complex reflectivity”, J. Opt. Soc. Am. **65**, 146–149 (1975).
- ⁵⁷ P. L. Nash, “On the Kramers-Kronig Relation for the Phase Spectrum”, J. Mod. Optics **42**, 1837–1842 (1995).
- ⁵⁸ T. S. Robinson and W. C. Price, “The Determination of Infra-Red Absorption Spectra from Reflection Measurements”, Proceedings of the Physical Society of London Section **B66**, 969–974 (1953).
- ⁵⁹ J. S. Plaskett and P. N. Schatz, “On the Robinson and Price (Kramers—Kronig) Method of Interpreting Reflection Data Taken through a Transparent Window”, J. Chem. Phys. **38**, 612–617 (1963).
- ⁶⁰ Frank de Groot and Akio Kotani, “Core Level Spectroscopy of Solids”, CRC Press, Taylor & Francis Group (2008).
- ⁶¹ Joachim Stöhr, “NEXAFS Spectroscopy”, Springer Series in Surface Science, Springer New York (1996).
- ⁶² W. Gudat, and C. Kunz, “Close Similarity between Photoelectric Yield and Photoabsorption Spectra in the Soft-X-ray Range”, Phys. Rev. Lett. **29**, 169–172 (1972).
- ⁶³ B. L. Henke, “Ultrasoft-X-ray Reflection, Refraction, and Production of Photoelectrons (100–1000-eV Region)”, Phys. Rev. A, **6**, 94–104 (1972).
- ⁶⁴ A. J. Achkar, T. Z. Regier, E. J. Monkman, K. M. Shen and D. G. Hawthorn, “Determination of total X-ray absorption coefficient using non-resonant X-ray emission”, Sci. Rep. **1**, 182 (1–7) (2011).
- ⁶⁵ S. V. Pepper, “Optical Analysis of Photoemission”, J. Opt. Soc. Am. **60**, 805–812 (1970).
- ⁶⁶ V. N. Shchemelev and E. P. Savinov, “Total quantum-current yield in the soft X-ray region”, Phys. Solid State **40**, 952–955 (1988).
- ⁶⁷ Burton L. Henke, Jerel A. Smith, and David T. Attwood, “0.1–10-keV x-ray-induced electron emissions from solids—Models and secondary electron measurements”, J. Appl. Phys. **48**, 1852–1866 (1977).
- ⁶⁸ Bradley H. Frazer, Benjamin Gilbert, Brandon R. Sonderegger, Gelsomina De Stasio, “The probing depth of total electron yield in the sub-keV range: TEY-XAS and X-PEEM”, Surf. Sci. **537**, 161–167 (2003).
- ⁶⁹ A. Erbil, G. S. Cargill III, R. Frahm, R. F. Boehme, “Total-electron-yield current measurements for near-surface extended X-ray-absorption fine structure”, Phys. Rev. B **37**, 2450–2464 (1988).
- ⁷⁰ H. Henneken, F. Scholze, and G. Ulm, “Lack of proportionality of total electron yield and soft X-ray absorption coefficient”, J. Appl. Phys. **87**, 257–268 (2000).
- ⁷¹ R. Z. Bachrach and F. C. Brown, “Exciton-optical properties of TiBr and TiCl”, Phys. Rev. B **1**, 818–831 (1970).
- ⁷² K. F. Palmer, M. Z. Williams, and B. A. Budde, “Multiply subtractive Kramers–Kronig analysis of optical data”, Appl. Opt. **37**, 2660–2673 (1998).
- ⁷³ V. Lucarini, J. J. Saarinen, K.-E. Peiponen, and E. M. Vartiainen, “Kramers-Kronig Relations in Optical Materials Research”, Springer (2005).
- ⁷⁴ Hongping Yan, Cheng Wang, Allison R. McCarn, and Harald Ade, “Accurate and Facile Determination of the Index of Refraction of Organic Thin Films Near the Carbon 1s Absorption Edge”, Phys. Rev. Lett. **110**, 177401(1–5) (2013).
- ⁷⁵ http://henke.lbl.gov/optical_constants/
- ⁷⁶ E. Allaria, C. Callegari, D. Cocco, W. M. Fawley, M. Kiskinova, C. Masciovecchio, and F. Parmigiani, “The FERMI@Elettra free-electron-laser source for coherent X-ray physics: photon properties, beam transport system and applications”, New. J. Phys. **12**, 075002 (1–17) (2010).
- ⁷⁷ A. R. Khorsand, R. Sobierajski, E. Louis, S. Bruijn, E. D. van Hattum, R. W. E. van de Kruijs, M. Jurek, D. Klinger, J. B. Pelka, L. Juha, T. Burian, J. Chalupsky, J. Cihelka, V. Hajkova, L. Vysin, U. Jastrow, N. Stojanovic, S. Toleikis, H. Wabnitz, K. Tiedtke, K. Sokolowski-Tinten, U. Shymanovich, J. Krzywinski, S. Hau-Riege, R. London, A. Gleeson, E. M. Gullikson, and F. Bijkerk, “Single shot damage mechanism of Mo/Si multilayer optics under intense pulsed XUV-exposure”, Opt. Express **18**, 700–712 (2010).
- ⁷⁸ F. Barkusky, A. Bayer, S. Döring, P. Grossmann, and K. Mann, “Damage threshold measurements on EUV optics using focused radiation from a table-top laser produced plasma source”, Opt. Express **18**, 4346–4355 (2010).

- ⁷⁹ M. Barthelmess and S. Bajt, "Thermal and stress studies of normal incidence Mo / B 4 C multilayers for a 6.7 nm wavelength", *Appl. Opt.* **50**, 1610- 1619 (2011).
- ⁸⁰ M.H. Modi, M. Nayak, G.S. Lodha, A.K. Sinha, R.V. Nandedkar, "Determination of layer structure in Mo/Si multilayers using soft X-ray reflectivity", *Physica B* **325**, 272-280 (2003).
- ⁸¹ Mohammed H. Modi, S. K. Rai, Mourad Idir, F. Schäfers, G. S. Lodha, "NbC/Si multilayer mirror for next generation EUV light sources", *Opt Express* **20**, 15114-15120 (2012).
- ⁸² R. Sobierajski, S. Bruijn, A. R. Khorsand, E. Louis, R. W. E. van de Kruijs, T. Burian, J. Chalupsky, J. Cihelka, A. Gleeson, J. Grzonka, E. M. Gullikson, V. Hajkova, S. Hau-Riege, L. Juha, M. Jurek, D. Klinger, J. Krzywinski, R. London, J. B. Pelka T. Płociński, M. Rasiński, K. Tiedtke, S. Toleikis, L. Vysin, H. Wabnitz, and F. Bijkerk, "Damage mechanisms of MoN/SiN multilayer optics for next-generation pulsed XUV light sources", *Opt. Express* **19**, 193-205 (2011).
- ⁸³ W. de la Cruz , G. Soto and F. Yubero, "Beryllium nitride: an alternative material to beryllium for extreme ultraviolet and soft X-ray uses", *Optical Materials* **25**, 39-42 (2004).
- ⁸⁴ M. Mayer, C. Grévent, A. Szeghalmi, M. Knez, M. Weigand, S. Rehbein, G. Schneider, B. Baretzky & G. Schütz, "Multilayer Fresnel zone plate for soft X-ray microscopy resolves sub-39 nm structures", *Ultramicroscopy* **111**, 1706-1711 (2011).
- ⁸⁵ Umut Tunca Sanli, Chengge Jiao, Margarita Baluktsian, Corinne Grévent, Kersten Hahn, Yi Wang, Vesna Srot, Gunther Richter, Iuliia Bykova, Markus Weigand, Gisela Schütz, and Kahraman Keskinbora, "3D Nanofabrication of High-Resolution Multilayer Fresnel Zone Plates", *Adv. Sci.* **5**, 1800346 (1-12) (2018).
- ⁸⁶ M. Reese, B. Schäfer. P. Großmann, A. Bayer, K. Mann, T. Liese, and H. U. Krebs, "Submicron focusing of XUV radiation from a laser plasma source using a multilayer Laue lens", *Appl. Phys. A* **102**, 85-90 (2011).
- ⁸⁷ T. Liese, V. Radisch, I. Knorr, M. Reese, P. Großmann, K. Mann, H. Krebs, "Development of laser deposited multilayer zone plate structures for soft X-ray radiation", *Appl. Surf. Sci.* **257**, 5138- 5141 (2011).
- ⁸⁸ S. Bajt, N.V. Edwards, and T. E. Madey, "Properties of ultrathin films appropriate for optics capping layers exposed to high energy photon irradiation", *Surf. Sci. Rep.* **63**, 73-100 (2008).
- ⁸⁹ S. Vitta, M. Weisheit, and H. Krebs, "Structure and scattering properties of Ni₈₀Nb₂₀-MgO water-window multilayer mirrors", *Appl. Opt.* **42**, 3297-3304 (2003).
- ⁹⁰ C. Fuhse, H. Krebs, S. Vitta & G. A. Johansson, "Interface quality and thermal stability of laser-deposited metal/MgO multilayers", *Appl. Opt.* **43**, 6265-6269 (2004).
- ⁹¹ Mónica Fernández-Perea, Regina Soufli, Jeff C. Robinson, Luis Rodríguez-De Marcos, Jose A. Méndez, Juan I. Larruquert, and Eric M. Gullikson, "Triple-wavelength, narrowband Mg/SiC multilayers with corrosion barriers and high peak reflectance in the 25-80 nm wavelength region", *Opt. Express* **20**, 24018-24029 (2012).
- ⁹² H. K Pew and D. D Allred, "High throughput reflectivity and resolution X-ray dispersive and reflective structures for the 100 eV to 5000 eV energy range and method of making the devices." Patent number US5485499 A.
- ⁹³ Clement Y. J. Hémonnot, and Sarah Köster, "Imaging of Biological Materials and Cells by X-ray Scattering and Diffraction", *ACS Nano* **11**, 8542–8559 (2017).
- ⁹⁴ Peter Fischer, Mi-Young Im, Chloe Baldasseroni, Catherine Bordel, Frances Hellman, Jong-Soo Lee, and Charles S.Fadley, "Magnetic imaging with full-field soft X-ray microscopies", *J. Elec. Spectros. & Rel. Phenom.* **189**, 196-205 (2013).
- ⁹⁵ D. D Bhawalkar, G. Singh and R. V Nandedkar, "Synchrotron radiation sources INDUS-1 and INDUS-2", *Pramana J. Phys.* **50**, 467-484 (1998).
- ⁹⁶ <http://www.rrcat.gov.in/technology/accel/indus/index.html>
- ⁹⁷ S. S.Ramamurthi and G. Singh, "Status of the Indus-I SR source", *Nucl. Instrum. & Meth. Phys. Res. A* **359**, 15-20 (1995).
- ⁹⁸ <http://www.rrcat.gov.in/technology/accel/indus/indus2.html>
- ⁹⁹ S K Deb, Gurnam Singh and P D Gupta, "Indus-2 Synchrotron Radiation Source: current status and utilization", *J. Phys. Conf. Series* **425**, 072009(1-4) (2013).
- ¹⁰⁰ R. V. Nandedkar, K. J. S. Sawhney, G. S. Lodha, A. Verma, V. K. Raghuvanshi, A. K. Sinha, M. H. Modi, and M. Nayak, "First results on the reflectometry beamline on Indus-1", *Curr. Sci.* **82**, 298–304 (2002).
- ¹⁰¹ K J S Sawhney and R V Nandedkar, "Optical design of a toroidal grating monochromator based beam line on Indus-1", *Pramana J. Phys.* **42**, 49-64 (1994).
- ¹⁰² Aby Joseph, Mohammed H Modi, Amol Singh, R.K. Gupta and G.S. Lodha, "Analysis of soft X-ray/VUV transmission characteristics of Si and Al filters", *AIP Conf. Proc.* **1512**, 498-499 (2013).

- ¹⁰³ Mohammed H. Modi, Rajkumar Gupta, Amol Singh, G. S. Lodha, "Quantitative determination of higher harmonic content in the soft X-ray spectra of toroidal grating monochromator using a reflection multilayer", *Appl. Opt.* **51**, 3552 (2012).
- ¹⁰⁴ G. S. Lodha, M. H. Modi, V. K. Raghuvanshi, K. J. S. Sawhney, R. V. Nandedkar, "Soft X-ray reflectometer on Indus-1", *Synchrotron Radiat. News* **17**, 33-35 (2004).
- ¹⁰⁵ E.M. Gullikson, R. Korde, L.R. Canfield, R.E. Vest, "Stable silicon photodiodes for absolute intensity measurements in the VUV and soft X-ray regions", *J. Elect. Spectros.and Rel. Phen.* **80**, 313 (1996).
- ¹⁰⁶ Mohammed H. Modi, R. K. Gupta, S. R. Kane, V. Prasad, C. K. Garg, P. Yadav, V. K. Raghuvanshi, Amol Singh, and Mangalika Sinha, "A soft X-ray reflectivity beamline for 100-1500eV energy range at Indus-2 synchrotron radiation source", *AIP Conf. Proc.* **2054**, 060022 (1-5) (2019).
- ¹⁰⁷ M.C. Hettrick, J.H. Underwood, P.J. Batson and M. J. Eckart, "Resolving power of 35,000 (5 mA) in the extreme ultraviolet employing a grazing incidence spectrometer", *Appl. Optics* **27**, 200–202 (1988).
- ¹⁰⁸ K.Amemiya, H.Kondoh, T.Yokoyama and T.Ohta, "A soft X-ray beamline for surface chemistry at the Photon Factory", *J. Electron Spectros. Rel. Phenomena* **124**, 151–164 (2002).
- ¹⁰⁹ R.Follath and F.Senf, "New plane-grating monochromators for third generation synchrotron radiation light sources", *Nuclear Instruments and Methods in Physics Research A* **390**, 388-394 (1997).
- ¹¹⁰ T. T. Prasad, M. H. Modi, and G. S. Lodha, "Optical Design of VLS-PGM Soft X-ray Beamline on Indus-2", *AIP Conf. Proc.* **1234**, 375-378 (2010).
- ¹¹¹ Paul van der Heide, "X-ray Photoelectron Spectroscopy: An introduction to Principles and Practices" John Wiley and sons Inc. (2012).
- ¹¹² A. Benninghoven, "Chemical Analysis of Inorganic and Organic Surfaces and Thin Films by Static Time-of-Flight Secondary Ion Mass Spectrometry (TOF-SIMS)", *Angewandte Chemie International* **33**, 1023-1043 (1994).
- ¹¹³ M. Veldkamp, H. Zabel and Ch. Morawe, "Thermally induced structural modifications in sputtered C/Al₂O₃ multilayers", *J. Appl. Phys.* **83**, 5233-5238 (1998).
- ¹¹⁴ A. Szeghalmi, S. Senz, M. Bretschneider, U. Gösele, and M. Knez, "All dielectric hard X-ray mirror by atomic layer deposition", *Appl. Phys. Lett.* **94**, 133111 (1-3) (2009).
- ¹¹⁵ J. M. Jensen, A.B. Oelkers, R. Toivola, and D.C. Johnson, "X-ray Reflectivity Characterization of ZnO/Al₂O₃ Multilayers Prepared by Atomic Layer Deposition", *Chem. Mater.* **14**, 2276-2282 (2002).
- ¹¹⁶ A. Das, R. K. Gupta, M. H. Modi, C. Mukherjee, S. K. Rai, A. Bose, T. Ganguli, S. C. Joshi, G. S. Lodha, and S. K. Deb, "Fine structures in refractive index of sapphire at the L_{II,III} absorption edge of aluminum determined by soft X-ray resonant reflectivity", *Appl. Opt.* **51**, 7402-7410 (2012).
- ¹¹⁷ J.Y. Jung, "Optical Modeling Off-Stoichiometric Amorphous Al₂O₃ thin films deposited by reactive sputtering", PhD Thesis, University of Illinois at Urbana-Champaign, (2012).
- ¹¹⁸ R. H. French, H. Müllejan, and D. J. Jones, "Optical Properties of Aluminum Oxide: Determined from Vacuum Ultraviolet and Electron Energy-Loss Spectroscopies", *J. Am. Ceram. Soc.* **81**, 2549-2557 (1998).
- ¹¹⁹ Isao Tanaka and Teruyasu Mizoguchi, "First-principles calculations of X-ray absorption near edge structure and energy loss near edge structure: present and future", *J. Phys. Condens. Matter* **21**, 104201 (1-9) (2009).
- ¹²⁰ Teruyasu Mizoguchi, Atsuto Seko, Masato Yoshiya, Hisao Yoshida, Tomoko Yoshida, W. Y. Ching, and Isao Tanaka, "X-ray absorption near-edge structures of disordered Mg_{1-x}Zn_xO solid solutions", *Phys. Rev. B* **76**, 195125(1-7) (2007).
- ¹²¹ Isao Tanaka, Hiroyuki Araki, Masato Yoshiya, Teruyasu Mizoguchi, Kazuyoshi Ogasawara, and Hirohiko Adachi, "First-principles calculations of electron-energy-loss near-edge structure and near-edge X-ray-absorption fine structure of BN polytypes using model clusters", *Phys. Rev. B* **60**, 4944-4951 (2000).
- ¹²² W. Olovsson, I. Tanaka, T. Mizoguchi, G. Radtke, P. Puschnig, and C. Ambrosch-Draxl, "Al L_{2,3} edge X-ray absorption spectra in III-V semiconductors: Many-body perturbation theory in comparison with experiment", *Phys.Rev. B* **83**, 195206 (1-8) (2011).
- ¹²³ Isao Tanaka and Hirohiko Adachi, "Calculation of core-hole excitonic features on Al L_{2,3}-edge X-ray-absorption spectra of α -Al₂O₃", *Phys. Rev B* **54**, 4604-4608 (1996).
- ¹²⁴ Carmen Sousa, Coen de Graaf, and Francesc Illas, "Core exciton energies of bulk MgO, Al₂O₃, and SiO₂ from explicitly correlated ab initio cluster model calculations", *Phys. Rev B* **62**, 10013-10021 (2000).
- ¹²⁵ Shang-Di Mo and W. Y. Ching, "Ab initio calculation of the core-hole effect in the electron energy-loss near-edge structure", *Phys Rev B* **62**, 7901-7907 (2000).
- ¹²⁶ Kazuyoshi Ogasawara, Isao Tanaka and Hirohiko Adachi, "Analysis of Core-Hole Effect in Cation L_{2,3}-Edge of MgO, α -Al₂O₃ and SiO₂ Based on DV-X α Cluster Calculations", *Advances in Quantum Chemistry* **29**, 441-466 (1997).

- ¹²⁷ E.P. Gusev, M. Copel, E. Cartier, I. J. R. Baumvol, C. Krugs, and M.A. Gribelyuk, “High-resolution depth profiling in ultrathin Al_2O_3 films on Si”, *Appl. Phys. Lett.* **76**, 176-178 (2000).
- ¹²⁸ S.P. Singh, M.H. Modi, and P. Srivastava, “Growth kinetics and compositional analysis of silicon rich a- $\text{SiN}_x\text{:H}$ film: A soft X-ray reflectivity study”, *Appl. Phys. Lett.* **97**, 151906 (1-3) (2010).
- ¹²⁹ M. Zwiebler, J.E. Hamann Borrero, M. Vafaei, P. Komissinskiy, S. Macke, R. Sutarto, F. He, B. Büchner, G.A. Sawatzky, L. Alff, and J. Geck, “Electronic depth profiles with atomic layer resolution from resonant soft X-ray reflectivity”, *New J. Phys.* **17**, 083046 (1-15) (2015).
- ¹³⁰ J. Bai, E.E. Fullerton, and P.A. Montano, “Resonant X-ray reflectivity study of Fe/Cr superlattices”, *Physica B* **221**, 411-415 (1996).
- ¹³¹ Handbook of Optical Constants of Solids, Edited by E. D. Palik, Academic Press, 1991.
- ¹³² F. Gervais, Aluminum oxide (Al_2O_3), in Handbook of Optical Constants of Solids II, E. D. Palik, ed. (Academic, 1991), p 761
- ¹³³ H. J. Hagemann, W. Gudat, and C. Kunz, DESY report SR-74/7, 1974
- ¹³⁴ M Idir, P Mercere, T Moreno, A Delmotte, P Dasilva, and M. H Modi, “Metrology and Tests beamline at SOLEIL Design and first results”, *AIP Conf. Proc.* **1234**, 485-488 (2010).
- ¹³⁵ C Weigel, G Calas, L Cormier, L Galois and G S Henderson, “
Journal of Physics: Condensed Matter
High-resolution Al L_{2,3}-edge X-ray absorption near edge structure spectra of Al-containing crystals and glasses: coordination number and bonding information from edge components”, *J. Phys.: Condens. Matter* **20**, 135219(1-8) (2008).
- ¹³⁶ Elena O. Filatova and Aleksei S. Konashuk, “Interpretation of the Changing the Band Gap of Al_2O_3 Depending on Its Crystalline Form: Connection with Different Local Symmetries”, *J. Phys. Chem. C* **119**, 20755-20761 (2015).
- ¹³⁷ W. L. O' Brien, J. Jia, Q-Y Dong, T. A Callcott, J. -E Rubensson, D. L Mueller, and D. L Ederer, “Intermediate coupling in L₂-L₃ core excitons of MgO, Al_2O_3 , and SiO_2 ”, *Phys. Rev B* **44**, 1013-1018 (1991).
- ¹³⁸ W. L. O' Brien, J. Jia, Q-Y. Dong, T. A. Callcott, D. L. Mueller, D. L. Ederer, N. D Shinn, and S. C Woronick, “Decay channels of Al L_{2,3} excitons and the absence of O K excitons in $\alpha\text{-Al}_2\text{O}_3$ ”, *Phys. Rev. B* **44**, 13277-13282 (1991).
- ¹³⁹ A. Balzarotti, F. Antonangeli, R. Girlanda, and G.Martino, “Core excitons in corundum”, *Solid State Communications* **44**, 275-278 (1982).
- ¹⁴⁰ Arijeet Das, Rajkumar K. Gupta, Mohammed H. Modi, Chandrachur Mukherjee, Sanjay K. Rai, Aniruddha Bose, Tapas Ganguli, Satish C. Joshi, Gyan S. Lodha, and Sudip K. Deb, *Appl. Opt.* **51**, 7402-7410 (2012).
- ¹⁴¹ J.M. Andersson, “Controlling the Formation and Stability of Alumina Phases”, Ph.D. Thesis, Linköping University (2005).
- ¹⁴² <http://srdata.nist.gov/xps/>
- ¹⁴³ Mangalika Sinha and Mohammed H. Modi, “X-ray reflectivity and photoelectron spectroscopy study of aluminum oxide thin film”, *AIP Conf. Proc.* **1832**, 080025(1-3) (2017).
- ¹⁴⁴ G. Faraci, S. La. Rosa and A.R. Pennisi, “Evidence for a new aluminum oxidation state”, *Phys. Rev. B* **47**, 4052-4055 (1993).
- ¹⁴⁵ G. Faraci, S. La. Rosa, A.R. Pennisi, Y. Hwu and G. Margaritondo, “Al intermediate oxidation states observed by core level photoemission spectroscopy”, *J. Appl. Phys.* **78**, 4091-4098 (1995).
- ¹⁴⁶ S. Yuasa, T. Nagahama, A. Fukushima, Y. Suzuki, and K. Ando, “Giant room-temperature magnetoresistance in single-crystal Fe/MgO/Fe magnetic tunnel junctions”, *Nature. Mat.* **4**, 868-871 (2004).
- ¹⁴⁷ S. S. P. Parkin, C. Kaiser, A. Panchula, P. M Rice., B. Hughes, M. Samant, and S. -H Yang, “Giant tunnelling magnetoresistance at room temperature with MgO (100) tunnel barriers”, *Nature Mat.* **3**, 862-867 (2004).
- ¹⁴⁸ T. Awaji, K. Sakuta, Y. Sakaguchi, and T. Kobayashi, “Improved surface crystallinity of MgO crystal substrate through annealing in oxygen atmosphere”, *Jpn. J. Appl. Phys.* **31**, L642-L645 (1992).
- ¹⁴⁹ J. Pascual, J. Camassel, and H. Mathieu, “Fine structure in the intrinsic absorption edge of TiO_2 ”, *Phys. Rev. B* **18**, 5606-5614 (1978).
- ¹⁵⁰ V. V. Pavlov, A. R. Akbashev, A. M. Kalashnikova, V. A. Rusakov, A. R. Kaul, M. Bayer, and R. V. Pisarev, “Optical properties and electronic structure of multiferroic hexagonal orthoferrites RFeO_3 (R = Ho, Er, Lu)”, *J. Appl. Phys.* **111**, 056105 (1-3) (2012).
- ¹⁵¹ D. J. Singh, R. C. Rai, J. L. Musfeldt, S. Auluck, Nirpendra Singh, P. Khalifah, S. McClure, and D. G. Mandrus, “Optical Properties and Electronic Structure of Spinel ZnRh_2O_4 ”, *Chem. Mater.* **18**, 2696-2700 (2006).

- ¹⁵² Yue-Jie Shi, Rong-Jun Zhang, Xin Chen, Lei Wang, Lei Chen, Qing-Hua Huang, Da-Hai Li, Yu-Xiang Zheng, Song-You Wang, Ning Dai and Liang-Yao Chen, “Evolution of optical properties and electronic structures: band gaps and critical points in $\text{Mg}_x\text{Zn}_{1-x}\text{O}$ ($0 \leq x \leq 0.2$) thin films”, *Phys. Chem. Chem. Phys.* **20**, 25467-25475 (2018).
- ¹⁵³ Christian Gähwiller and Frederick C. Brown, “Photoabsorption near the $L_{II,III}$ Edge of Silicon and Aluminum”, *Phys. Rev. B* **2**, 1918-1925 (1970).
- ¹⁵⁴ J. Olivier and R. Poirier, “Electronic structure of Al_2O_3 from electron energy loss spectroscopy”, *Surface Science* **105**, 347-356 (1981).
- ¹⁵⁵ C. Århammar, Annette Pietzsch, Nicolas Bock, Erik Holmström, C. Moyses Araujo, Johan Gråsjög et al., “Unveiling the complex electronic structure of amorphous metal oxides”, *PNAS* **108**, 6355–6360 (2011).
- ¹⁵⁶ A. Ruosi, C. Raisch, A. Verna, R. Werner, B. A. Davidson, J. Fujii, R. Kleiner, and D. Koelle, “Electron sampling depth and saturation effects in perovskite films investigated by soft X-ray absorption spectroscopy”, *Phys. Rev. B* **90**, 125120 (1-8) (2014).
- ¹⁵⁷ Christian Vorwerk, Caterina Cocchi, and Claudia Draxl, “Addressing electron-hole correlation in core excitations of solids: An all-electron many-body approach from first principles”, *Phys. Rev. B* **95**, 155121 (1-10) (2017).
- ¹⁵⁸ Chikashi Suzuki, Tsuyoshi Nishi, Masami Nakada, Mitsuo Akabori, Masaru Hirata, and Yoshiyuki Kaji, “Core-hole effect on XANES and electronic structure of minor actinide dioxides with fluorite structure”, *J. Phys. & Chem. Of Solids* **73**, 209-216 (2012).
- ¹⁵⁹ M. Calandra, J. P. Rueff, C. Gougoussis, D. Ceolin, M. Gorgoi, S. Benedetti, P. Torelli, A. Shukla, D. Chandesris, and Ch. Brouder, “K-edge X-ray absorption spectra in transition-metal oxides beyond the single-particle approximation: Shake-up many-body effects”, *Phys. Rev. B* **86**, 165102 (1-6) (2012).
- ¹⁶⁰ A. Gibaud, J. B Bal, E. M Gullikson, C. Wang, and G. Vignaud, “Resonant soft X-ray reflectivity of ultrathin polymer films at the C-edge: A direct approach”, *AIP Advances* **6**, 095016 (1-8) (2016).
- ¹⁶¹ M. W Williams, and E. T Arakawa, “Optical Properties of Single-Crystal Magnesium Oxide”, *J. Appl. Phys.* **38**, 5272-5276 (1967).
- ¹⁶² J. E Hamann-Borrero, S. Macke, B. Gray, M Kareev, E. Schierle, S. Partzsch, M. Zwiebler, U. Treske, A. Koitzsch, B. Büchner, J. W Freeland, J. Chakhalian, and J. Geck, “Site-selective spectroscopy with depth resolution using resonant X-ray reflectometry”, *Sci. Rep.* **7**, 13792 (1-11) (2017).
- ¹⁶³ E. Filatova, and A. Sokolov, “Effect of reflection and refraction on NEXAFS spectra measured in TEY mode”, *J Synchrotron Rad.* **25**, 232-240 (2018).
- ¹⁶⁴ D. Alders, T. Hibma, G. A. Sawatzky, K. C. Cheung, G. E. van Dorssen, M. D. Roper, H. A. Padmore, G. van der Laan, J. Vogel, and M. Sacchi, “Grazing incidence reflectivity and total electron yield effects in soft X-ray absorption spectroscopy”, *J. Appl. Phys.* **82**, 3120-3124 (1997).
- ¹⁶⁵ W. Olovsson, I. Tanaka, T. Mizoguchi, P. Puschnig, and C. Ambrosch-Draxl, “All-electron Bethe-Salpeter calculations for shallow-core X-ray absorption near-edge structures”, *Phys. Rev B* **79**, 041102(R) (2009).
- ¹⁶⁶ J. Vinson, J. J Rehr, J. J Kas, and E. L Shirley, “Bethe-Salpeter equation calculations of core excitation spectra”, *Phys. Rev. B* **83**, 115106 (1-7) (2011).
- ¹⁶⁷ http://www.csr.res.in/ion_beam_sputter_deposition_system.html
- ¹⁶⁸ J. P Singh, S. Gautam, B. B Singh, S. Chaudhary, D. Kabiraj, D. Kanjilal, K. H. Chae, R. Kotnala, Jenn-Min Lee, Jin-Ming Chen, and K. Asokan, “Magnetic, Electronic Structure And Interface Study Of Fe/MgO/Fe Multilayer”, *Adv. Mat. Lett.* **5**, 372-377 (2014).
- ¹⁶⁹ C. Elsässer, and S. Köstlmeier, “Density-functional modelling of core-hole effects in electron energy-loss near-edge spectra”, *Ultramicroscopy* **86**, 325–337 (2001).
- ¹⁷⁰ C. Hébert, J. Luitz, and P. Schattschneider, “Improvement of energy loss near edge structure calculation using Wien2k”, *Micron* **34**, 219–225 (2003).
- ¹⁷¹ S. Gao, C. J Pickard, A. Perlov, and V. Milman, “Core-level spectroscopy calculation and the plane wave pseudopotential method”, *J. Phys. Condens. Matter* **21**, 104203 (1-12) (2009).
- ¹⁷² P. Luches, S. D’Addato, S. Valeri, E. Groppo, C. Prestipino, C. Lamberti and F. Boscherini, “X-ray absorption study at the Mg and O K edges of ultrathin MgO epilayers on Ag(001)”, *Phys. Rev. B* **69**, 045412(1-9) (2004).
- ¹⁷³ S. M. Edlou, A. Smajkiewicz, and G. A. Al-Jumaily, “Optical properties and environmental stability of oxide coatings deposited by reactive sputtering”, *Appl. Optics* **32**, 5601-5605 (1993).
- ¹⁷⁴ N.L. Zhang, Z.T. Song, Q. Wan, Q.W. Shen, and C.L. Lin, “Interfacial and microstructural properties of zirconium oxide thin films prepared directly on silicon”, *Appl. Surf. Sci.* **202** 126–130 (2002).
- ¹⁷⁵ S. Harasek, H. D. Wanzenboeck, and E. Bertagnolli, “Compositional and electrical properties of zirconium dioxide thin films chemically deposited on silicon”, *J. Vac. Sci. & Technol A* **21**, 653-659 (2003).

- ¹⁷⁶ V. K. Dixit, A. Marathe, G. Bhatt, S. K. Khamari, K. Rajiv, R. Kumar, C. Mukherjee, C. J. Panchal, T. K. Sharma, and S. M. Oak, "Evaluation of structural and microscopic properties of tetragonal ZrO₂ for the facet coating of 980 nm semiconductor laser diodes", *J. Phys. D* **48**, 105102 (1-10) (2015).
- ¹⁷⁷ A. Kikas, J. Aarik, V. Kisand, K. Kooser, T. Kämre, H. Mändar, T. Uustare, R. Rammula, V. Sammelselg and I. Martinson, "Effect of Phase Composition on X-ray Absorption Spectra of ZrO₂ Thin Films", *J. Elec. Spectro. Rel. Phenomena* **156-158**, 303-306 (2007).
- ¹⁷⁸ D. W McComb, "Bonding and electronic structure in zirconia pseudopolymorphs investigated by electron energy-loss spectroscopy", *Phys. Rev. B* **54**, 7094–7102 (1996).
- ¹⁷⁹ B. Ravel and M. Newville, "ATHENA, ARTEMIS, HEPHAESTUS: data analysis for X-ray absorption spectroscopy using IFEFFIT" *J. Synch. Rad.* **12**, 537 (2005).
- ¹⁸⁰ M. A. Andreeva, E. P. Domashevskaya, E. E. Odintsova, V. A. Terekhov and S. Yu. Turishchev, "Interference phenomena of synchrotron radiation in TEY spectra for silicon-on-insulator structure", *J. Synchrotron Rad.* **19**, 609-618 (2012).
- ¹⁸¹ M. A. Andreeva, Yu. L. Repchenko, E. P. Domashevskay, V. A. Terekhov, P. V. Seredin, and V. M. Kashkarov, "The problem of XANES spectrum interpretation measured by TEY technique at different photon glancing angles", *J. Elec. Spectros. Rel. Phenomena* **191**, 35-40 (2013).
- ¹⁸² Wen Ma, F. William Herbert, Sanjaya D. Senanayake, Bilge Yildiz, "Non-equilibrium oxidation states of zirconium during early stages of metal oxidation", *Appl. Phys. Lett.* **106**, 101603(1-5) (2015).
- ¹⁸³ Saurabh Sharma, M.Tech Thesis, "Kramers-Kronig Analysis of Soft X-ray Reflectivity Data", GSITS, Indore.